μ^+SR MEASUREMENT OF THE TEMPERATURE DEPENDENCE OF THE MAGNETIC PENETRATION DEPTH IN $YBa_2Cu_3O_{6.95}$ SINGLE CRYSTALS

By

Jeffrey E. Sonier

Hon. B.Sc. Univ. of Western Ont., 1991

A THESIS SUBMITTED IN PARTIAL FULFILLMENT OF

THE REQUIREMENTS FOR THE DEGREE OF

MASTER OF SCIENCE

in

THE FACULTY OF GRADUATE STUDIES

DEPARTMENT OF PHYSICS

We accept this thesis as conforming

to the required standard

THE UNIVERSITY OF BRITISH COLUMBIA

In presenting this thesis in partial fulfilment of the requirements for an advanced degree at the University of British Columbia, I agree that the Library shall make it freely available for reference and study. I further agree that permission for extensive copying of this thesis for scholarly purposes may be granted by the head of my department or by his or her representatives. It is understood that copying or publication of this thesis for financial gain shall not be allowed without my written permission.

Department of Physics
The University of British Columbia
6224 Agricultural Road
Vancouver, Canada
V6T 1W5

Date: April 29, 1994

Abstract

This thesis presents the results of transverse-field muon spin rotation (TF-μ^+SR) measurements of the magnetic penetration depth in the ab-plane (*i.e.* λ_{ab}), for the vortex state of high quality single crystals of $YBa_2Cu_3O_{6.95}$. In particular, the low-temperature dependence of λ_{ab} was determined in an effort to clarify the nature of the pairing mechanism in the $YBa_2Cu_3O_{6.95}$ compound. These results should be more reliable than previous μ^+SR studies on powders and crystal mosaics, due to the employment of a novel low-background apparatus, as well as to improvements in sample quality and in the fitting procedure.

A strong linear temperature dependence for $1/\lambda_{ab}^2$ was found to exist below 50K for applied magnetic fields of 0.5T and 1.5T. This linear temperature dependence contradicts the consensus of previous μ^+SR studies which suggested a behaviour consistent with conventional s-wave pairing of carriers in the superconducting state. The presence of a linear term in the data reported here, supports recent microwave cavity measurements in zero field and indicates the existence of a more unconventional pairing state. In addition, a possible field dependence for λ_{ab} at low temperatures was indicated by the data, with $\lambda_{ab}(T=0)$ having a range of $1347-1451$Å and $1437-1496$Å for the 0.5T and 1.5T data, respectively. The range of these values was determined by fitting the data several different ways. For each type of analysis, $\lambda_{ab}(0)$ was found to be greater and the linear term was stronger in the 0.5T data. Furthermore, the 1.5T data appear to agree better with the microwave cavity measurements.

Included in this thesis is a qualitative description of the conventional s-wave pairing state and a proposed d-wave pairing state, called $d_{x^2-y^2}$. The findings in this μ^+SR

study support the latter, but does not rule out the possibility of other anisotropic pairing states or isotropic pairing theories in which critical fluctuations persist down to very low temperatures.

Table of Contents

List of Tables

List of Figures

Acknowledgements

I would like to thank my thesis advisor Rob Kiefl for many patient and informative discussions over the past two years, all of which have accelerated my research and heightened my interest in the field of high-T_c superconductors. Equal thanks to Jess Brewer, the TRIUMF spokesperson for this experiment and the author of many of the valuable computer programs used in the analysis process.

Additional thanks to my predecessor in this work, Tanya Riseman, who provided me with the algorithm which forms the basis for the computer program I used to fit the data. I am also appreciative of the early help from Juerg Schneider, who helped design the low-background apparatus used in this experiment. For making the wonderful $YBa_2Cu_3O_{6.95}$ crystals, I thank Ruixing Liang. For running shifts in this experiment and/or participating in inspirational discussions, I would like to thank Walter Hardy, Doug Bonn, Andrew MacFarlane, Gerald Morris, Kim Chow, Tim Duty, Phillipe Mendels, Jim Carolan and Arnold Sikkema. Also, thanks to Curtis Ballard and Keith Hoyle for their technical assistance.

Chapter 1

Introduction

In recent years, "high-T_c" superconductors have generated a frenzy of experimental and theoretical endeavours, motivated by the likelihood of spawning revolutionary technologies. Their mere existence challenges our present-day understanding of many facets of condensed matter physics. The particular features which distinguish this class of materials from conventional BCS superconductors have been well documented. Besides the extraordinarily high transition temperatures in excess of 120K, some of the more noteable differences include: anomalous normal-state properties, strong anisotropy, a very small coherence length and unconventional behaviour in the superconducting state.

Early experiments intended to answer some of the broader questions concerning the nature of the mechanism forming the basis for superconductivity in the high-T_c materials, yielded conflicting and questionable results. More recently, the experiments have become more reliable, mainly because of vast improvements in sample quality. Researchers now recognize that the inherent differences between high-T_c powders, thin films and single crystals, are significant enough that they must be accounted for when interpreting and comparing results. Furthermore, it is now understood that impurities play a major role in the outcome of many of these experiments, so that often only experiments done with the same sample are comparable.

Theories regarding the high-T_c compounds are divided into two major categories: "Fermi liquid" and "non-Fermi liquid" theories. The normal state of a conventional

BCS superconductor is well described by a Fermi liquid. However, the anomalous normal-state properties of the high-T_c compounds hint at the possible absence of a Fermi surface in this class of materials. The interpretation of experimental measurements is dependent upon which class of theories one assumes. For now at least, there is an unwillingness to stray too far from conventional thinking and the successes of BCS theory, so that experimental results are usually interpreted in the context of Fermi liquid theories.

With the general assumption that the electronic ground state of the high-T_c superconductors is composed of paired charge carriers, determining the symmetry of the paring state has been the subject of much controversy. Despite many of the earlier reports, it is now generally agreed that conventional s-wave pairing of carriers is unlikely. The pairing state is almost certainly anisotropic, but beyond this, little is known for certain. A leading candidate in the high-T_c materials is the d-wave form of pairing called $d_{x^2-y^2}$ [1,2]. For $d_{x^2-y^2}$ symmetry, the wave-vector dependence of the energy gap which develops at the Fermi surface in the superconducting state is such that line nodes appear in the gap.

Measurements of the temperature dependence of the magnetic penetration depth λ are one way to probe the nature of the low-energy excitations and the symmetry of the pairing state. For an isotropic s-wave superconductor, the magnetic penetration depth $\lambda(T)$ varies exponentially at low temperatures. Even if the superconducting gap is anisotropic, as long as it does not vanish anywhere on the Fermi surface, the penetration depth $\lambda(T)$ will still exhibit exponential behaviour at temperatures such that k_BT is less than the minimum value of the energy gap for excitations [3].

However, if the symmetry of the superconducting state is $d_{x^2-y^2}$, with the associated line nodes running along the cylindrical Fermi surface, Cooper pairs can be broken more easily and $\lambda(T)$ is expected to change linearly with temperature at low

temperatures [4,5]. Recent microwave cavity perturbation measurements of $\Delta\lambda$ (*i.e.* $\lambda(T) - \lambda(0)$) on high quality $YBa_2Cu_3O_{6.95}$ single crystals show a strong linear term below $30K$ [6]. Studies of $Tl_2CaBa_2Cu_2O_{8-\delta}$ single crystals also show a linear dependence on T for $\lambda(T)$ at low temperatures [7]. However, previous experiments in $Bi_2Sr_2CaCu_2O_8$ and $YBa_2Cu_3O_{7-\delta}$ thin films showed a T^2 dependence on $\lambda(T)$ [8]. It has been pointed out that impurity scattering in a $d_{x^2-y^2}$-wave superconductor can change the low-temperature behaviour from $\lambda(T) \sim T$ to $\lambda(T) \sim T^2$ [5,6,7].

Muon spin rotation is the most direct way to measure λ_{ab} (the penetration depth in the ab-plane) in the bulk of the sample. Unlike other techniques, which are performed in zero-static magnetic field, μ^+SR directly measures the magnetic field distribution associated with the vortex lattice of a type II superconductor. The penetration depth λ_{ab} is the length scale over which magnetic flux leaks into the superconducting regions around the vortex cores. The μ^+SR technique provides a means by which one can investigate not only the temperature dependence of λ_{ab}, but also its field dependence. The difficulty in the μ^+SR technique lies in the extraction of λ_{ab} from the measured data. Here, one relies heavily on a phenomenological model of the magnetic field distribution and the ability of the fitting program to extract the relevant parameters.

Previous μ^+SR studies on sintered powders and crystals of $YBa_2Cu_3O_{7-\delta}$, which were of lower quality than the ones used in this study, provide evidence in support of an isotropic s-wave pairing state [9]. However, impurities or other crystalline imperfections could lead to a T^2 dependence. Furthermore, conclusions regarding the pairing mechanism were based on the overall behaviour of $\lambda(T)$ rather than that in the low-temperature regime. It has been argued that the temperature dependence of $\lambda(T)$ at higher temperatures can be drastically altered by strong-coupling corrections, impurity scattering, the precise shape of the Fermi surface and gap anisotropy [4].

A universal equation for $\lambda(T)$ at all $T < T_c$, based on the d-wave formalism, has yet

to be determined. One must rely solely on the low-temperature deviations from s-wave theory, anticipated from purely qualitative arguments. Consequently, conclusions with regard to the pairing mechanism in $YBa_2Cu_3O_{7-\delta}$ requires precise low temperature data. Previous μ^+SR measurements of $\lambda(T)$ either lacked good low-temperature data or were done on sintered powders. Low-temperature measurements of $\lambda(T)$ should also be able to reconcile the nature of the nodes in the gap, if they do indeed exist. That is to say, point nodes on the Fermi surface should be distinguishable from the line nodes associated with $d_{x^2-y^2}$ pairing [4].

This present study is concerned with recent μ^+SR measurements of λ_{ab} in single crystals of $YBa_2Cu_3O_{6.95}$. Some words of caution must be provided to the reader. Recent discovery of a significant $\vec{a}$-$\vec{b}$ anisotropy in the magnetic penetration depth [10] may have a dramatic influence on the interpretation of measurements of $\lambda_{ab}(T)$. Although the existence of $\vec{a}$-$\vec{b}$ anisotropy is acknowledged in this study, it is not included in the final analysis, as the matter is presently under investigation. Also, during the final stages of this thesis there have been recent suggestions that $\lambda(T)$ is controlled by critical fluctuations down to very low temperatures [11]. In this case, the measured $\lambda(T)$ has little to do with the pairing mechanism, but is determined by the $3D$ XY and $2D$ XY universality classes. This possibility is not discussed any further in this thesis.

Chapter 2

Theory

2.1 Magnetic Properties of Conventional Superconductors

2.1.1 Type-I Superconductors

The Meissner effect, which has long been used to characterize conventional superconductors, is also readily observed in high temperature superconductors. When these compounds are cooled below a critical temperature T_c in the presence of an externally applied magnetic field, all of the magnetic flux is expelled from their interior in the absence of flux pinning. When the external field exceeds a critical value (H_c), the superconductor returns to its normal state. Superconductors which obey the magnetization curve depicted in Fig. 2.1 are called type-I superconductors. The critical field $H_c(T)$ which separates the *superconducting* and *normal* phases is a temperature dependent quantity.

2.1.2 The London Penetration Depth

In 1935, F. and H. London modified an essential equation of electrodynamics (i.e. Ohm's Law) in such a way as to obtain the Meissner effect, without altering Maxwell's equations themselves. In doing so, they incorporated the two-fluid model of Gorter and Casimir [12]. The two-fluid model separates the electron system into a *superconducting* component with an electron density n_s, and a *normal* component with an electron density n_n. They assumed the total electron density $n_o = n_s + n_n$ behaved such that

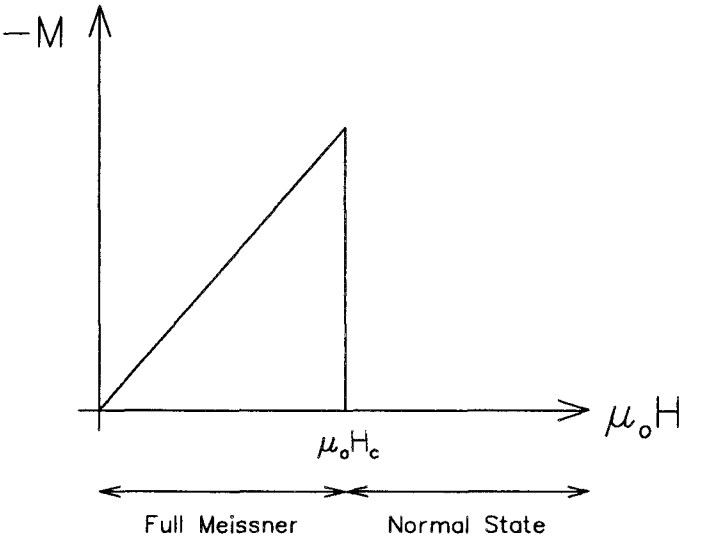

Figure 2.1: Magnetization curve for a type-I superconductor. M is the average magnetization defined by $\overline{B} = \mu_o H + M$, where $\overline{B}$ is the spatial average of the field in the superconductor.

$n_s \rightarrow n_o$ as $T \rightarrow 0$, and $n_n = n_o$ when $T > T_c$. Emerging from their phenomenological model is the so-called *London penetration depth* λ_L [13]:

$$\frac{1}{\lambda_L^2} = \frac{4\pi e^2 n_s}{m^* c^2} \tag{2.1}$$

where m^* is the effective mass of the superconducting carriers, and n_s is the superconductor carrier density. Pure-elemental metals and low concentration alloys (*eg.* dilute SnIn alloy system [14]), where $m^* \approx m_e$ (free electron mass), tend to be type-I. Generally speaking, λ_L is short and the Fermi velocity of the superconducting carriers v_F is high in these materials [15].

The physical significance of λ_L pertains to the failure of the Meissner effect to occur abruptly at the surface of a superconductor; rather the magnetic field penetrates slightly into the bulk of the superconducting material on a length scale given by λ_L. Consider a semi-infinite superconductor with the boundary between normal and superconducting

regions at $x = 0$. In the presence of an external magnetic field applied perpendicular to the surface, London theory predicts that the magnetic flux decays exponentially into the bulk of the superconductor according to [13,16]:

$$\vec{B}(x) = \vec{B}(0)e^{-x/\lambda_L} \tag{2.2}$$

where $\vec{B}(0)$ is the magnetic field at the surface of the superconductor, and x is the distance into the superconductor from the surface (see Fig. 2.2). The expulsion of the magnetic field is accomplished by shielding currents (or *supercurrents*) which flow at the surface of the superconductor without any Ohmic losses. These supercurrents form a finite sheath which is spread out to a thickness λ_L into the sample. Such a distribution of current is much more energetically favourable than an infinitely thin sheath of current [13]. The supercurrent density $\vec{J}_s$ is related to the local magnetic flux density $\vec{B}$ by Ampére's Law:

$$\vec{\nabla} \times \vec{B} = \mu_o \vec{J}_s \tag{2.3}$$

2.1.3 The Coherence Length (Pippard's Equation)

The London equations whose derivation appears elsewhere (see [13] for instance), are local equations (i.e. they relate the current density at a point $\vec{r}$ to the vector potential $\vec{A}$ at the same point), and hence define the superconducting properties as such. However, early discrepancies between experimental estimations of $\lambda_L(0)$ (the penetration depth at zero temperature) for certain conventional superconductors, and those predicted by Eq. (2.1) led Pippard [13,15] in 1950 to introduce non-local effects into the London equations. Spatial changes of quantities such as n_s in a superconductor may only occur on a finite length scale, the *coherence length* ξ_o, and not over arbitrarily small distances. That is to say, whenever n_s is varying in space its value may change significantly over

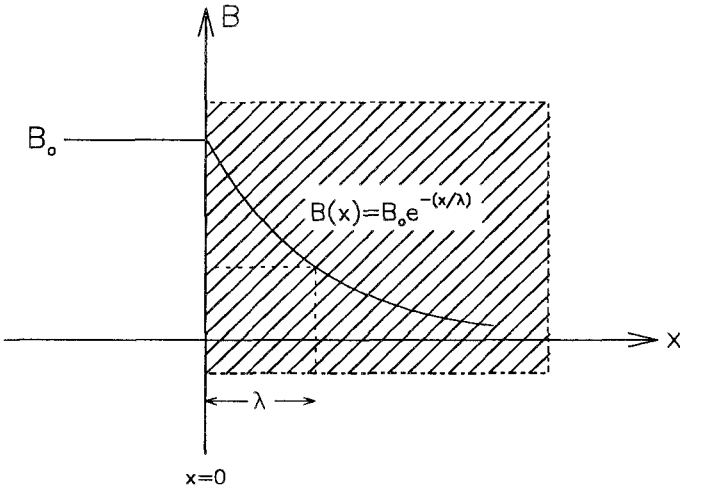

Figure 2.2: The magnetic field B_o at the surface of the superconductor decays to B_o/e at a distance $x = \lambda$ in the interior of the superconductor (shaded region).

distances of order ξ_o. Thus the coherence length defines the intrinsic nonlocality of the superconducting state. Using the uncertainty principle, Pippard estimated the coherence length for a pure metal to be [17,18]:

$$\xi_o \approx \frac{\hbar v_F}{\pi \Delta(0)} \approx 0.18 \frac{\hbar v_F}{k_B T_c} \tag{2.4}$$

where k_B is Boltzmann's constant, and $\Delta(0)$ is the energy gap that forms at the Fermi surface in the superconducting state at absolute zero. This will be discussed in more detail later.

In the London model, the local value of the magnetic flux density $B(\vec{r})$ and the supercurrent density $J(\vec{r})$ are assumed to vary slowly in space on a length scale λ_L, and have negligible variation over distances $\sim \xi_o$. In Fig. 2.2, the superconducting carrier density n_s jumps discontinuously from zero to a maximum value at the sample surface. As already mentioned, n_s is expected to make a significant change like this only over a distance on the order of ξ_o. Thus in Fig. 2.2, $\xi_o = 0$, so that one would

anticipate an exponential screening of the magnetic field in a real superconductor only when $\lambda_L \gg \xi_o$. Indeed, the London model is valid only for $\lambda_L \gg \xi_o$.

In a type-I superconductor, the magnetic penetration depth λ_L is much less than the coherence length ξ_o, so that n_s does not reach its maximum value near the surface. That is to say, not all of the electrons within a thickness ξ_o from the surface of the superconductor contribute to the screening currents. Consequently, the penetration of the magnetic field does not follow the exponential form of Eq. (2.2) until one ventures an appreciable distance $x \sim \xi_o$ into the superconductor. Thus the usual London model is inadequate in describing type-I superconductors where, $\xi_o \gg \lambda_L$. A modification of the London equations which gives the magnetic flux and supercurrent densities a more rapid variation in space, predicts the actual penetration depth λ in a type-I superconductor to be [14]:

$$\lambda = (0.62\lambda_L^2 \xi_o)^{1/3}, \quad (\xi_o \gg \lambda_L) \tag{2.5}$$

where λ is larger than λ_L, but much smaller than ξ_o.

2.1.4 Ginzburg-Landau Theory

In 1950, Ginzburg and Landau introduced the so-called *superconducting order parameter* $\Psi(\vec{r})$ to describe the nonlocality of the superconducting properties. $\Psi(\vec{r})$ can be thought of as a measure of the order in the superconducting state at position $\vec{r}$ below T_c. It has the properties that $\Psi(\vec{r}) \to 0$ as $T \to T_c$, and $|\Psi(\vec{r})|^2 = n_s(\vec{r})$ (i.e. the local density of superconducting electrons). At the time Ginzburg-Landau (GL) theory was developed, the nature of the superconducting carriers was yet to be determined. Interpreting m^* as the effective mass and q as the charge of the fundamental superconducting

particles (whatever they may be), they derived the penetration depth as:

$$\lambda(T) = \sqrt{\frac{m^* c^2}{4\pi q^2 |\Psi_o|^2}} \tag{2.6}$$

where $|\Psi_o|^2$ is the value of $|\Psi|^2$ deep inside the superconductor (i.e. its equilibrium value). The coherence length defined in the GL-formalism is:

$$\xi(T) = \sqrt{\frac{\hbar^2}{2m^* |\alpha(T)|}} \tag{2.7}$$

where $\alpha(T)$ is a temperature-dependent coefficient in the series expansion of the free energy (see [19]). As written, (2.6) and (2.7) suggest that the penetration depth $\lambda(T)$ and the coherence length $\xi(T)$ are temperature dependent quantities. Eq. (2.7) is closely related to the Pippard coherence length ξ_o defined in Eq. (2.4). In GL-theory, the coherence length $\xi(T)$ is the characteristic length for variations in $|\Psi(\vec{r})|^2 = n_s(\vec{r})$. One noteable difference is that Pippard's coherence length ξ_o is independent of temperature. In fact in the dirty limit $\xi(T = 0)$ reduces to Eq. (2.4). Near the transition temperature T_c both $\lambda(T)$ and $\xi(T)$ vary as $(1 - T/T_c)^{-1/2}$, prompting the introduction of the Ginzburg-Landau parameter κ, where:

$$\kappa = \frac{\lambda(T)}{\xi(T)} \tag{2.8}$$

The variation of $\lambda(T)$ and $\xi(T)$ with temperture near T_c comes from an expansion of the free energy density to first-order in the field $\vec{H}$. It follows that κ in (2.8) is temperature independent to this order. An exact calculation from microscopic theory gives a weak temperature dependence for κ, with κ increasing for decreasing temperature T. Through energy considerations, Ginzburg and Landau characterized a type-I superconductor as one in which $\kappa < 1/\sqrt{2}$. For $\kappa \gg 1$, GL theory reduces to the London model.

2.1.5 The Clean and Dirty Limits

The purity of a superconductor is characterized by the ratio l/ξ_o. ξ_o is the coherence length of the pure material, and is given by Eq. (2.4). l is the *electron mean free path*, defined as:

$$l = \tau v_F \tag{2.9}$$

where τ is the time interval between collisions of conduction electrons with impurities in the sample. The magnitude of τ is determined in the normal state. A sample is *clean* if $l/\xi_o \gg 1$, and *dirty* if $l/\xi_o \ll 1$ [20]. The *actual* coherence length when impurities are considered, is dependent upon the mean free path l. Intuitively, one can define an *effective coherence length* $\xi(l)$ such that [13,17]:

$$\frac{1}{\xi(l)} = \frac{1}{\xi_o} + \frac{1}{l} \tag{2.10}$$

According to Eq. (2.10), the coherence length $\xi(l)$ becomes shorter with decreasing l, so that in the *dirty limit*:

$$\xi(l) = l, \quad (l \ll \xi_o) \tag{2.11}$$

and in the *clean limit*:

$$\xi(l) = \xi_o, \quad (l \gg \xi_o) \tag{2.12}$$

Eq. (2.11) and Eq. (2.12) are valid only for $T = 0$K. In the clean limit ($l \gg \xi_o$) at $T = 0$K, the magnetic penetration depth is the London penetration depth given in Eq. (2.1). The actual coherence length $\xi(T)$ and the observed penetration depth $\lambda(T)$ as determined by microscopic theory are given in the *clean limit* ($l \gg \xi_o$) as [21]:

$$\xi(T) = 0.74\xi_o \left(\frac{T_c}{T_c - T}\right)^{\frac{1}{2}} \tag{2.13}$$

$$\lambda(T) = 0.71\lambda_L \left(\frac{T_c}{T_c - T}\right)^{\frac{1}{2}} \tag{2.14}$$

and in the *dirty limit* ($l \ll \xi_o$):

$$\xi(T) = 0.85(\xi_o l)^{\frac{1}{2}} \left(\frac{T_c}{T_c - T}\right)^{\frac{1}{2}} \tag{2.15}$$

$$\lambda(T) = 0.62\lambda_L \left(\frac{\xi_o}{l}\right)^{\frac{1}{2}} \left(\frac{T_c}{T_c - T}\right)^{\frac{1}{2}} \tag{2.16}$$

where Equations (2.13) through (2.16) are valid only in the neighborhood of T_c, such that $(T_c - T)/T_c \ll 1$ [22]. The important result is that according to Eqs.(2.15) and (2.16), as l decreases (*i.e.* the superconductor becomes more impure), $\lambda(T)$ increases, while $\xi(T)$ decreases. Thus $\lambda(T) \gg \xi(T)$ at all temperatures in an impure material. The high-temperature superconductors have short coherence lengths on the order of $\xi \sim 12$ to 15Å. Since the electron mean free path l is typically ~ 150Å in these materials, then they are well within the clean limit [23].

2.1.6 BCS Theory for Conventional Superconductors

In 1957 the underlying microscopic theory of superconductivity in metals was unveiled by J. Bardeen, L.N. Cooper and J.R. Schrieffer [24], in the now famous *BCS theory.* In normal metals, the situation is well described by *free electron theory*, where the electrons behave as free particles and the metallic ions play a limited role in conductivity. BCS theory outlines how in the presence of an attractive interaction between electrons (*Cooper pairs*), the normal state of an otherwise free electron gas becomes unstable to the formation of a coherent many-body ground state. The mechanism behind the weak attractive force binding the Cooper pairs was actually first suggested by Herbert Frölich [25]. He proposed that the same mechanism responsible for much of the electrical resistivity in metals (*i.e.* the interaction of conduction electrons with lattice vibrations) leads to a state of superconductivity. This hypothesis of an electron-phonon interaction was born out of experiments which found that the critical temperature T_c varied with

isotopic mass. In simple terms, an electron interacts with the lattice by virtue of the Coulomb attraction it feels for the metallic ions. The result is a deformation of the lattice (*i.e.* a phonon). A second electron in the vicinity of the deformed lattice correspondingly lowers its energy, resulting in an electron-electron attraction via a phonon. Viewed in this context, the superconducting order parameter $\Psi(\vec{r})$ from GL-theory can be interpreted as a one-particle wave function describing the position of the center of mass of a Cooper pair [26].

Despite being an extremely weak attraction, bound pairs form in part because of the presence of a Fermi *sea* of additional electrons. As a result of the Pauli exclusion principle, electrons that would prefer to be in a state of lower kinetic energy cannot populate these states because they are already occupied by other electrons. Thus a Fermi sea is required to ensure the formation of bound pairs of electrons; otherwise an isolated pair of electrons would just repel one another as a result of the Coulomb force between them. The Fermi sea itself is comprised of other distinct bound pairs of electrons. It follows that each electron is a member of both a Cooper pair and of the Fermi sea which is necessary for the formation of all Cooper pairs. The force of attraction between the electrons which comprise a Cooper pair has a range equivalent to the coherence length. It should be noted that the separation between electrons in a Cooper pair (and thus the correlation length ξ), for a type-I superconductor, is large enough that millions of other pairs have their centers of mass positioned between them. It is then assumed that the occupancy of a bound pair is instantaneous and uncorrelated with the occupancy of other bound pairs at an instant in time [27]. Armed with knowledge of the fundamental particles responsible for superconductivity (*i.e.* Cooper pairs), the substitutions $q = 2e$ and $|\Psi_\circ|^2 = n_s/2$ immediately transform the Ginzburg-Landau result for the penetration depth $\lambda(T)$ [*i.e.* Eq. (2.6)] into the result predicted by London theory [*i.e.* Eq. (2.1)].

One of the most remarkable features emerging from BCS theory, is the existence of an *energy gap* $\Delta(T)$ between the BCS ground state and the first excited state. It is the minimum energy required to create a single-electron (hole) excitation from the superconducting ground state. Thus the binding energy of a Cooper pair is two times the energy gap $\Delta(T)$. BCS theory estimates the zero-temperature energy gap $\Delta(0)$ as [26]:

$$\Delta(0) = 1.76 k_B T_c \tag{2.17}$$

and near the critical temperature T_c,

$$\frac{\Delta(T)}{\Delta(0)} = 1.74 \left(1 - \frac{T}{T_c}\right)^{1/2}, \quad T \approx T_c \tag{2.18}$$

so that the energy gap approaches zero continuously as $T \to T_c$. Superconductors which obey Eq. (2.17) are considered to be weakly-coupled, in reference to the weak interaction energy between electrons in a Cooper pair. Furthermore, the wave functions corresponding to electron pairs (Cooper pairs), are spatially symmetric like an atomic s-orbital with angular momentum $L = 0$. That is to say, the wave function of a pair is unchanged if the positions of the electrons are exchanged. This immediately implies that the spin part of the wave function is antisymmetric in accordance with the Pauli exclusion principle. In particular, the electron pairs are in a spin-singlet state $S = 0$ with antiparallel spins. The pairing mechanism in a conventional superconductor is thus appropriately called, *s-wave spin-singlet.* The energy gap of an s-wave superconductor is finite over the entire Fermi surface. Under ideal circumstances, the magnitude of the gap is the same at all points on the Fermi surface. BCS theory assumes the Fermi surface is spherical (see Fig. 2.3). More realistically however, the energy gap reflects the symmetry of the crystal under consideration [28]. For a conventional s-wave

superconductor with a weak-coupling ratio $\Delta(0)/k_BT_c = 1.76$, BCS theory predicts:

$$\frac{\lambda(T)}{\lambda(0)} - 1 \approx 3.33 \left(\frac{T}{T_c}\right)^{1/2} e^{-1.76T_c/T} \tag{2.19}$$

for small T (*i.e.* $T < 0.5T_c$) [17,29]. At low temperatures, the energy gap is virtually independent of temperature and much larger than the thermal energy k_BT. The probability of exciting a single electron with energy E_k is then proportional to the Boltzmann factor e^{-E_k/k_BT}. The maximum value of this probability is proportional to $e^{-\Delta(0)/k_BT} = e^{-1.76T_c/T}$, which is the exponential factor appearing in Eq. (2.19). Therefore in conventional superconductors, $\lambda(T)$ shows an exponential decrease at low temperatures.

If the value of the energy gap is not constant over the entire Fermi surface, then the minimum value of the gap determines the density of quasiparticle excitations at these low temperatures. Hence the topology of the energy gap is crucial in deciding the low-temperature behaviour of $\lambda(T)$. If the sample under investigation is riddled with impurities, then there will exist a broad range of transition temperatures ΔT_c [30]. Equations (2.17) and (2.18) suggest that one should anticipate a corresponding distribution of gap energies in such materials.

Some systems (e.g. lead, mercury) produce experimental results which deviate substantially from the BCS results [26]. These materials are more appropriately described by strong-coupling theory where the coupling ratio $\Delta(0)/k_BT_c$ is greater than the BCS prediction of 1.76. Under certain conditions superconductivity can occur without an energy gap in some materials. Tunneling experiments on superconductors with specific concentrations of paramagnetic impurities show this to be possible [31]. Theories exist which explain such anomalies, and the nature of the gap as we will soon see is a vital property to be considered in any theory describing superconductivity in the high-T_c compounds.

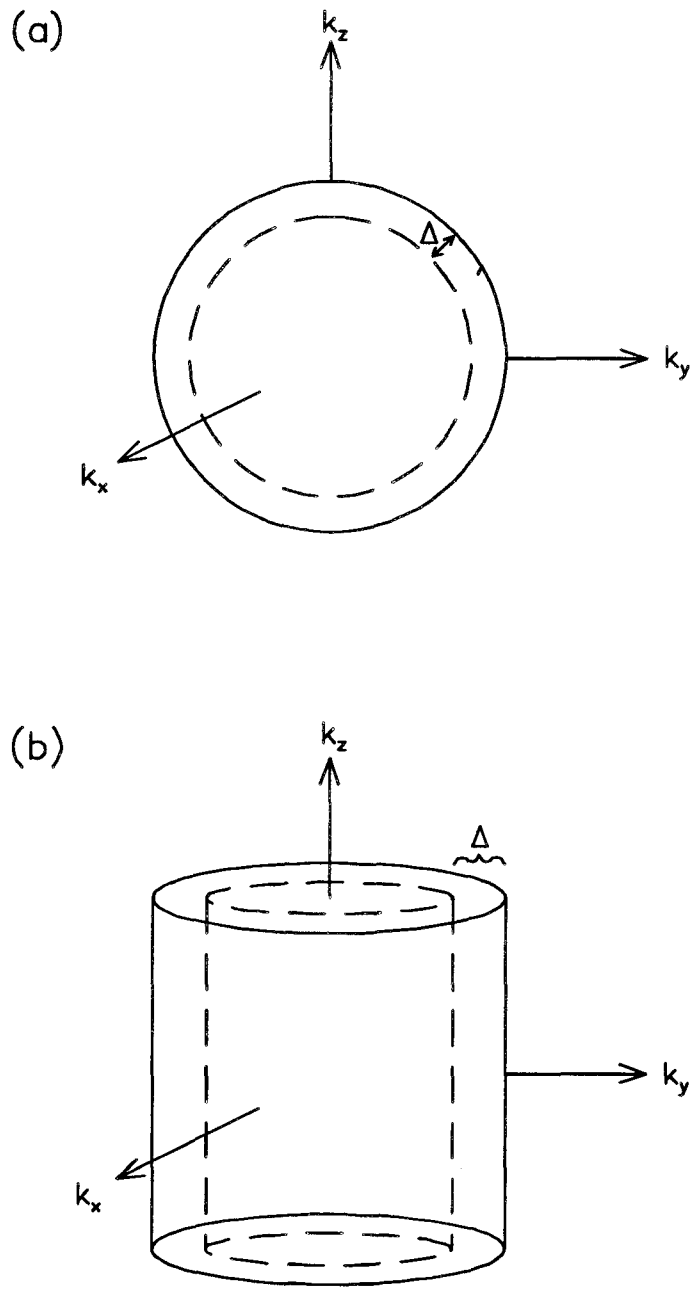

Figure 2.3: Isotropic *s*-wave energy gap for a (a) spherical Fermi surface and, (b) a cylindrical Fermi surface. The dotted lines outline the Fermi surfaces.

2.1.7 Type-II Superconductors and the Vortex State

As presented in their original form, the above results pertain almost exclusively to type-I superconductors. The main topic of interest here however, is the magnetic properties of type-II superconductors, whose magnetization curve is depicted in Fig. 2.4. Below T_c, in the presence of an externally applied magnetic field H, three distinct phases are recognizable, dependent on the strength of the applied field. Below a *lower critical field* $H_{c1}(T)$ the superconductor is in the Meissner state with full expulsion of magnetic flux from its interior. For an applied field above an *upper critical field* $H_{c2}(T)$, magnetic flux fully penetrates the type-II material and returns it to its normal state. Within Ginzburg-Landau theory, the lower and upper critical fields may be written as:

$$H_{c1}(T) = \frac{\Phi_\circ}{4\pi\lambda(T)^2} \tag{2.20}$$

and,

$$H_{c2}(T) = \frac{\Phi_\circ}{2\pi\xi(T)^2} \tag{2.21}$$

respectively.

If the applied field lies between $H_{c1}(T)$ and $H_{c2}(T)$, there is a partial penetration of flux into the sample leading to regions in the interior which are superconducting and others which are in the normal state; this is often referred to as the *mixed state.* Ginzburg and Landau defined type-II superconductors as those with $\kappa > 1/\sqrt{2}$. The high-temperature superconductors are extreme type-II, with large GL parameters κ (*i.e.* $\lambda \gg \xi$), large upper critical fields $H_{c2}(T)$, and small lower critcal fields $H_{c1}(T)$ [32,33,34].

In 1957, the Russian physicist Alexei A. Abrikosov predicted the existence of type-II superconductors by considering the solution of the GL equations for $\kappa > 1/\sqrt{2}$ [35]. In particular, he considered the case where the externally applied magnetic field H is only

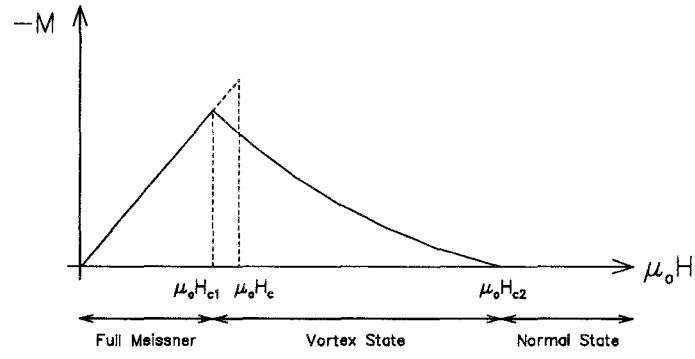

Figure 2.4: Magnetization curve for a type-II superconductor.

slightly below $H_{c2}(T)$; for in this region one obtains approximate solutions resembling those of the linearized GL equations [13]. The solutions revealed the presence of a periodic microscopic magnetic field distribution, transverse to the applied field. More precisely his efforts predicted a periodic square array of thin filaments of magnetic flux in the mixed state. Consequently, literature sometimes refers to the mixed state as the *Abrikosov regime* or for reasons to soon be made apparent, the *vortex state.*

In the core region of a filament, the magnetic field is high and the material does not superconduct here; that is these regions are in the normal state. The magnetic field is screened from the rest of the sample by supercurrents which circulate around each filament. It is common to refer to the filaments as *vortex lines* and the array of filaments as a *vortex lattice.* At the vortex center where the magnitude of the local field is largest, the density of superconducting electrons n_s and hence the order parameter $\Psi(\vec{r})$ is zero. As one moves radially out from the center of a vortex core, n_s increases and the supercurrents screen a greater amount of flux. At a radius on the order of the coherence length $\xi(T)$, n_s approaches the value in the bulk of the sample. It follows that the density of the supercurrents is greatest near the edge of the vortex core where the screening of the local magnetic field is at a maximum. Outside of the

vortex core, magnetic field leaks into the superconducting regions of the sample (see Fig. 2.5), in much the same way magnetic field penetrates the surface of the semi-infinite superconductor in Figure 1.2. The superconducting order parameter is, for all intents and purposes, constant beyond regions of the order $\xi(T)$ around the vortex cores [36]. It may be noted here that Abrikosov's prediction of the vortex state was remarkable in that it precluded any concrete experimenital proof of its existence. He derived the following relations between H_{c1}, H_{c2}, and the thermodynamic critical field H_c:

$$H_{c1} = \frac{H_c}{\kappa}(\ln \kappa - 0.27) \tag{2.22}$$

and,

$$H_{c2} = \sqrt{2}\kappa H_c \tag{2.23}$$

At a field H_{c2} the vortex cores begin to overlap and there is no longer any solution of the Ginzburg-Landau equation (*i.e.* the material returns to its normal state) [37]. H_{c1} marks the magnetic field at which it first becomes energetically favourable to have a flux line penetrate the superonductor.

In the dirty limit ($l \ll \xi_o$), one can write the upper critcal field as [14]:

$$H_{c2} = \frac{\sqrt{6}}{2}(\lambda_L/l)H_c = \frac{3\Phi_o}{2\pi^2\xi_o}\left(\frac{1}{l}\right) \tag{2.24}$$

Thus it is clear that increasing the impurity content of the superconductor and thus shortening the mean free path l results in a higher value of H_{c2} for the material.

One may wonder how London's magnetic penetration depth λ could be incorporated into a theory for type-II superconductors. Although London's original theory is indeed valid for $\lambda \gg \xi$, it makes no mention of an upper critical field $H_{c2}(T)$. Nevertheless, one could anticipate some extension of the London model applicable to type-II superconductors by consideration of specific features. To start with, F. London theoretically

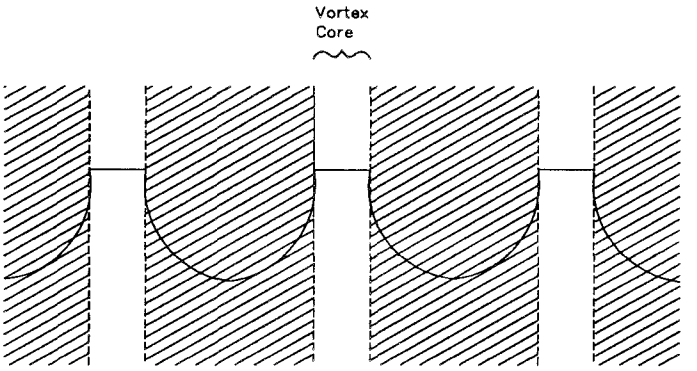

Figure 2.5: Magnetic flux leaking from the vortex cores where the field is highest into the surrounding superconducting regions (shaded area). The relative magnitude of the local magnetic field is depicted by the solid line.

predicted that magnetic flux is quantized in a superconducting annulus. An analogous treatment of the supercurrents that shield the vortex cores, leads one to deduce in several different ways [13,17], that the flux associated with each vortex is quantized and defined by:

$$\Phi_o = \frac{hc}{2e} = 2.07 \times 10^{-7}\text{G-cm}^2 \tag{2.25}$$

where Φ_o is called the *flux quantum*, h is Planck's constant and c is the speed of light. London's original calculation of the flux quantum Φ_o was off by a factor of 2. The reason for this was his unknown knowledge of Cooper pairs. Experiments done on superconducting rings verify Eq. (2.25) as the correct equation [15].

For an isolated vortex line, the field as determined in the extreme type-II limit $\kappa \gg 1$ is [35]:

$$B(r) = \frac{\Phi_o}{2\pi\lambda^2} K_o\left(\frac{r}{\lambda}\right) \tag{2.26}$$

where r is the distance from the axis of the vortex line, and K_o denotes a modified Bessel function of the second kind. For small distances ($\xi < r \ll \lambda$), from the vortex-line axis,

Eq. (2.26) reduces to [13]:

$$B(r) = \frac{\Phi_o}{2\pi\lambda^2} \ln\left(\frac{\lambda}{r}\right) \tag{2.27}$$

while further away ($r \gg \lambda$):

$$B(r) = \frac{\Phi_o}{2\pi\lambda^2}\sqrt{\frac{\pi\lambda}{2r}}e^{-r/\lambda} \tag{2.28}$$

The interaction between vortex lines becomes significant when their separation is $\leq \lambda$ [38]. In a type-II superconductor, the local magnetic field outside a vortex core decays in an exponential manner so that one is justified in describing the field in this region by the London equations. In a crude sense, the mixed state of a type-II superconductor may be visualized as a type-I superconductor with a regular array of normal state regions (*i.e.* the vortex cores) embedded in its interior. The magnetic penetration depth λ is then a measure of the length over which magnetic flux leaks into the superconducting regions that encompass the vortex cores.

The existence of the mixed state can be argued through free energy considerations. Consider a sample in an applied magnetic field $H_{applied}$ with a normal phase and a superconducting phase separated by a single interface. Realistically, the changeover between the two phases is not abrupt. Magnetic field leaks into the superconducting region a distance $\lambda(T)$, resulting in a contribution to the free surface energy of the interface that is negative. In addition, the order parameter $\Psi(\vec{r})$ decreases to zero over a distance $\xi(T)$, thereby decreasing the actual volume of the sample which superconducts. This leads to a positive-energy contribution at the interface. The sum of both phenomena give the net surface energy per unit length at the interface as [39]:

$$\sigma = \frac{1}{2}\mu_o H^2_{applied}\pi[\xi^2(T) - \lambda^2(T)] \tag{2.29}$$

A type-I superconductor where $\xi(T) > \lambda(T)$, has positive surface-energy; while type-II

superconductors with $\lambda(T) > \xi(T)$, have negative surface-energy. A more precise calculation in the context of GL-theory predicts that the sign of the surface energy changes at $\kappa = \lambda(T)/\xi(T) = 1/\sqrt{2}$ [17]. For a type-I superconductor in an applied field, the presence of normal-superconducting interfaces would increase the total free energy density because of positive surface-energy contributions. This situation is of course most unfavourable. For this reason, in the intermediate state of a type-I superconductor large normal regions will be formed which contain many flux quanta [13]. On the other hand, in the case of a type-II superconductor, negative surface-energy contributions from normal-superconducting interfaces would reduce the free energy density. Consequently, the total energy is minimized by introducing as many of these interfaces as possible. This is exactly what happens in the mixed state of a type-II superconductor.

It has been argued that the vortex model borne out of Abrikosov's solution of the Ginzburg-Landau equations is the most energetically favourable form for the magnetic flux to assume inside the superconductor [37]. Maximizing the surface-to-volume ratio of the normal regions leads to the lowest energy situation in the mixed state, because this provides the smallest positive surface-energy contribution. To achieve this, one can form normal regions which constitute either lamina of very small thickness ($\sim \xi$) or alternatively, filaments of small diameter ($\sim \xi$). Theoretical calculations indicate that the latter formation is lowest in energy for $\lambda \gg \xi$ [14].

Since Abrikosov's original prediction of a square vortex lattice, subsequent solutions of the GL equations for magnetic fields just below the upper critical field $H_{c2}(T)$, have convincingly shown that a periodic triangular array of vortex lines has the lowest free energy of all possible periodic solutions, and hence is the most stable configuration [13,40,41]. Decoration experiments which utilize small iron particles to make the vortices visible through an electron microscope have not only provided the best confirmation of the triangular arrangement but have also verified the flux quantum of Eq.

(2.25) [42]. It is clear from such experiments which verify the flux quantum that it is energetically more favourable to increase the number of vortices as one increases the magnetic field, rather than increasing the amount of flux in each vortex [37]. Thus in an isotropic type-II superconductor, the vortex lines repel one another as a result of the magnetic force between them, to form an equilateral triangular lattice in accordance with energy minimization.

2.2 The Pairing Mechanism

The mechanism responsible for superconductivity in the copper oxides is still a matter of serious debate. This section provides a qualitative comparison between the s-wave pairing state associated with conventional metallic superconductors and a proposed d-wave pairing mechanism for the high-temperature superconductors. The latter has attracted considerable attention in the past few years because it is experimentally verifiable. However, conflicting experimental results have left the nature of the pairing mechanism still very much a mystery. This chapter will avoid the rigorous mathematical details associated with each mechanism; the interested reader is referred to references within.

2.2.1 s-Wave Pairing

As touched upon earlier, conventional BCS superconductors are characterized by a standard *s-wave, spin-singlet* pairing state with $S = 0$, $L = 0$ Cooper pairs. The two electrons of a pair have equal and opposite momenta $\vec{k}$ and $-\vec{k}$, so that the centre-of-mass momentum of a Cooper pair is zero. For an attractive electron-electron interaction, the bound state is symmetric upon exchange of electron positions, so it must be an antisymmetric singlet upon exchange of electron spins to satisfy the Pauli exclusion principle. Thus, at any instant of time, one can think of the electrons in a Cooper pair as being in a state $(\vec{k}_i \uparrow, -\vec{k}_i \downarrow)$, and the wavefunction describing the pair consists of all states "i" occupied by the pair during its lifetime. An attractive interaction between two electrons results in a potential energy contribution which is negative, and thus lowers the total energy of the electron system. The negative potential energy associated with a Cooper pair is the *binding energy* of that pair.

In normal metallic superconductors, the attractive interaction between electrons originates from the electron-phonon interaction, which is short range and retarded in space-time [43]. The lattice deformation resulting from the first electron takes a finite time to relax, and thus a second electron can be influenced by the lattice deformation at a later time. The attraction arising from the electron-phonon interaction overcomes the screened Coulomb repulsion between electrons due to the presence of other electrons and ions in the solid [26]. This screening aids in reducing the natural Coulomb repulsion between two electrons, leading to an effective interaction which is relatively short range compared with the unscreened Coulomb potential [38].

The net effect of the attractive interaction on all the other electrons in the material renders the normal Fermi liquid state unstable. Consider the normal ground state of a metal in the absence of an attractive electron-electron interaction at $T = 0$K. The kinetic energy (and hence the total energy) of the system is minimized by requiring that the momenta of the plane wave states of the electrons fill up a sphere of radius $p_F = \hbar k_F$ (*i.e.* a Fermi sphere) in three-dimensional momentum space. Fig. 2.6(a) illustrates a Fermi sphere of radius k_F in three-dimensional k-space for a free electron gas at $T = 0$K. The corresponding normal density of states $N(E)$, where $N(E)dE$ is defined as the number of electron states with energy between E and $E + dE$, is shown in Fig. 2.6(b). $N(0)$ denotes the density of states at the Fermi surface at absolute zero.

Original BCS theory described superconductivity in metals, so that the Fermi surface was assumed spherical in the normal state. In the BCS ground state (*i.e.* the state of the superconductor at $T = 0$K), some of the electron states just outside the normal Fermi surface are occupied, and some just inside the Fermi surface are unoccupied. Certainly such an arrangement has a higher kinetic energy than does the normal state of the metal at $T = 0$K. However, the BCS ground state is in part comprised of Cooper

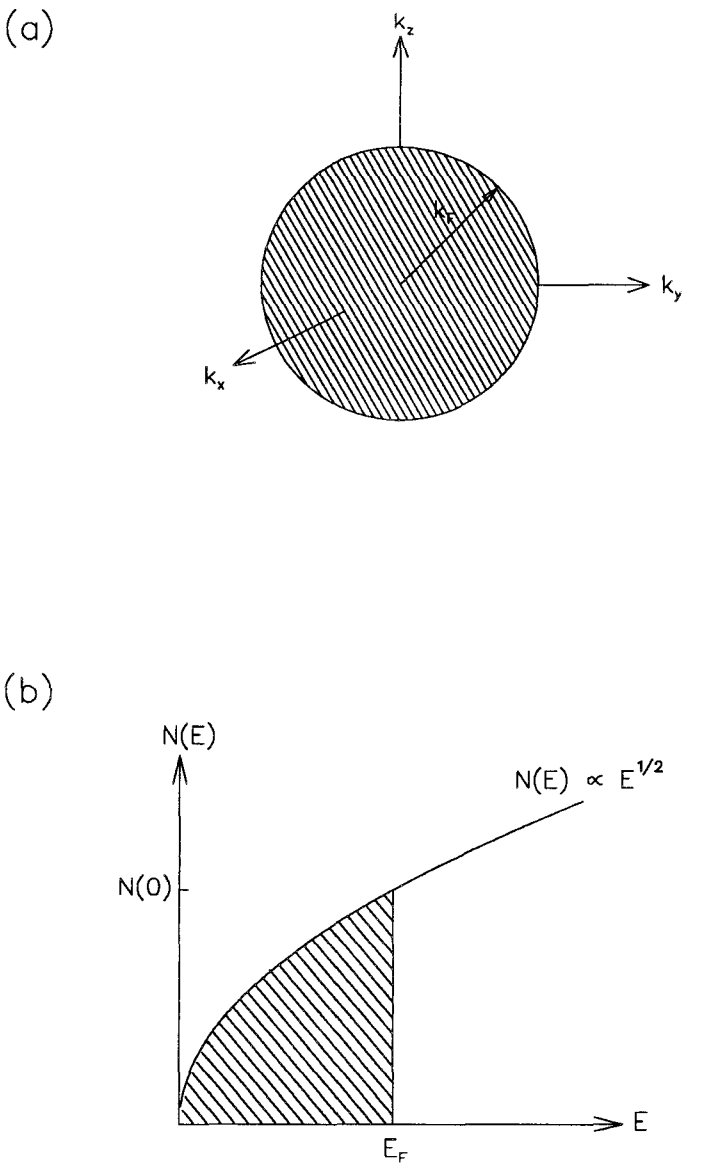

Figure 2.6: A metal at $T = 0$K. (a) The corresponding filled Fermi sphere. (b) The density of states.

pairs, the formation of which lowers the potential energy of the system. In the BCS ground state the arrangement of Cooper pairs is such that lowering of the potential energy outweighs the increase in kinetic energy, so that the BCS ground state has a lower total energy than that of the normal ground state [44].

As mentioned, the decrease in potential energy is due to the phonon-induced, electron-electron attractive interaction. The phonon-induced attractive force scatters Cooper pairs from one state $(\vec{k}\uparrow, -\vec{k}\downarrow)$ to another state $(\vec{k}'\uparrow, -\vec{k}'\downarrow)$. An electron occupying state $(\vec{k}\uparrow)$ near the Fermi surface vibrates the lattice resulting in the emission of a phonon of wave vector $\vec{q}$. The electron is thereby scattered to a state $(\vec{k}'\uparrow)$, where $\vec{k}' = \vec{k} - \vec{q}$. A second electron occupying state $(-\vec{k}\downarrow)$, absorbs the phonon thus scattering to a state $(-\vec{k}'\downarrow)$, where $-\vec{k}' = -\vec{k} + \vec{q}$. The total centre-of-mass momentum in the final state is thus $\vec{K} = \vec{k}' + (-\vec{k}') = 0$, which is unaltered from before the scattering process. The two electrons forming a Cooper pair are continually scattered between states with equal and opposite momentum. Since only the total centre-of-mass momentum is conserved in such scattering processes, the momenta of the individual electrons is continually changing, so that one cannot explicitly assign a single momentum to each electron in the pair.

Each scattering process reduces the potential energy of the electron system further. The negative potential energy contribution is greatest for scattering between states of equal and opposite momentum [39]. The range of momenta available to the scattered electrons in the ground state is dictated by the energy of the phonon and the Pauli exclusion principle. The phonon-induced attractive interaction can only affect those electrons in the vicinity of the Fermi surface. Electrons further inside the Fermi sphere cannot scatter to other levels because of the Pauli exclusion principle. To scatter electrons well below the Fermi level into unoccupied states would require phonon

frequencies much larger than that generated from the electron interaction with the lattice. Electrons closer to the Fermi surface may form Cooper pairs; however, as they do so the number of states available to the scattering electrons decreases. As the number of scattering events decreases, so does the maximum amount by which the potential energy of the system can be lowered. The formation of Cooper pairs must then cease at the moment the increase in kinetic energy due to moving electrons above the Fermi level exceeds the amount by which the potential energy is lowered. This limit then specifies the arrangement of the BCS ground state.

One of the most distinctive consequences of BCS theory is that an energy gap opens up between the ground state and the lowest excited state. As shown in Fig. 2.7(a), the energy gap $\Delta(\vec{k})$ has the same symmetry as the Fermi surface of the normal state. The important feature in s-wave pairing is that the wave vector dependence of the energy gap is finite everywhere on the Fermi surface at temperatures below T_c.

As the temperature is increased above $T = 0$K, thermally excited phonons become available to scatter the electron pairs. Because of the energy gap in the excitation spectrum, excitations cannot occur with an arbitrarily small amount of energy as in the case of a normal metal. Phonons with energy comparable to twice the energy gap (2Δ) will scatter electrons in a Cooper pair to states above the gap. The electrons from the pair will no longer have equal and opposite momentum, so that their interaction potential becomes negligible and the Cooper pair is destroyed. Of course at low temperatures, the density of phonons with this much energy is small. Near T_c on the other hand, phonons with energy on the order of the energy gap are plentiful, and pair breaking is greatly enhanced. In addition, the gap itself is temperature dependent and can be well approximated by [15]:

$$\frac{\Delta(T)}{\Delta(0)} = \tanh\left[\frac{T_c}{T}\frac{\Delta(T)}{\Delta(0)}\right] \tag{2.30}$$

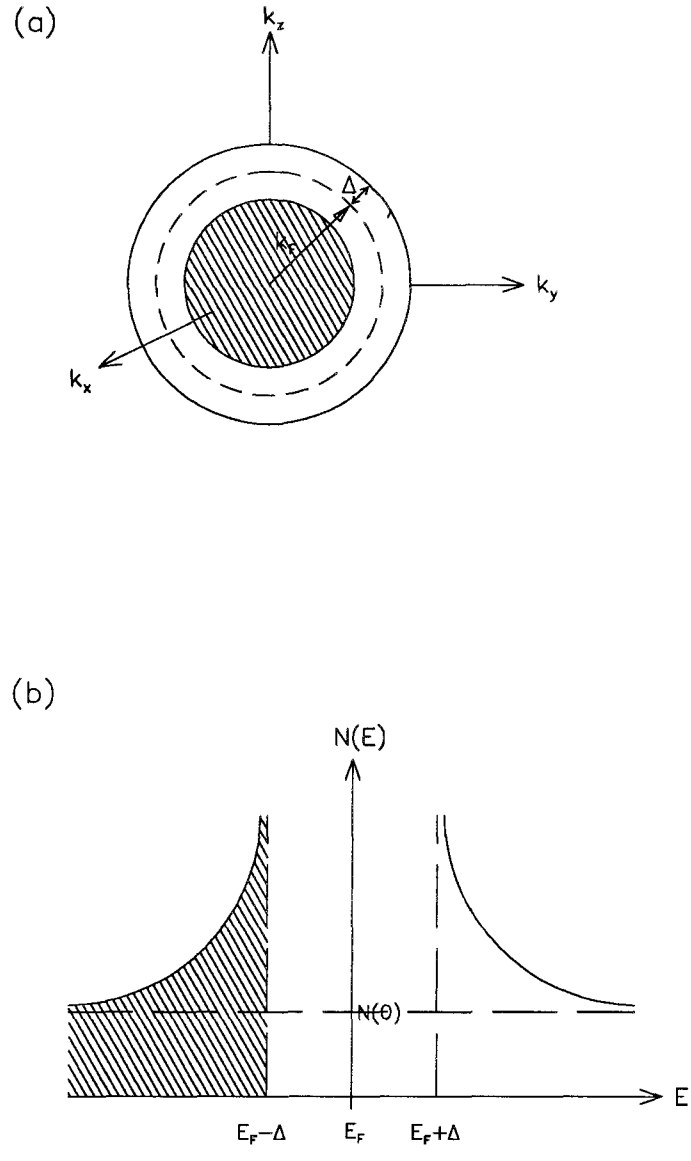

Figure 2.7: A BCS superconductor at $T = 0$K. (a) The Fermi surface (dotted line) for the groundstate. (b) The corresponding density of states. The shaded region represents the occupied states of the superconducting electrons.

except near T_c where Eq. (2.18) better describes the behaviour. As T increases, the amplitude and frequency of the lattice-ion movement increases. This disrupts the propagation of the phonons between correlated electron pairs, resulting in a weakening of the attractive interaction and a corresponding reduction in the size of the energy gap [45].

Fig. 2.7(b) and Fig. 2.8 show the associated density of quasiparticle states $N(E)$ at $T = 0$K and T slightly above absolute zero, respectively. The states which are no longer occupied between $E_F - \Delta$ and $E_F + \Delta$ pile up on the edges of the gap region. Above the energy gap, the electrons are often referred to as *normal electrons* or *quasiparticles*. That is, if an electron occupies a state $(\vec{k} \uparrow)$ then the state $(-\vec{k} \downarrow)$ need not be occupied. The corresponding density of quasiparticles (*i.e.* the *normal fluid density*) is usually denoted n_n. Below the energy gap the electrons are paired. These electrons are referred to as *superconducting electrons*, and their associated density (*i.e.* the *superfluid density*) is denoted n_s. At $T = 0$K all the electrons are superconducting, while for $T \geq T_c$ they are all normal. For temperatures in between, the system is a mixture of superconducting and normal electrons.

2.2.2 The Motivation for an Alternative Pairing Mechanism

For the high-T_c superconductors, there are several experimental and theoretical reasons for seriously questioning traditional BCS theory with a simple phonon-induced electron-electron interaction. Experimentally, an extremely small isotope effect measured for $YBa_2Cu_3O_{7-\delta}$ is often cited as one such deterrent [17]. BCS theory predicts an isotope shift if T_c is determined by the motion of the oxygen ions; however, substitution of ^{18}O for ^{16}O in $YBa_2Cu_3O_{7-\delta}$ does not significantly change T_c. Ruling out a phonon-induced pairing mechanism based on these observations is premature however. The presence of an isotope shift implies that the lattice is certainly involved in the pairing

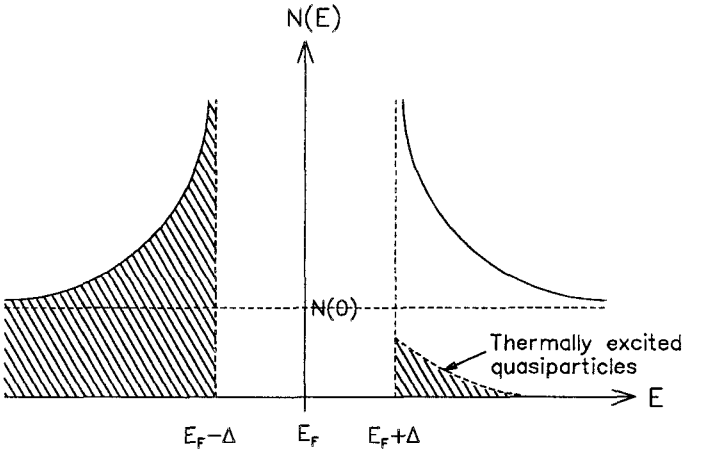

Figure 2.8: The density of states for a BCS superconductor at $T > 0$K. As T is increased above absolute zero, Cooper pairs are broken and the resulting normal electrons occupy states above $E_F + \Delta$.

mechanism. However, one cannot assume that the lack of an isotope effect necessarily implies that the pairing mechanism does not involve phonons. Superconductors such as ruthenium and zirconium exhibit virtually no isotope effect, while uranium shows a negative isotope effect [46]. The problem is that there are many additional factors which can effect the strength of the isotope shift. Thus, by itself the lack of a significant isotope effect in $YBa_2Cu_3O_{7-\delta}$ is not enough to rule out an electron-phonon mechanism.

The anomalous normal-state properties of the cuprates suggest that these materials are not just a normal Fermi liquid above T_c, and therefore may not be adequately described by BCS theory below T_c. The electrical dc resistivity $\rho(T)$, exhibits a linear dependence in temperature over a wide range of temperatures above T_c. For a conventional Fermi liquid associated with normal metals, $\rho(T) \sim T^2$. This is a manifestation of the long lifetime of electrons near the Fermi surface in a conventional Fermi liquid [47]. The nuclear spin-lattice relaxation rate $T_1^{-1}(T)$ shows a temperature dependence

substantially different from that of normal metals. Other anomalous normal-state properties of the copper-oxide superconductors include the thermal conductivity $\kappa(T)$, the optical conductivity $\sigma(\omega)$, the Raman scattering intensity $S(\omega)$, the tunneling conductance as a function of voltage $g(V)$, and the Hall coefficient $R_H(T)$ [48]. All of these normal-state properties are quite uncharacteristic of the Fermi liquid usually associated with the normal state of conventional superconductors. In fact, it is possible that the unusual normal-state properties of the high-T_c compounds cannot be appropriately described by a Fermi liquid.

Some argue on theoretical grounds that BCS theory cannot explain the high transition temperatures of the cuprates. For example, it has been suggested that an electron-phonon mechanism probably cannot account for transition temperatures in excess of 40 to 50K [49]. The magnitude of the electron-phonon interaction required to generate a T_c comparable to that of $YBa_2Cu_3O_{7-\delta}$, would substantially weaken the lattice. This structural instability would greatly reduce the density of electron states at the Fermi surface and hence destroy superconductivity [18]. This argument is not accepted by all. It has been suggested that the calculations leading to the above conclusion are not valid, so that an electron-phonon mechanism may still be the basis for superconductivity in the high-temperature superconductors [50].

2.2.3 *d*-Wave Pairing

It is plausible that the notion of Cooper pairing and BCS theory may still be applicable to the high-temperature superconductors, yet the nature of the pairing mechanism may be something other than the phonon-induced electron-electron interaction. The formation of a bound state can be achieved by any attractive interaction capable of overcoming the natural Coulomb repulsion between two electrons. Several alternative sources for this attractive force which are compatable with conventional BCS theory

have been proposed. One such mechanism, which has received much attention in recent years, is an electron-electron interaction mediated by magnetic spin fluctuations [51,52,53]. The concept is not entirely new. A similar process is believed to help facilitate p-wave spin-triplet pairing ($L = 1$, $S = 1$) in superfluid ^{3}He, and to lead to other pairing states in certain organic superconductors and heavy fermion systems such as UPt_3 [49,53].

The antiferromagnetic state of the parent materials such as $YBa_2Cu_3O_6$ and the anomalous normal-state properties of the high-T_c superconductors provide the inspiration for attempts at describing the superconducting properties in terms of a spin-fluctuation exchange mechanism [52,53,82]. A logical starting point for such a theory is to suggest that the physical origin of those normal-state features which differ from normal metals may somehow be responsible for superconductivity in the cuprates. It has been suggested that the measured anomalous normal-state properties of $YBa_2Cu_3O_{7-\delta}$ stem from strong antiferromagnetic correlations of spins, and these same antiferromagnetic spin fluctuations are also responsible for superconductivity in the cuprates [1]. NMR measurements of the normal state have been successfully modelled with a nearly antiferromagnetic Fermi liquid [55,56,57].

Some insight into the origin of possible antiferromagnetic spin fluctuations in the superconducting phase of $YBa_2Cu_3O_{7-\delta}$ may be obtained by examination of the antiferromagnetic insulating compound $YBa_2Cu_3O_6$. The structures of $YBa_2Cu_3O_6$ and $YBa_2Cu_3O_7$ appear in Fig. 2.9 and the phase diagram for $YBa_2Cu_3O_x$ ($6 < x < 7$) appears in Fig. 2.10. In reference to Fig. 2.9(a), the Cu(1) or Cu-O *chain layer* of $YBa_2Cu_3O_6$ consists entirely of Cu^{1+} ions. The singly ionized Cu ions have no magnetic moment. Oxygen doping places O ions along the b-axis, resulting in a progressive conversion of Cu^{1+} into Cu^{2+} with the development of holes in the $3d$-shell of the Cu ions [59].

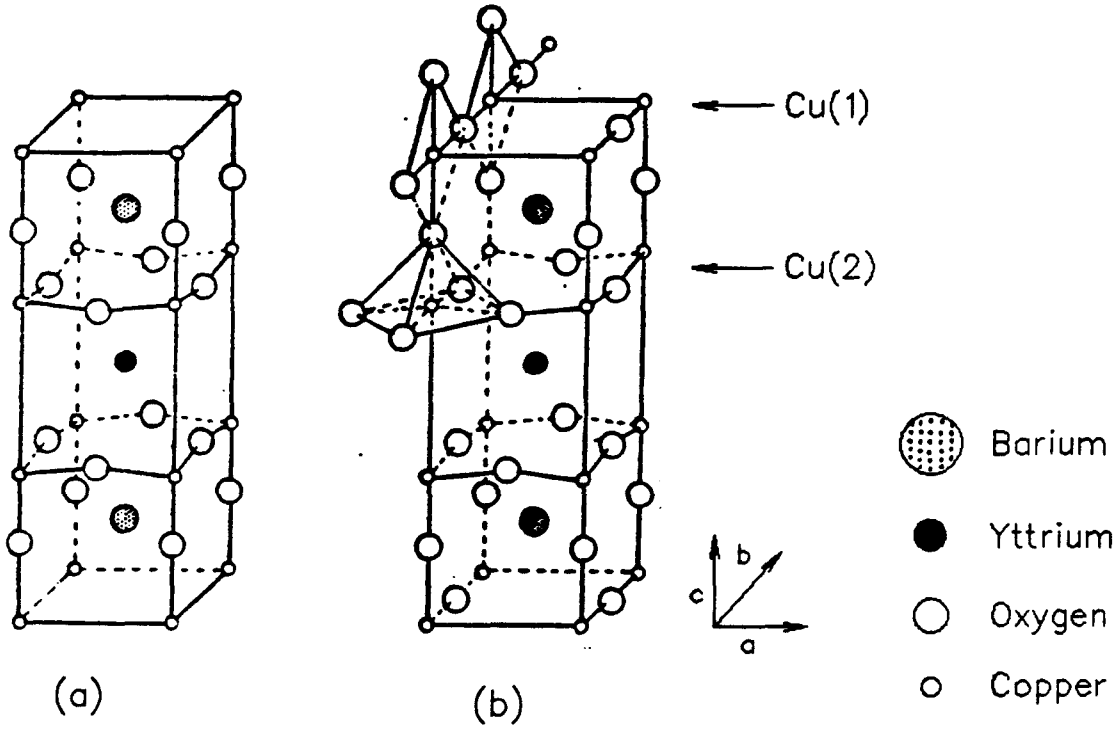

Figure 2.9: (a) The structure of the insulator $YBa_2Cu_3O_6$ and (b) the structure of the superconductor $YBa_2Cu_3O_7$ [18].

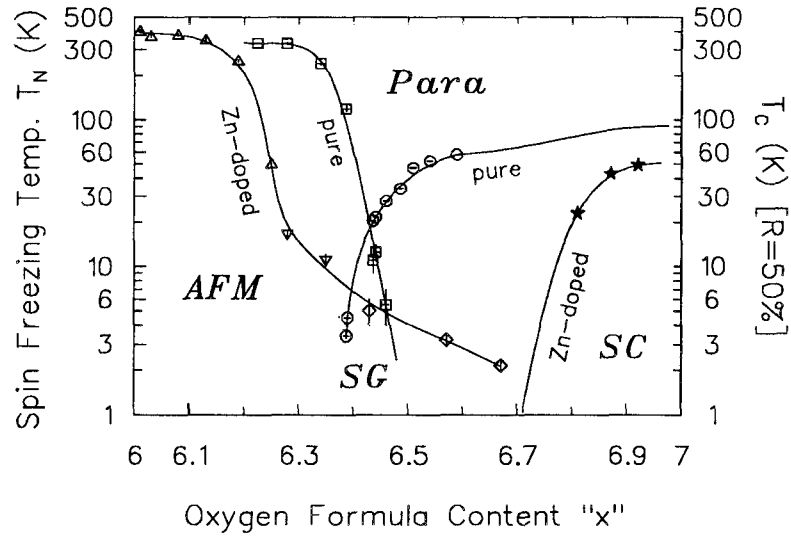

Figure 2.10: Phase diagram for $YBa_2Cu_3O_x$, as a function of oxygen formula concentration x. Also shown is the phase diagram for a Zn-doped sample [58].

The Cu(2) or CuO_2 *planes* of $YBa_2Cu_3O_6$ have predominantly Cu^{2+} ions. Each Cu gives up two electrons; an electron from the $4s$-shell and the other from the $3d$-shell. The absence of an electron in the $3d$-shell (a hole) results in a net magnetic moment (spin) on the Cu ions in this layer. Oxygen cannot easily be removed or added to the CuO_2 planes. The oxygen concentration can be varied appreciably only in the Cu-O chains. As mentioned, adding oxygen converts the copper ions in the Cu-O chains from Cu^{1+} to Cu^{2+}. Beyond $x \approx 6.5$ it is believed that adding oxygen is equivalent to adding holes to the CuO_2 planes. The oxygen which is randomly added to the chains becomes O^{2-} by trapping two electrons which are believed to originate from the creation of two holes in the oxygens of an adjacent CuO_2 plane. However, Hall coefficient measurements suggest that holes may also be forming in the chains [23].

Neutron difffraction and muon precession experiments indicate that the Cu moments are antiferromagnetically aligned in $YBa_2Cu_3O_6$ below the Neel temperature T_N

(see Fig. 2.10). The Cu^{2+} spins (*i.e.* spin 1/2 holes) in the CuO_2 planes are coupled antiferromagnetically through a superexchange process with the oxygen ions. The O^{2-} ions themselves have no net magnetic moment. At sufficiently low temperatures, the Cu ions in the chains also become antiferromagnetically ordered and couple with the Cu^{2+} ions in adjacent CuO_2 planes [18]. In view of this, the Cu^{1+} labelling of the chain layer Cu ions may not be entirely accurate. Neutron and Raman scattering experiments suggest that the exchange interactions within the CuO_2 planes are much greater than the coupling between adjacent layers. This is likely due to the greater separation between Cu ions in the vertical direction and a lack of O^{2-} ions between adjacent CuO_2 planes. The difference between strengths of the interplanar and intraplanar couplings means that $YBa_2Cu_3O_6$ exhibits a quasi two-dimensional magnetic behaviour. Furthermore, the measured maximum magnetic moment on the Cu ions is substantially smaller than what one would expect for a localized Cu^{2+} ion. This may be due to the enhanced thermal fluctuations associated with a two-dimensionally ordered system [18].

It is a widely accepted belief that the electrons responsible for conduction in the copper-oxide superconductors are more or less confined to the CuO_2 planes [52]. If this is the case then it is plausible that these electrons are paired by way of a two-dimensional system of antiferromagnetic spin fluctuations. The next obvious question to ask is,

"Do these spin fluctuations persist in the superconducting phase?"

Raman and neutron scattering measurements suggest that the magnetic fluctuations do indeed survive into the superconducting state. The spin-correlation length is substantially diminished in the superconducting state, but the amplitude of the magnetic moments is not greatly diminished [18]. Furthermore, NMR data taken above T_c indicate the presence of two-dimensional antiferromagnetic spin fluctuations arising from the nearly localized Cu^{2+} d-orbitals in the CuO_2 planes.

It is difficult to give an intuitive description of pairing due to spin-fluctuation exchange. It is clear that a single hole will help destroy the antiferromagnetic order. However it is less clear whether it will attract or repel a second hole with the same or opposite spin. The answers to these questions seem to depend very much on the regions of k-space and r-space considered [60].

Weak-coupling calculations of the normal and superconducting state properties have been carried out [1,57,82] for an antiferromagnetic spin-fluctuation induced interaction between quasiparticles on a two-dimensional square lattice. Such a two-dimensional model is at best an approximation to the behaviour of the three-dimensional $YBa_2Cu_3O_{7-\delta}$ compound. Nevertheless, these calculations yield a value of the transition temperature T_c which is near 90K and a superconducting pairing state with $d_{x^2-y^2}$ symmetry. For this pairing state the energy gap is of the form:

$$\Delta(\vec{k}, T) = \Delta_o(T) \mid \cos(k_x a) - \cos(k_y a) \mid \tag{2.31}$$

where $\Delta_o(T)$ is the maximum value of the energy gap at temperature T and a is the lattice constant or distance between nearest neighbor Cu atoms in the plane. The angular momentum and spin of a Cooper pair is $L = 2$ and $S = 0$, respectively (*i.e. singlet* $d_{x^2-y^2}$ pairing).

The superconducting gap originating from the spin-fluctuation mediated interaction has a momentum (or k) dependence, in contrast to the phonon-frequency dependence of the gap associated with an electron-phonon interaction. It is clear from Eq. (2.31) that the excitation gap vanishes when $|\hat{k}_x| = |\hat{k}_y|$. Fig. 2.11 shows the four nodes which result along the diagonals in the Brillouin zone at the Fermi surface. In three-dimensional k-space the gap vanishes along four nodal lines running parallel to the k_z-axis for a cylindrical Fermi surface, or along four nodal lines joining the *north* and *south* poles for a spherical Fermi surface (see Fig. 2.12). Because of these nodal lines,

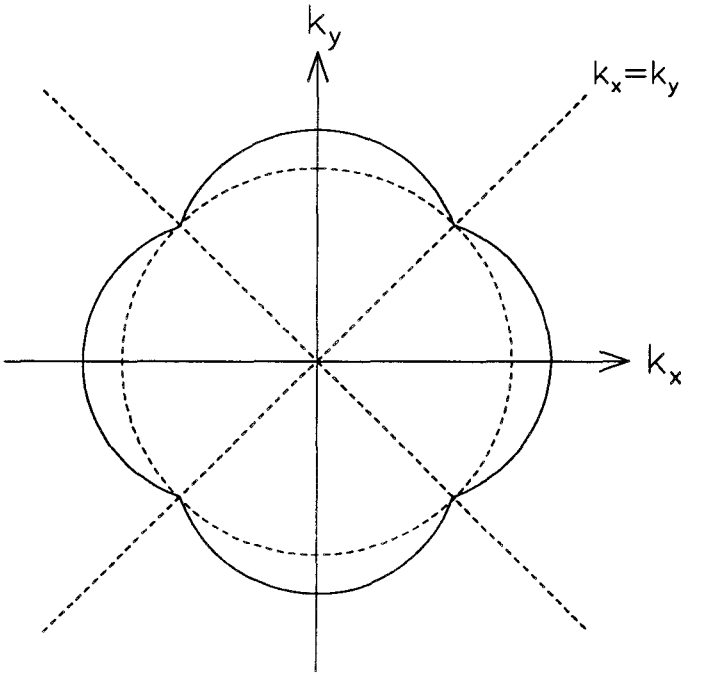

Figure 2.11: The the energy gap for $d_{x^2-y^2}$ symmetry. The gap is largest along the k_x and k_y-directions. Nodes exist at the Fermi surface (dashed circle) along $|k_x| = |k_y|$.

there will be considerably more quasiparticle excitations at low temperatures compared to conventional s-wave superconductors. Thus even at $T = 0$K there is a quasiparticle contribution to the supercurrent [61]. For $YBa_2Cu_3O_{7-\delta}$ which is highly anisotropic, a cylindrical Fermi surface with no gap in the k_z direction seems like a plausible description. However, it has been suggested that the cross-section of the Fermi surface in $YBa_2Cu_3O_{7-\delta}$ is not a perfect circle. If this is the case, then the pairing state can have d-wave symmetry but not give rise to nodes in the gap [49].

To gain a qualitative understanding of the symmetry in Fig. 2.11, consider the two-dimensional square lattice of antiferromagnetically ordered spins depicted in Fig. 2.13.

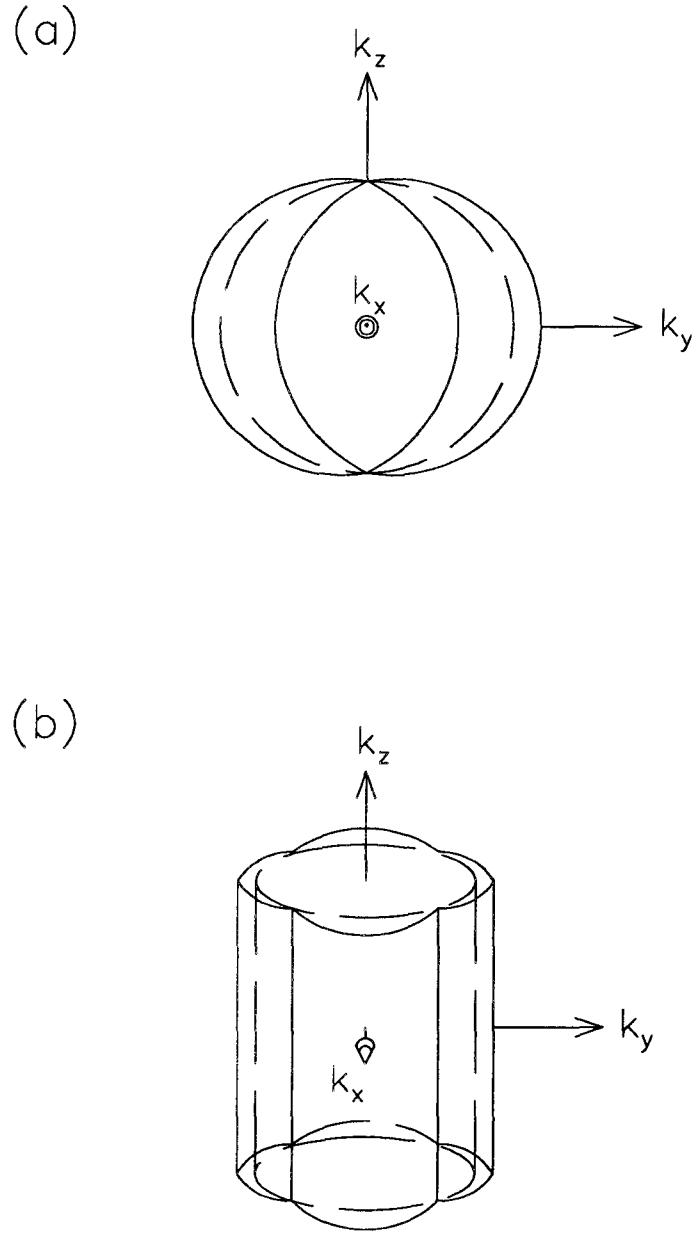

Figure 2.12: $d_{x^2-y^2}$-symmetry for a (a) spherical Fermi surface and (b) a cylindrical Fermi surface. The Fermi surfaces are shown as dashed lines.

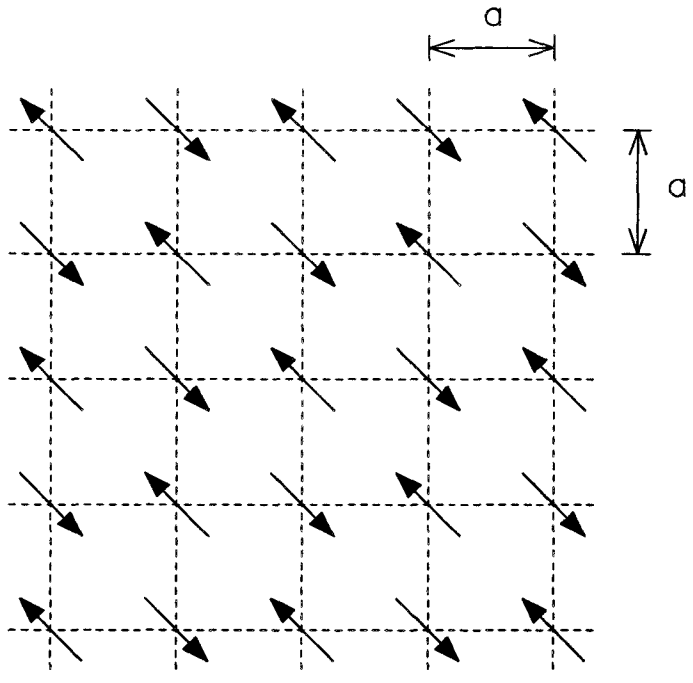

Figure 2.13: A square lattice of antiferromagnetically arranged spins.

In real space nearest-neighbor spins are separated by the lattice constant a. Such an arrangement is a simplified model of the CuO_2 planes in $YBa_2Cu_3O_7$. In the $YBa_2Cu_3O_7$ compound, $a \approx b$, so that the CuO_2 planes are almost square and the localized spins of Fig. 2.13 correspond to the antiferromagnetically-correlated spin fluctuations associated with the Cu^{2+} d-orbitals. In the derivation of Eq. (2.31), a spin-spin correlation function (electronic spin susceptibility) was chosen which gave a good quantitative fit to NMR measurements of the Knight shift and the spin-lattice relaxation rates of ^{63}Cu, ^{17}O and ^{89}Y nuclei in $YBa_2Cu_3O_7$ [82]. The electronic spin susceptibility is representative of the strength of the spin-fluctuation-mediated pairing potential. This function is strongly peaked at the *nesting* wave vector $\vec{Q} = (\pm\frac{\pi}{a}, \pm\frac{\pi}{a})$ in the first Brillouin zone. For an s-wave gap, the electronic spin susceptibility is suppressed at $(\pm\frac{\pi}{a}, \pm\frac{\pi}{a})$ [2].

To understand the significance of $\vec{Q}$, consider first the phase-space restrictions on the electron-electron scattering rate for a conventional electron gas assuming a cylindrical Fermi surface. At $T = 0$K the Fermi cylinder is full and there are no electrons to scatter from such that energy and momentum are conserved. For $T > 0$K, an excited electron with energy different than E_F can scatter into a shell of partially occupied levels centered about E_F in $\vec{k}$-space. That is to say, the range of momenta available to the scattered electron is proportional to the temperature T [47]. This situation is depicted in two dimensions in Fig. 2.14(a), where the incoming quasiparticle momenta are $\vec{k}$ and $-\vec{k}$. Any interaction between electrons changes the momenta of the quasiparticles such that $\vec{k}' \approx \vec{k} \pm \vec{q}$. Any orientation of the wave vector $\vec{q}$ in Fig. 2.14(a) will yield the same available phase space for electron scattering near the Fermi surface at a temperature T.

Consider now a nearly antiferromagnetic Fermi liquid with nesting vector $\vec{Q}$ as shown in Fig. 2.14(b). In this nested-Fermi liquid, two electrons with momenta $(\vec{k}, -\vec{k})$ near the Fermi surface exchange the antiferromagnetic spin fluctuation which has a sharp peak at $\vec{Q}$. The two electrons are subsequently scattered (by the oscillating potential set up by the corresponding spin density wave) to states with wave vectors $(\vec{k}', -\vec{k}')$ near opposite sides of the Fermi surface. In this case $\vec{k}' \approx \vec{k} \pm \vec{Q}$. As illustrated in Fig. 2.14(b), the range of momenta available to the scattering electron is greater than in the conventional Fermi liquid of Fig. 2.14(a). For all $\vec{k} - \vec{k}' \equiv \vec{Q}$ parallel to the wave vectors $(\pm\frac{\pi}{a}, 0)$ and $(0, \pm\frac{\pi}{a})$, the available phase space for scattering is the same. As $\vec{k} - \vec{k}' \equiv \vec{Q}$ is rotated away from these directions, the range of momenta available to the scattering electron decreases so that it is smallest when $\vec{Q} = (\pm\frac{\pi}{a}, \pm\frac{\pi}{a})$. The evolution of the wave vector $\vec{k} - \vec{k}'$ in Fig. 2.14(b) maps out the gap function of Fig. 2.11. This is demonstrated in Fig. 2.15. As $\vec{k} - \vec{k}'$ is rotated away from $(\pm\frac{\pi}{a}, 0)$ or $(0, \pm\frac{\pi}{a})$, the

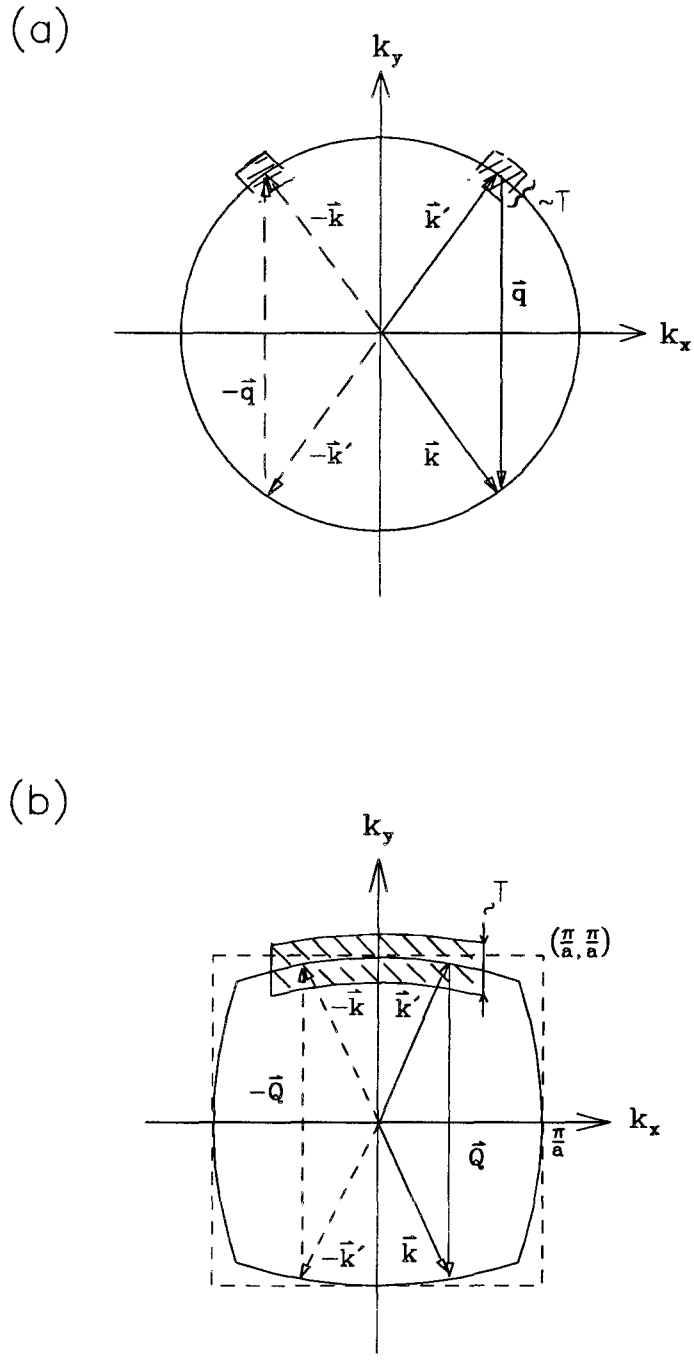

Figure 2.14: Phase space available for electrons scattered from the state $(\vec{k}, -\vec{k})$ to the state $(\vec{k}', -\vec{k}')$ at temperature T. (a) An electron gas system with a weak attractive interaction. (b) A nested Fermi liquid. The dashed square represents the first Brillouin zone. In both cases the Fermi surface is indicated by a solid line. The shaded regions indicate the available phase space which is proportional to T.

range of momenta available to scatter into decreases and so does the magnitude of the energy gap.

It should be noted that there are theories which predict $d_{x^2-y^2}$-wave pairing which are not based on spin fluctuations [28]. Considering these, it seems appropriate to discuss $d_{x^2-y^2}$ symmetry as it pertains to the Fermi-surface geometry, rather than to introduce the details of the theoretical calculations which predict $d_{x^2-y^2}$-wave pairing from antiferromagnetic spin fluctuations. The orientation of the Fermi surface in Fig. 2.14(b) and Fig. 2.15 is that used to explain commensurate peaks at $(\pm\frac{\pi}{a}, \pm\frac{\pi}{a})$ in neutron experiments involving $YBa_2Cu_3O_7$ [62]. The corners of the Fermi surface are actually more rounded than they appear in these figures. The Fermi surface for $La_{2-x}Sr_xCuO_4$ has more curvature in the sides and is rotated 45° from that of $YBa_2Cu_3O_{6.95}$ so that incommensurate peaks are observed at $(\pm\frac{\pi}{a}, \pm\frac{\pi}{a})$ in neutron experiments.

Returning to $YBa_2Cu_3O_{6.95}$ and the notion of spin fluctuations, if one assumes that a given oxygen nucleus is coupled predominantly to the spins on its two nearest-neighbor Cu sites, then the Cu spin-density of states is greatest near the Brillouin zone corners $(\pm\frac{\pi}{a}, \pm\frac{\pi}{a})$ [56]. Also since the O nucleus is resting between two oppositely directed Cu spins, the transferred hyperfine field from the Cu moments cancels at the O site so that the spin density vanishes there. Thus the Cu spins relax the O nuclei so that the dominant contribution to the spin susceptibility comes from the Cu^{2+} d-orbital spin states. Thus low temperature excitations may result from the influence of the Cu spins on the superconducting carriers.

Opponents of the spin-fluctuation mechanism have argued that the measured quasiparticle lifetimes in $YBa_2Cu_3O_7$ are much too short for the quasiparticles to take advantage of this sort of interaction [53]. Strong-coupling calculations (which normally imply

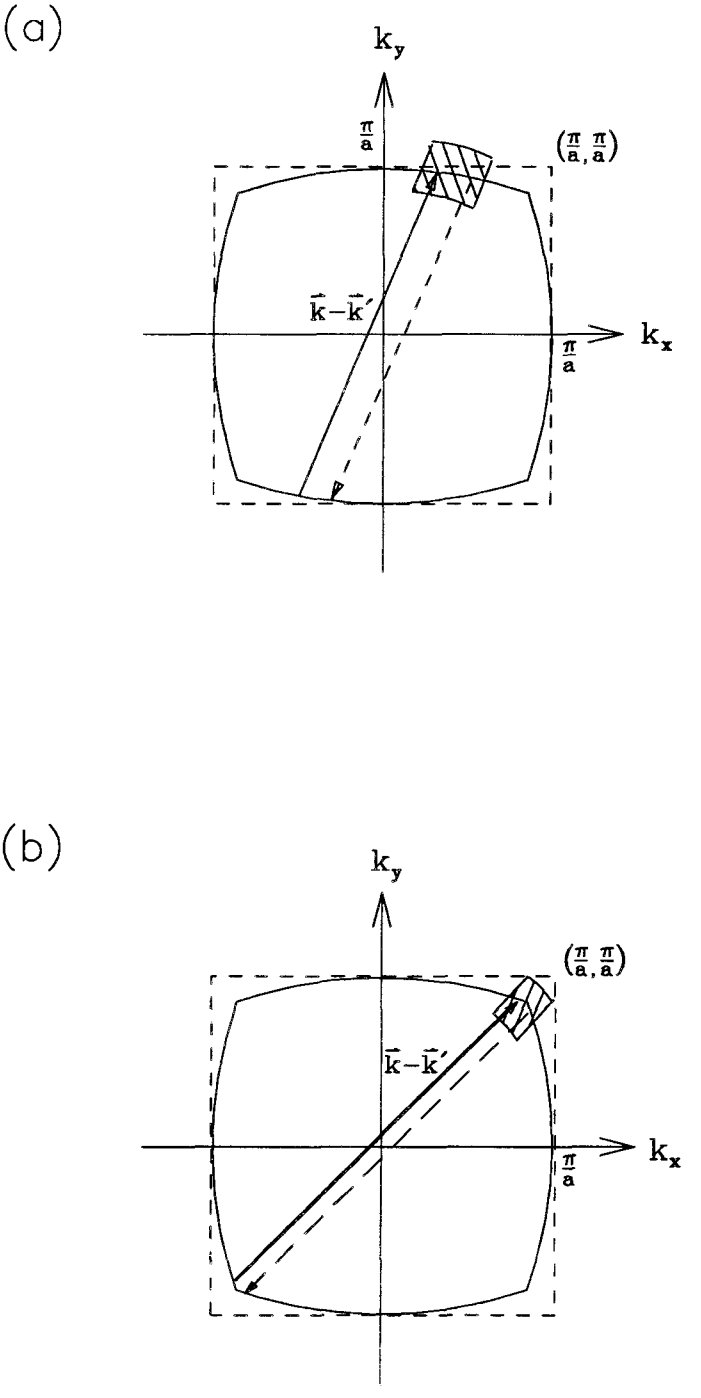

Figure 2.15: The dependence of the available phase space on the scattering wave vector $\vec{k} - \vec{k}'$. As the phase space decreases, the energy gap increases so that it is at its maximum in (b). The dashed square represents the first Brillouin zone and the Fermi surface is indicated by a solid line.

a short quasiparticle lifetime) have been carried out. Results show that one still obtains a T_c of 90K for $YBa_2Cu_3O_7$, with a $d_{x^2-y^2}$ pair gap [53]. Subsequent calculations of the anomalous normal-state quasiparticle properties in the corresponding strong-coupling regime have also been done [53,63]. Results are consistent with experimental measurements, indicating that the strong-coupling calculations are reasonable.

Theoretically a d-wave pairing state is appealing because it avoids the strong on-site Coulomb repulsion which is inherent in an s-wave pairing state. Also a spin-fluctuation pairing mechanism for the high-T_c superconductors would not lead to a lattice instability as may occur for an extremely strong electron-phonon interaction. Unfortunately it is yet to be shown if the $d_{x^2-y^2}$ symmetry evolves out of calculations for oxygen concentrations less than in $YBa_2Cu_3O_7$. Also a complete microscopic theory for $d_{x^2-y^2}$ pairing is still unavailable. On the experimental front, attempts at determining the pairing state in the copper-oxide superconductors have been conflicting and inconclusive.

2.3 Anisotropy in $YBa_2Cu_3O_{7-\delta}$

2.3.1 General Considerations

The electronic properties of high-T_c superconductors are extremely anisotropic. Consequently theories which describe their behaviour must be able to distinguish between the motion of the superconducting carriers in different directions. For $YBa_2Cu_3O_{7-\delta}$, the crystal structure is orthorhombic (see Fig. 2.9). The layered crystal structure of $YBa_2Cu_3O_{7-\delta}$ results in a strong $\vec{a}$-$\vec{c}$ anisotropy, while the orthorhombic distortions due to the Cu-O chains introduce another $\vec{a}$-$\vec{b}$ anisotropy. The anisotropic nature of various physical quantities measured in single crystals of $YBa_2Cu_3O_{7-\delta}$ have been well documented. For instance, the electrical resistivity along the $\vec{a}$ and $\vec{c}$-directions of the unit cell varies linearly with temperature, while along the $\vec{b}$-direction there is a distinct upward curvature for increasing temperature, which has been attributed to conductivity along the Cu-O chains [64,65]. Critical-field, critical-current and magnetic penetration depth measurements in $YBa_2Cu_3O_{7-\delta}$ also exhibit strong anisotropy. The anisotropy of the magnetic penetration depth λ in the uniaxial high-T_c materials is a direct consequence of the superconducting currents not being isotropic [66]. In addition to the penetration depth exhibiting a large $\vec{a}$-$\vec{c}$ anisotropy, recent measurements on untwinned $YBa_2Cu_3O_{6.95}$ single crystals show a small but significant $\vec{a}$-$\vec{b}$ anisotropy [10].

2.3.2 Anisotropy of the Magnetic Penetration Depth

In experiments to determine λ, single crystals are much preferred over polycrystalline samples. This is true for several reasons. Because $YBa_2Cu_3O_{7-\delta}$ is strongly anisotropic, the orientation of the sample in the applied field is significant. With single crystals one has control over this feature. By positioning the single crystal with its c-axis parallel

to the applied field, one can readily proceed to determine the magnetic penetration depth in the *ab*-plane (or Cu-O plane), λ_{ab} (or $\lambda_{||}$). In an analogous fashion, suitable orientation of the single crystal in the applied field in principle allows measurement of λ_c or $\lambda_\perp$ (*i.e.* the magnetic penetration depth perpendicular to the Cu-O planes). This is much more difficult to perform experimentally, however, since the crystals grow in such a way that the $\vec{a}$-$\vec{b}$ dimensions are much greater than in the $\vec{c}$-direction.

With polycrystalline samples, the principal axis of each grain is randomly oriented with respect to the applied field. Consequently one must average over all possible orientations of the *c*-axis to simulate the field distribution and then try to extract a value for the magnetic penetration depths λ_{ab} and λ_c. This could be difficult, since different combinations of values of λ_{ab} and λ_c may give similar line shapes.

Further considerations attached to the use of powdered samples include the dissimilarity in shape of the individual grains. Consequently, each grain has a different demagnetization factor and thus a slightly different average field. This leads to an additional broadening of the field distribution, which if not properly taken into account will lead to an underestimate of the magnetic penetration depth.

In general, the magnetic penetration depth in an anisotropic superconductor is determined by replacing the effective mass m^* of the superconducting electrons by an effective-mass tensor $\mathbf{m}^*$ [67]. Until very recently, the $\vec{a}$-$\vec{b}$ anisotropy had been considered negligible, so it has always been assumed that, for the uniaxial high-temperature superconductors, $\mathbf{m}^*$ has a degenerate eigenvalue m^*_{ab} (*i.e.* $m^*_a \approx m^*_b \equiv m^*_{ab}$) associated with supercurrents flowing in the *ab*-planes that screen magnetic fields perpendicular to the planes, and a nondegenerate eigenvalue m^*_c associated with supercurrents flowing along the c-axis, which help screen magnetic fields parallel to the Cu-O planes [68].

Thus for a uniaxial, anisotropic superconductor:

$$\lambda_{ab} = \sqrt{\frac{m^*_{ab}\, c^2}{4\pi e^2 n_s}} \tag{2.32}$$

and

$$\lambda_c = \sqrt{\frac{m^*_c\, c^2}{4\pi e^2 n_s}} \tag{2.33}$$

One can define an anisotropic ratio γ for uniaxial superconductors, such that:

$$\gamma = \frac{\lambda_c}{\lambda_{ab}} = \sqrt{\frac{m^*_c}{m^*_{ab}}} = \sqrt{\frac{\langle \triangle B^2 \rangle_{\|}}{\langle \triangle B^2 \rangle_{\perp}}} \tag{2.34}$$

For $YBa_2Cu_3O_7$, $\gamma \approx 5$ [69].

2.3.3 Anisotropy of the Energy Gap

In any superconductor with a non-spherical Fermi surface, one expects anisotropy in the superconducting gap function $\Delta(\vec{k})$. In general, the gap function will vary according to the angle with respect to the crystalline axes [70]. That is, the energy required to break a Cooper pair will depend on the direction of $\vec{k}$.

In $YBa_2Cu_3O_7$, one expects the size of the energy gap to show some variation in the *ab*-plane. However this does not necessarily imply nodes in the gap. If the Fermi surface in the *ab*-plane is not a perfect circle, then the gap will certainly be anisotropic; but as is the case for an *anisotropic s-wave* pairing state, the gap may remain finite over the entire Fermi surface. Furthermore, if we are to think of the energy gap in the superconducting state of $YBa_2Cu_3O_{7-\delta}$ as having $d_{x^2-y^2}$ symmetry, $\vec{a}$-$\vec{b}$ anisotropy will produce nodes in the gap which are not precisely along $|\hat{k}_x| = |\hat{k}_y|$.

As mentioned above, conventional superconductors also have some anisotropy in the gap function. However, in most of these materials the mean free path is such that $l \ll \xi$ and also $\lambda \ll \xi$, so that the anisotropy is negligible when interpreting the experimental

results [71]. In the high-T_c superconductors where $\xi \ll l \ll \lambda$, the anisotropy in the gap might play a significant role.

Chapter 3

Measuring the penetration depth with TF-μ^+SR

3.1 The Field Distribution

The vortex lattice in a type-II superconductor results in a spatially varying magnetic field $B(\vec{r})$ inside the superconductor. Transverse -field muon spin rotation (TF-μ^+SR) can be utilized to investigate the local magnetic field distribution function [72,77]:

$$n(B') \equiv \frac{\int \delta[B' - B(\vec{r})] d^3\vec{r}}{\int d^3\vec{r}} \tag{3.1}$$

The function $n(B)$ denotes the field density. Specifically it is the probability that the magnitude of the magnetic field at a point $\vec{r}$ inside the superconductor is B. Eq. (3.1) defines $n(B)$ as the spatial average of a one-dimensional Dirac delta function. By definition

$$\int_{-\infty}^{+\infty} n(B)\, dB = 1 \tag{3.2}$$

The field distribution pertaining to a perfect vortex lattice free of distortions resembles that of Fig. 3.1. The magnetic lineshape exhibits van Hove singularities corresponding to:

A: the minimum value of $B(\vec{r})$ which occurs at the center of the vortex lattice.

B: the saddle point value of $B(\vec{r})$ which occurs midway between two vortices.

C: the maximum value of $B(\vec{r})$ which occurs at the vortex cores.

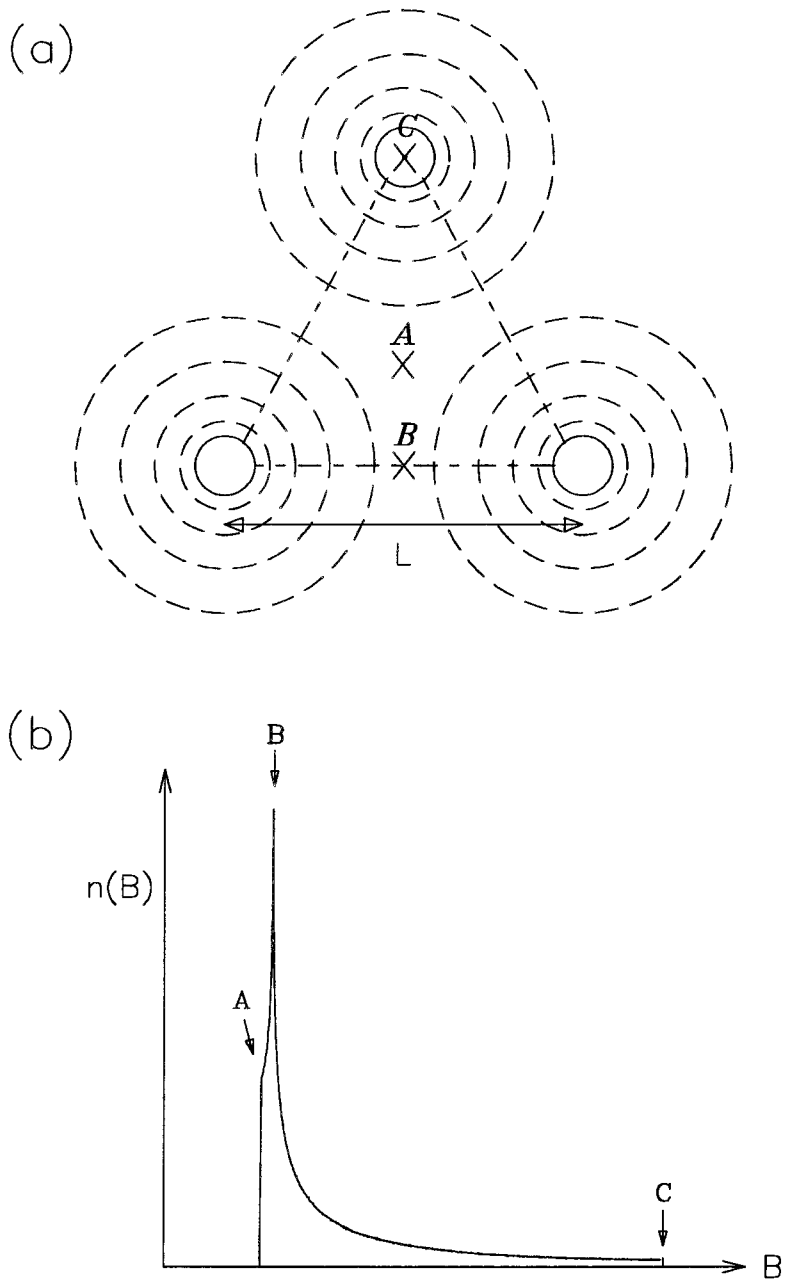

Figure 3.1: (a) A single unit cell in the vortex lattice. The dotted lines represent contours of the local field around a vortex core. The local field is perpendicular to the page. (b) The corresponding field distribution.

The average local magnetic field strength inside the superconductor is denoted $\overline{B}$. The spatial average of B is just the *first moment* of $n(B)$ [73]:

$$\overline{B} \equiv \langle B \rangle = \int_{-\infty}^{+\infty} n(B)\, B\, dB = \mu_o H + (1 - N)M \tag{3.3}$$

where H is the magnitude of the externally applied field, N is the demagnetization factor ($0 \leq N \leq 1$) and M is the magnetization of the sample. The demagnetization factor N depends on the shape of the sample. The *second moment* of $n(B)$ determines the width of the field distribution and is given by:

$$\langle \triangle B^2 \rangle = \langle B^2 \rangle - \langle B \rangle^2 = \int_{-\infty}^{+\infty} n(B) \left(B - \overline{B}\right)^2 dB \tag{3.4}$$

If the applied field $H \lesssim H_{c2}/4$ then the London model is valid. At such fields the spacing L between adjacent vortices is large compared to the coherence length. In the London theory, the local magnetic field in an isotropic superconductor is given as [68]:

$$B(\vec{r}) = \overline{B} \sum_{\vec{K}} \frac{e^{i\vec{K}\cdot\vec{r}}}{1 + \lambda^2 K^2} \tag{3.5}$$

where the sum extends over the reciprocal lattice vectors $\vec{K}$ of the vortex lattice. Combining (3.4) and (3.5), the second moment of $n(B)$ for a triangular flux lattice as determined in the London picture is [32,68]:

$$\langle \triangle B^2 \rangle = 0.00371\, \Phi_o^2\, \lambda^{-4} \tag{3.6}$$

It is clear from Eq. (3.6) that one can estimate the penetration depth λ from the second moment $\langle \triangle B^2 \rangle$, so that λ is inherently related to the line width of the measured field distribution. Eq. (3.6) is valid at intermediate fields $2H_{c1} \leq H < H_{c2}/4$ where the second moment $\langle \triangle B^2 \rangle$ and hence λ is independent of the applied field [34,74]. At such fields the inter-vortex spacing $L \ll \lambda$ [66]. Rammer argues that in the case of $YBa_2Cu_3O_{7-\delta}$, Eq. (3.6) is useful only for fields significantly smaller than 50kG (*i.e.*

5.0T), and above this significant deviations from the London model result rammer. For low fields $H_{c1} \leq H \ll H_{c2}$, where $L \gg \lambda$ and the vortices are well separated, the second moment as determined in the London limit is related to the average local field $\overline{B}$ approximately by [74]:

$$\langle \triangle B^2 \rangle = \overline{B}^2 \left\{ 2\sqrt{3}\pi \left(\lambda\sqrt{3}/2L \right)^2 \left[1 + 4\pi^2 \left(\sqrt{3}\lambda/2L \right)^2 \right] \right\}^{-1} \tag{3.7}$$

This result was derived for a triangular flux-line lattice. According to Eq. (3.7), increasing the applied field in this region leads to a corresponding increase in the second moment. This statement of course assumes that the penetration depth λ is a field independent quantity.

At high fields the second moment decreases with increasing applied field H as the vortex cores start to overlap. The second moment at such fields can be estimated by using Abrikosov's numerical solution of the GL-equations for $H \leq H_{c2}$:

$$\langle \triangle B^2 \rangle \approx C_A \, \Phi_o^2 \, \lambda^{-4} \, [1 - b]^2 \tag{3.8}$$

where $b = \overline{B}/H_{c2}$ and $7.52 \times 10^{-4} < C_A < 8.19 \times 10^{-4}$, with the lower limit given by [34] and the upper limit given by [74]. London theory is not valid in this high-field regime, where the inter-vortex spacing of the lattice is comparable to ξ [*i.e.* $L \leq (5-10)\xi$] and the vortex cores start to overlap [75].

In London theory, where ξ is assumed to be zero, the local magnetic field in the center of a vortex is not finite. To get around this divergence, Brandt [34,72] approximates the vortex core by a gaussian function of width ξ, which provides a dome-shaped peak for the field. An additional term $(1 - b)$ can be incorporated to roughly account for the field dependence of the superconducting order parameter [76]. As in Eq. (3.8) this term is significant for applied fields close to the upper critical field H_{c2}, leading to a noticeable reduction in the width of the magnetic lineshape. Including this effect,

the vortex core can be approximated by a gaussian function of width $\xi/\sqrt{1-b}$. Thus, according to Brandt [34,72,76], one can modify Eq. (3.5) so that the local magnetic field of an isotropic superconductor for applied fields $H < H_{c2}/4$ is

$$B(\vec{r}) = \overline{B} \sum_{\vec{K}} \frac{e^{-i\vec{K}\cdot\vec{r}}\, e^{-\xi^2 K^2/2(1-b)}}{1 + \frac{K^2\lambda^2}{1-b}} \tag{3.9}$$

The second exponential in Eq. (3.9) introduces an upper cutoff for the reciprocal lattice vectors at $K \approx 2\pi/\xi$ [77]. This value emerged from Brandt's numerical solution of the GL-equations [34,72]. The upper cutoff for $\vec{K}$ leads to a finite value of the local field B at the vortex core. Fig. 3.2 illustrates the field distribution $B - \overline{B}$ as determined by Eq. (3.9) for the average internal magnetic fields $\overline{B}$=5kG and 15kG. As the field is increased, the distance between vortex cores decreases. Also the difference between the maximum and minimum field in the distribution decreases with increasing applied field. Fig. 3.3 shows the effects on the field distribution of increasing the magnetic penetration depth λ, while Fig. 3.4 illustrates the dependence on the GL-parameter κ.

The variation of the supercurrent density $\vec{J}_s(\vec{r})$ with position $\vec{r}$ from the vortex centre can be determined by substitution of Eq. (3.9) into Eq. (2.3). Fig. 3.5 illustrates the dependence of the absolute value of the supercurrent density distribution on magnetic field. The supercurrent density is zero at the centre of a vortex core, corresponding to the maximum in the field distribution; J_s rises steeply to its maximum value at the edge of the vortex core and then falls off exponentially. The singularity observed halfway between two vortices denotes a change in the flow direction of the supercurrents.

Fig. 3.8 shows the dependence of the average value of the supercurrent density $\overline{J}_s$ on the average field $\overline{B}$ for $YBa_2Cu_3O_{7-\delta}$. As the applied field ($\approx \overline{B}$) is increased above the lower critical field, the average supercurrent density rises steeply. This is because the supercurrents which screen the vortex cores have less room to spread out at higher fields when the cores are closer together. However, as shown in Fig. 3.8, the relationship

is not linear. This is due to the overlapping of vortices, which tends to reduce $\overline{J}_s$. As the field is increased, the inter-vortex separation decreases. Eventually the overlapping of vortices dominates the contribution to the average supercurrent density and the curve turns over, so that $\overline{J}_s$ decreases with further increase in the applied magnetic field. Interestingly, the turnover in Fig. 3.8 occurs around 50kG; the maximum field at which Rammer claims Eq. (3.6) is valid [32]. The dependence of the supercurrent distribution on λ and κ can be seen in Fig. 3.6 and Fig. 3.7, respectively.

As mentioned in the previous chapter, the orientation of the applied field with respect to the crystallographic axes of the superconductor is important. For an applied field parallel to the c-axis, the second moment of $n(B)$ valid at intermediate fields can be written as [66]

$$\langle \triangle B^2 \rangle_{||} = 0.00371\, \Phi_o^2\, \lambda_{ab}^{-4} \tag{3.10}$$

and for an applied field parallel to the ab-plane,

$$\langle \triangle B^2 \rangle_{\perp} = 0.00371\, \Phi_o^2 (\lambda_{ab}\lambda_c)^{-2} \tag{3.11}$$

In the latter case, the supercurrents flow across the ab-plane and along the c-axis. In fact, for the uniaxial anisotropic high-T_c superconductors, there exists a nonzero component of magnetic field transverse to the vortex axes, when the applied field is not directed along one of the principal axes in the ab-plane or along the c-axis [78]. As the angle between the applied field and the crystallographic c-axis is increased, the vortex lattice distorts. The circular cross-section of an isolated vortex line associated with an applied field directed parallel to the c-axis (see Fig. 3.1) is replaced by an elliptical cross-section as shown in Fig. 3.9. This is a result of the anisotropy of the supercurrents. Correspondingly, the equilateral-triangular vortex lattice is stretched into an isosceles one. The peak in the measured μ^+SR field distribution $n(B)$ will be split because now there are two types of saddle points. However, because the vortices

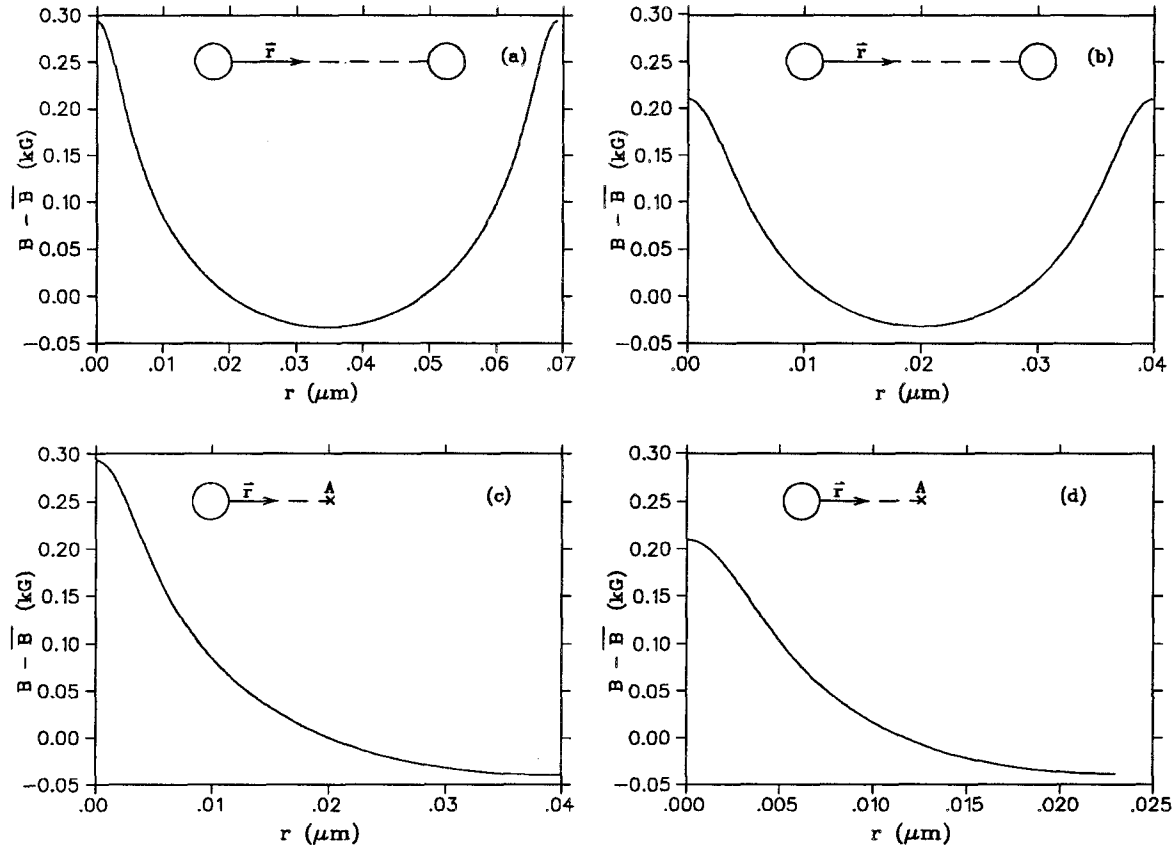

Figure 3.2: The field distribution between the centers of two vortices for (a) $\overline{B}$=5kG and, (b) $\overline{B}$=15kG. The field distribution between the center of a vortice and the center of the flux lattice for (c) $\overline{B}$=5kG and (d) $\overline{B}$=15kG. In all cases $\lambda = 1490$Å and $\kappa = 68$.

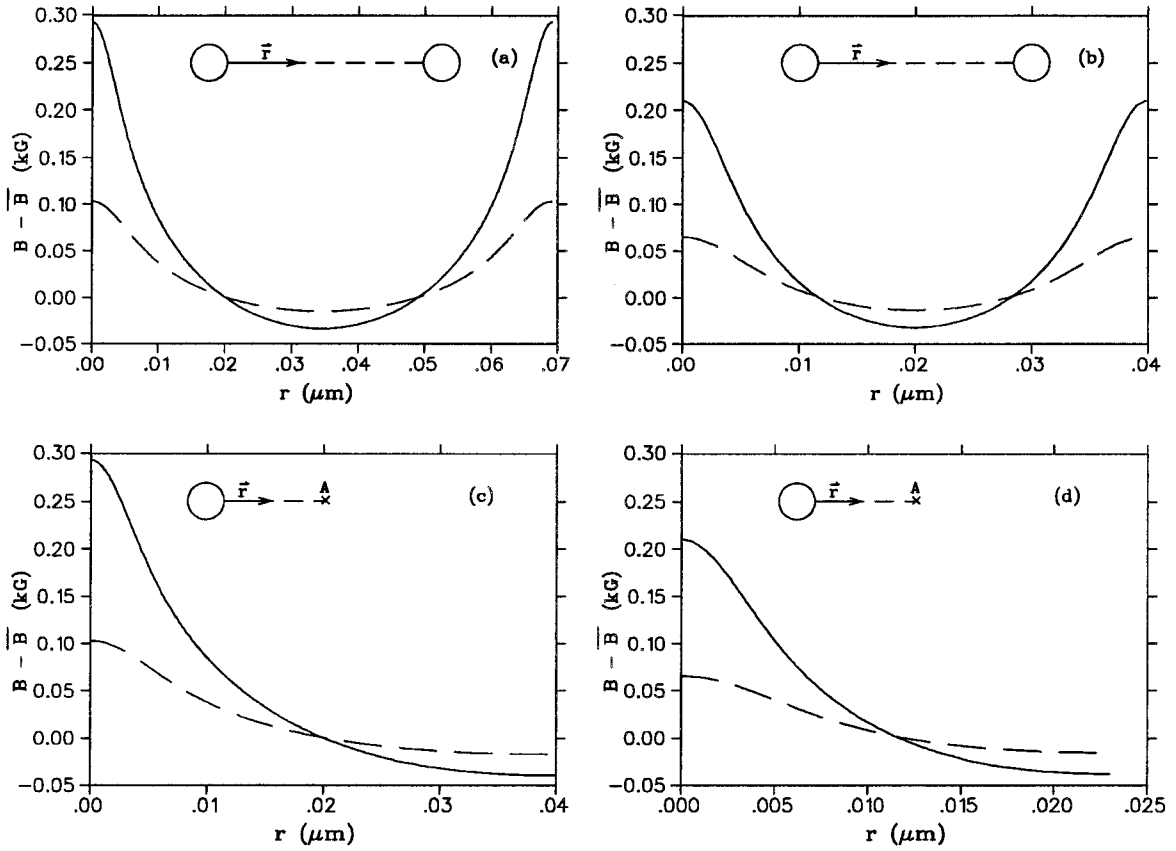

Figure 3.3: The field distribution between the centers of two vortices for (a) $\overline{B}$=5kG and (b) $\overline{B}$=15kG and the field distribution between the center of a vortice and the center of the flux lattice for: (c) $\overline{B}$=5kG and (d) $\overline{B}$=15kG, where λ = 1490Å (solid line) and λ = 2236Å (dashed line). In all cases κ = 68.

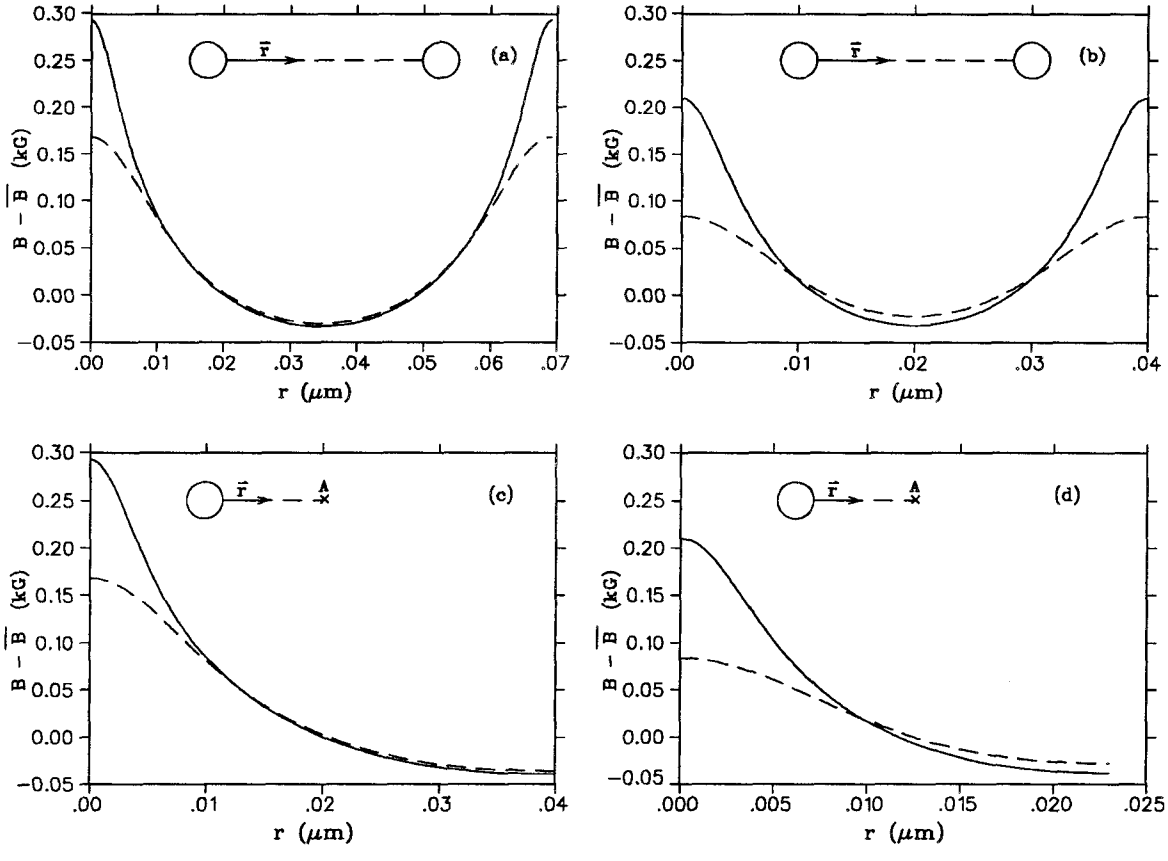

Figure 3.4: The field distribution between the centers of two vortices for (a) $\overline{B}$=5kG and (b) $\overline{B}$=15kG and, the field distribution between the center of a vortice and the center of the flux lattice for (c) $\overline{B}$=5kG and (d) $\overline{B}$=15kG, where $\kappa = 68$ (solid line) and $\kappa = 30$ (dashed line). In all cases $\lambda = 1490$Å.

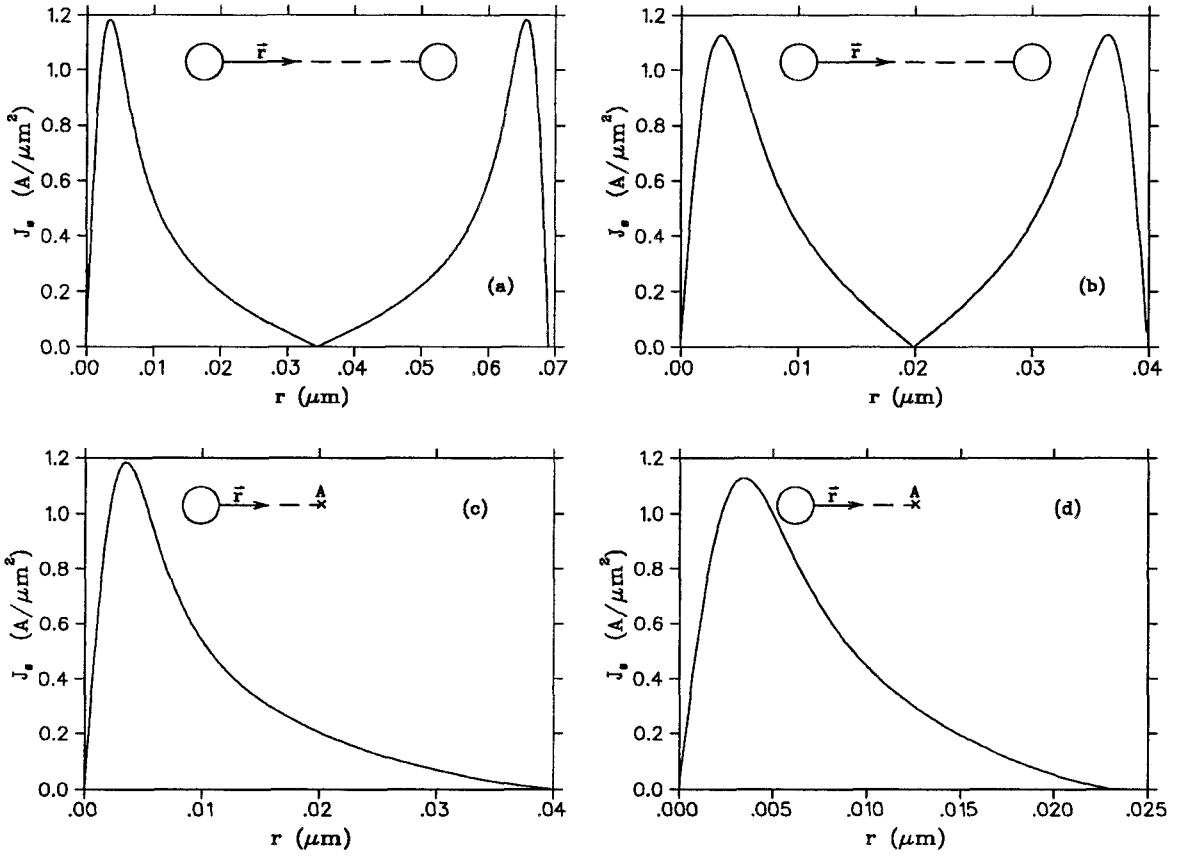

Figure 3.5: The absolute value of the supercurrent distribution between the centers of two vortices for (a) $\overline{B}$=5kG and (b) $\overline{B}$=15kG. The supercurrent distribution between the center of a vortice and the center of the flux lattice for (c) $\overline{B}$=5kG and (d) $\overline{B}$=15kG. In all cases $\lambda = 1490$Å. and $\kappa = 68$.

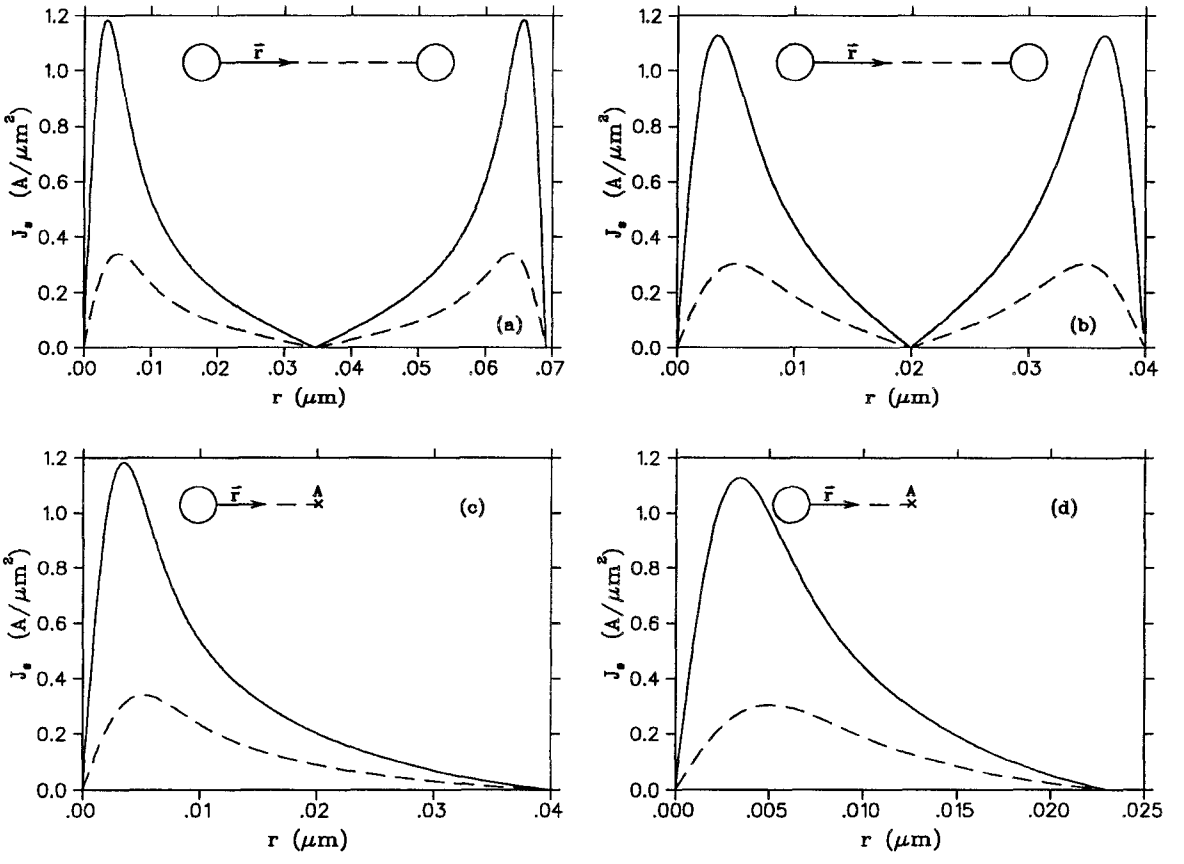

Figure 3.6: The absolute value of the supercurrent distribution between the centers of two vortices for (a) $\overline{B}$=5kG and (b) $\overline{B}$=15kG and the supercurrent distribution between the center of a vortice and the center of the flux lattice for (c) $\overline{B}$=5kG and (d) $\overline{B}$=15kG, where $\lambda = 1490$Å (solid line) and $\lambda = 2236$Å (dashed line). In all cases $\kappa = 68$.

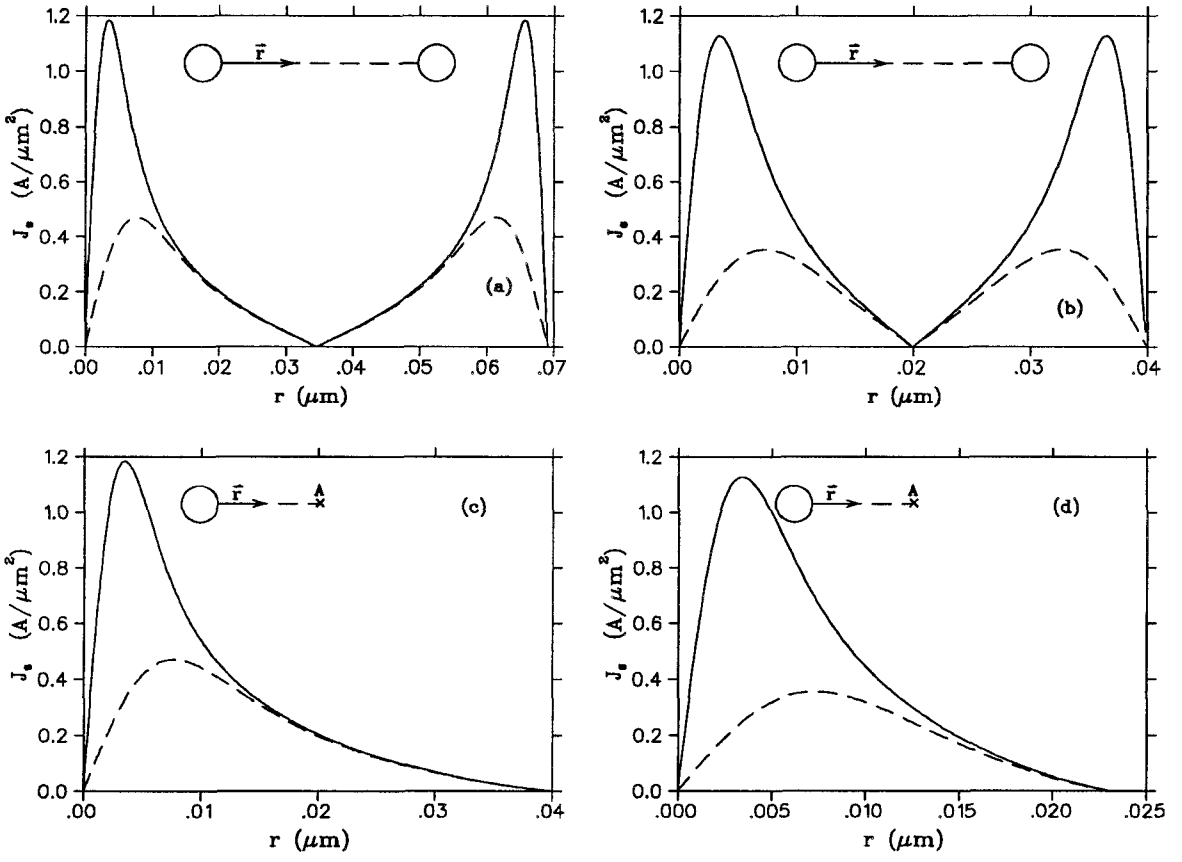

Figure 3.7: The absolute value of the supercurrent distribution between the centers of two vortices for (a) $\overline{B}$=5kG and (b) $\overline{B}$=15kG and, the supercurrent distribution between the center of a vortice and the center of the flux lattice for (c) $\overline{B}$=5kG and (d) $\overline{B}$=15kG, where $\kappa = 68$ (solid line) and $\kappa = 30$ (dashed line). In all cases $\lambda = 1490$Å.

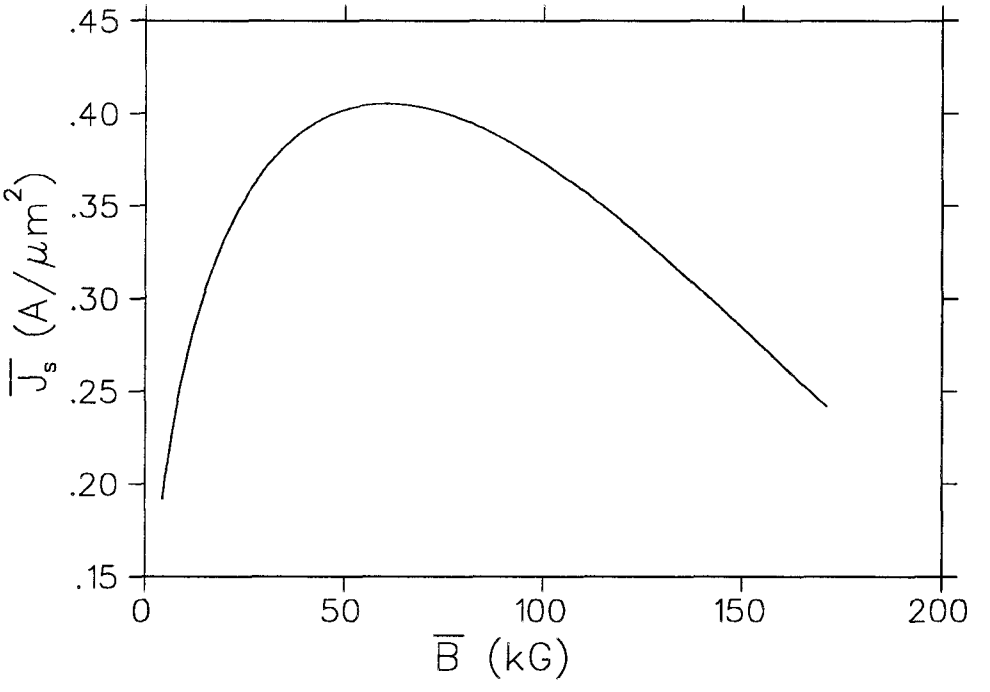

Figure 3.8: The variation of the average supercurrent density $\overline{J}_s$ on the average magnetic field $\overline{B}$ in $YBa_2Cu_3O_{7-\delta}$ with $\lambda = 1490$Å and $\kappa = 68$.

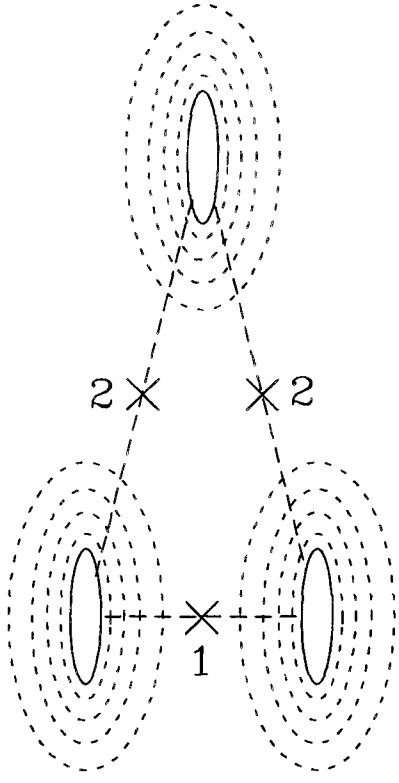

Figure 3.9: The vortex lattice associated with an applied field nonparallel to the crystallographic c-axis. The applied field is perpendicular to the page and the dashed lines are contours of the local magnetic field around the vortex cores; 1 and 2 indicate the two different saddle points in such an arrangement.

themselves are stretched, the saddle points are comparable; so that experimentally, a broadening of the peak in $n(B)$ may be observed, rather than a splitting. The width of the field distribution $n(B)$, as evidenced by Eqs. (3.10) and (3.11), is of course influenced by the anisotropic distortions of the vortex lattice. However it is clear from Eq. (3.10), that by orientating the sample with its crystallographic c-axis parallel to the applied field, the problem becomes isotropic in nature. Of course this is only true if one is ignoring the smaller $\vec{a}$-$\vec{b}$ anisotropy.

3.2 The Role of the Positive Muon

The elegance of the μ^+SR technique is the employment of a positive muon μ^+ to microscopically probe the local magnetic field distribution of Eq. (3.1) in the bulk of the superconducting sample. Thus, measurements of the penetration depth using μ^+SR are less sensitive to the sample's surface than other conventional techniques which measure λ. A positive muon has the following properties [77,79]:

Rest mass: $m_\mu = 105.65839(29)\frac{\text{MeV}}{c^2} = 206.7291(11)m_e = 0.11261(28)m_p$

Charge: +e

Spin: $S_\mu = \frac{1}{2}$

Magnetic Moment: $\mu_\mu = 4.84 \times 10^{-3}\mu_B = 3.18\mu_p$

Average Lifetime: $\tau_\mu = 2.19709(5)\mu$s

Muon Gyromagnetic Ratio: $\gamma_\mu/2\pi = 0.01355342(\pm 0.51\text{ppm})\ \frac{\text{MHz}}{\text{G}}$

Muons are generated via the weak decay of pions:

$$\pi^+ \longrightarrow \mu^+ + \nu_\mu \tag{3.12}$$

A low energy μ^+-beam can be created by making use of the fact that some of the

pions which are produced in collisions of high energy protons with a fixed carbon or beryllium production target stop inside that target. These pions rapidly decay ($\tau_\pi \approx 26$ns) according to Eq. (3.12). Muons produced in this manner are often referred to as *surface muons* to distinguish them from higher momentum muons which are obtained from pions which decay while in flight. A μ^+ emerging from π^+-decay has the direction of its spin antiparallel to its momentum vector. This result follows from conservation of linear and angular momentum, and the fact that the neutrino ν_μ is a left-handed particle (*i.e.* the neutrino helicity $= -1$). A beamline composed of magnetic dipole and quadrupole magnets is used to collect muons emitted in a given direction. Consequently, these muons are nearly 100% spin polarized, with their spin pointing backwards relative to their momentum.

In the TF-μ^+SR arrangement (see Fig. 3.10), the μ^+ spin is rotated perpendicular to the muon momentum using a Wien filter or separator, which consists of mutually perpendicular electric and magnetic fields, both of which are transverse to the beam direction. After passing through a collimator, the spin-polarized positive muons are implanted one by one into the sample, which is situated in an external field H. The applied field is transverse to the initial muon spin polarization, and hence parallel to the muon momentum. The muons entering the sample rapidly thermalize (stop) within $\sim 10^{-13}$s. Their low momentum implies a short range in the sample: $R \sim 120\text{mg/cm}^2$, which corresponds to a thickness of approximately 200μm in $YBa_2Cu_3O_{6.95}$ [77].

Inside the sample, the muon's magnetic moment comes under the influence of the local magnetic field. For $YBa_2Cu_3O_{6.95}$, the local magnetic field $\vec{H}_{local}$ is the vector sum of the externally applied field $\vec{H}_{ext}$, the magnetic field produced by the circulating supercurrents $\vec{H}_s$, and the field $\vec{H}_\mu$ resulting from local magnetic moments:

$$\vec{H}_{local} = \vec{H}_{ext} + \vec{H}_s + \vec{H}_\mu \tag{3.13}$$

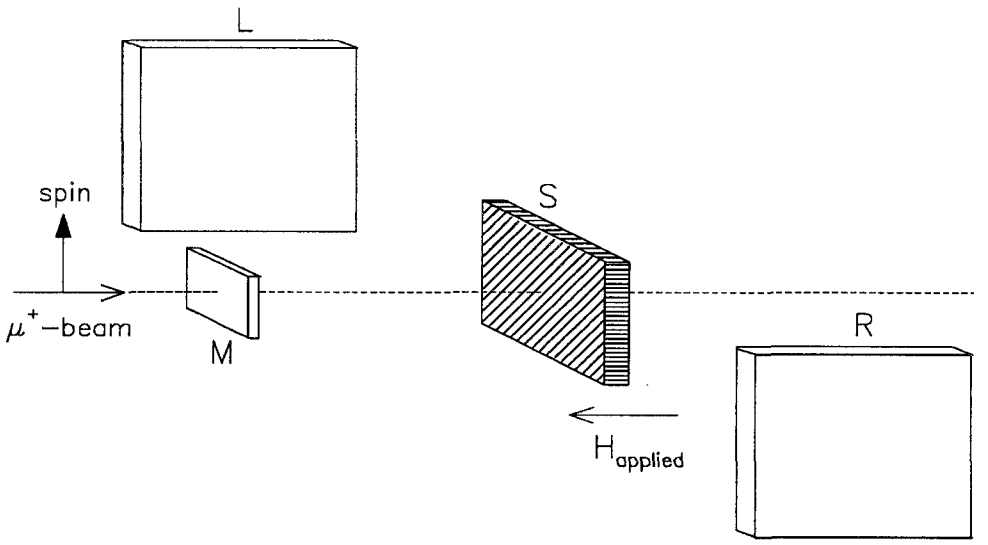

Figure 3.10: Schematic diagram for standard transverse-field geometry. The incoming muon spin is perpendicular to the muon momentum. The muons pass through a thin muon counter M and stop in the sample S, where their spin precesses around the transverse local field. Decay positrons are detected in the L and R counters. The muon spin rotates somewhat in the applied field before reaching the sample.

The muons precess about the local field $\vec{H}_{local}$ with a *Larmor frequency*:

$$\omega_\mu = \gamma_\mu(\mu_o H_{local}) = \gamma_\mu B_{local} \tag{3.14}$$

where B_{local} is the *local magnetic induction* and γ_μ is the *muon gyromagnetic ratio.* If the muons occupy identical sites in the sample, they will be subjected to the same local magnetic field. Therefore they will precess in phase with one another so that the magnitude of their initial polarization is retained. If, however, the muons experience different magnetic fields in the sample, they will not precess at the same Larmor frequency. The resulting dephasing of their spins manifests itself in a corresponding loss of polarization. After a mean lifetime τ_μ, the μ^+ decays into a positron and two neutrinos:

$$\mu^+ \longrightarrow e^+ + \nu_e + \overline{\nu}_\mu \tag{3.15}$$

The distribution of decay positrons is asymmetric with respect to the spin polarization vector $\vec{P}(t)$ of the muon, such that the highest probability of emission is along the direction of the muon spin. Consequently, the time evolution of the muon spin polarization $\vec{P}(t)$ can be monitored, since the μ^+ reveals its spin direction at the time of decay.

A thin μ^+-detector placed in front of the sample registers the arrival of a muon in the sample and starts a clock. A pair of positron detectors (one on either side of the sample as in Fig. 3.10) can be used to detect the positrons emerging from the μ^+-decay. Once a decay positron is registered, the clock is stopped. For a single counter the number of positrons recorded per time bin Δt is

$$N(t) = N^\circ e^{-t/\tau_\mu}\left[1 + A^\circ P(t)\right] + B^\circ \tag{3.16}$$

where N° is a normalization constant, τ_μ is the muon lifetime, A° is the maximum precession amplitude (or maximum experimental decay asymmetry), $P(t)$ is the time

evolution of the muon spin polarization in the direction of the positron counter and B° is a time-independent background from unwanted events.

3.3 The Raw Asymmetry For 2-Counter Geometry

Consider the pair of counters i and j in Fig. 3.11, analogous to counters R and L respectively in Fig. 3.10. In a real experiment one can define the *raw asymmetry* $A_{ij}(t)$ of the appropriately paired histograms $N_i(t)$ and $N_j(t)$ defined by Eq. (3.16) as [77]:

$$A_{ij}(t) = \frac{[N_i(t) - B_i^\circ] - \left[N_j(t) - B_j^\circ\right]}{[N_i(t) - B_i^\circ] + \left[N_j(t) - B_j^\circ\right]} \tag{3.17}$$

where

$$N_i(t) = N_i^\circ e^{-t/\tau_\mu}\left[1 + A_i^\circ\, P_i(t)\right] + B_i^\circ \tag{3.18}$$

$$N_j(t) = N_j^\circ e^{-t/\tau_\mu}\left[1 + A_j^\circ\, P_j(t)\right] + B_j^\circ \tag{3.19}$$

so that

$$A_{ij}(t) = \frac{N_i^\circ\left[1 + A_i^\circ P_i(t)\right] - N_j^\circ\left[1 + A_j^\circ P_j(t)\right]}{N_i^\circ\left[1 + A_i^\circ P_i(t)\right] + N_j^\circ\left[1 + A_j^\circ P_j(t)\right]} \tag{3.20}$$

The motivation behind introducing $A_{ij}(t)$ is the elimination of the muon lifetime (which is a well known quantity) and the random backgrounds B_i° and B_j°. In the ideal situation, the two counters in question are identical to one another so that the μ^+SR histograms recorded by each differ only by an initial phase. Because the muons travel for some time in the applied field before reaching the sample, their initial direction of polarization at the time of arrival in the sample is field dependent. However, the difference in phase between histograms is due solely to the geometry of the positron counters with respect to the sample. This situation is illustrated in Fig. 3.11. In the

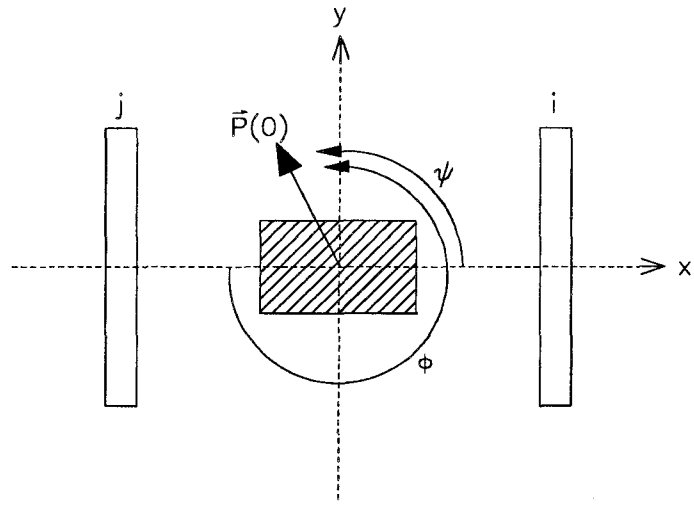

Figure 3.11: The orientation of the initial muon spin polarization $\vec{P}(0)$ with respect to a pair of counters i and j, in a TF-μ^+SR setup. The applied field is out of the page and S denotes the sample.

presence of a constant magnetic flux density B, the time evolution of the muon spin polarization vector $\vec{P}(t)$ is given in general by

$$P(t) = cos(2\pi\nu_\mu + \theta) \tag{3.21}$$

where $\nu_\mu = \frac{\gamma_\mu B}{2\pi}$ is the muon spin precession frequency and θ is the initial phase of the muon spin polarization vector. For counters i and j in Fig. 3.11, the polarization of the muon spin as seen by each counter is:

$$P_i(t) = \cos(2\pi\nu_\mu + \psi) \tag{3.22}$$

$$P_j(t) = \cos(2\pi\nu_\mu + \phi) \tag{3.23}$$

Since $\mid \psi - \phi \mid = 180°$ then,

$$P_i(t) = \cos[2\pi\nu_\mu + (\phi + \pi)] = -\cos(2\pi\nu_\mu + \phi) = -P_j(t) \tag{3.24}$$

With the counters i and j arranged symmetrically along the x and $-x$ directions:

$$P_i(t) \equiv P_x(t) \quad \text{and,} \quad P_j(t) = -P_i(t) \equiv -P_x(t) \tag{3.25}$$

Thus Eq. (3.17) becomes:

$$A_{ij}(t) = \frac{\left(N_i^\circ - N_j^\circ\right) + \left(N_i^\circ A_i^\circ + N_j^\circ A_j^\circ\right) P_x(t)}{\left(N_i^\circ + N_j^\circ\right) + \left(N_i^\circ A_i^\circ - N_j^\circ A_j^\circ\right) P_x(t)} \tag{3.26}$$

If $N_i^\circ = N_j^\circ$ and $A_i^\circ = A_j^\circ \equiv A^\circ$ then Eq. (3.26) reduces to:

$$A_{ij}(t) = A^\circ P_x(t) \tag{3.27}$$

If $B_i^\circ = B_j^\circ$, then using Eqs. (3.17), (3.18), (3.19) and (3.27) the x-component of the polarization can be written as:

$$P_x(t) = \frac{N_i(t) - N_j(t)}{N_i^\circ + N_j^\circ} e^{t/\tau_\mu} \tag{3.28}$$

3.4 The Corrected Asymmetry

In practice, differences in counter efficiency and deviations from perfect geometry complicate the above treatment. If the sensitivity of the individual positron counters are not the same, the values of the normalization constant N°, the maximum decay asymmetry A° and the random background levels B° will differ. The number of recorded events in each counter also depends on the solid angle they subtend at the sample. If the coverage of the solid angle is not maximized because of counter misalignments, there will be a decrease in the number of decay positrons detected. To account for these differences one can modify the above results by assuming:

$$\alpha = \frac{N_j^\circ}{N_i^\circ} \ , \ \beta = \frac{\mid A_j^\circ \mid}{\mid A_i^\circ \mid} \quad \text{and,} \quad \gamma = \frac{B_j^\circ}{B_i^\circ} \tag{3.29}$$

Experimentally one can determine these constants by examining data above T_c where the muon precesses around a spatially constant field. With the above considerations, the raw asymmetry $A_{ij}(t)$ for the counters i and j can then replaced by a *corrected asymmetry* $A_{corrected}(t)$. This is obtained by substituting Eq. (3.29) into Eq. (3.20) and defining $A_i^\circ \equiv A^\circ$ and $P_i(t) \equiv P_x(t)$:

$$A_{corrected}(t) = \frac{(1-\alpha) + A^\circ P_x(t)(1+\alpha\beta)}{(1+\alpha) + A^\circ P_x(t)(1-\alpha\beta)} = \frac{(1-\alpha) + A_{raw}(t)(1+\alpha\beta)}{(1+\alpha) + A_{raw}(t)(1-\alpha\beta)} \tag{3.30}$$

3.5 The Relaxation Function

In the vortex state the muons experience a spatially varying field strength $B(\vec{r})$. Consequently the x-component of the μ^+ polarization may be written:

$$P_x(t) = \frac{1}{N}\sum_{i=1}^{N} \cos\left[\gamma_\mu B(\vec{r_i})t + \theta\right] \tag{3.31}$$

where θ is the initial phase. In a real superconductor there are additional contributions to the relaxation rate, so that a more appropriate description of the μ^+ polarization is:

$$P_x(t) = G_x(t)\frac{1}{N}\sum_{i=1}^{N} \cos\left[\gamma_\mu B(\vec{r_i})t + \theta\right] \tag{3.32}$$

where $G_x(t)$ is a *relaxation function* (or *depolarization function*), which describes the damping of the precession signal. The precise form of the relaxation function $G_x(t)$ depends on the origin of the depolarization. In many cases one assumes a *gaussian* form which is appropriate when the depolarization originates from the muon-nuclear-dipolar interaction [79].

There is no significant loss of polarization during the short time over which the muons thermalize. This is because the primary interactions by which the muons rapidly lose their initial kinetic energy are electrostatic in nature and hence do not affect the muon spin [80]. Loss of the muon spin polarization in the vortex state is primarily due

to the inhomogeneous field distribution, which in turn can be related to the magnetic penetration depth λ. As λ decreases, the spatial variation in the magnetic field becomes greater and there is a corresponding increase in the relaxation rate of the muon spin polarization (see Fig. 3.12). As Fig. 3.1(b) indicates, the field distribution for a perfect vortex lattice is far from being gaussian, but rather is highly asymmetric.

The interaction of the μ^+-spin with nuclear-dipolar fields in the sample leads to further damping of the precession signal and a corresponding broadening of the field distribution. Normally, a gaussian distribution of the dipolar fields at the μ^+-site is assumed. Above T_c, this leads to a Gaussian relaxation function:

$$G_x(t) = e^{-\sigma_d^2 t^2/2} \tag{3.33}$$

where σ_d is the *muon spin depolarization rate* due to the nuclear-dipolar fields. The value of σ_d determined from data taken above T_c, is assumed to be the same in the superconducting state.

For a real sample in the vortex state, decoration experiments have shown that the vortex lattice is not perfect. Deviations from the ideal flux-line lattice lead to a further relaxation of the precession signal [72]. Consequently we can redefine the relaxation function as:

$$G_x(t) = e^{-(\sigma_d^2+\sigma_f^2)t^2/2} = e^{-\sigma_{eff}^2 t^2/2} \tag{3.34}$$

where σ_f is the muon spin depolarization rate due to lattice disorder and any additional depolarizing phenomena and σ_{eff} is the *effective* depolarization rate such that $\sigma_{eff}^2 = \sigma_d^2 + \sigma_f^2$. The influence of σ_{eff} is to further broaden the field distribution $n(B)$ beyond that due to λ.

It should be noted that the additional broadening of the field distribution due to flux-line lattice disorder is difficult to define. Because the field distribution corresponding to an ideal flux-line lattice is highly asymmetric, one would anticipate distortions

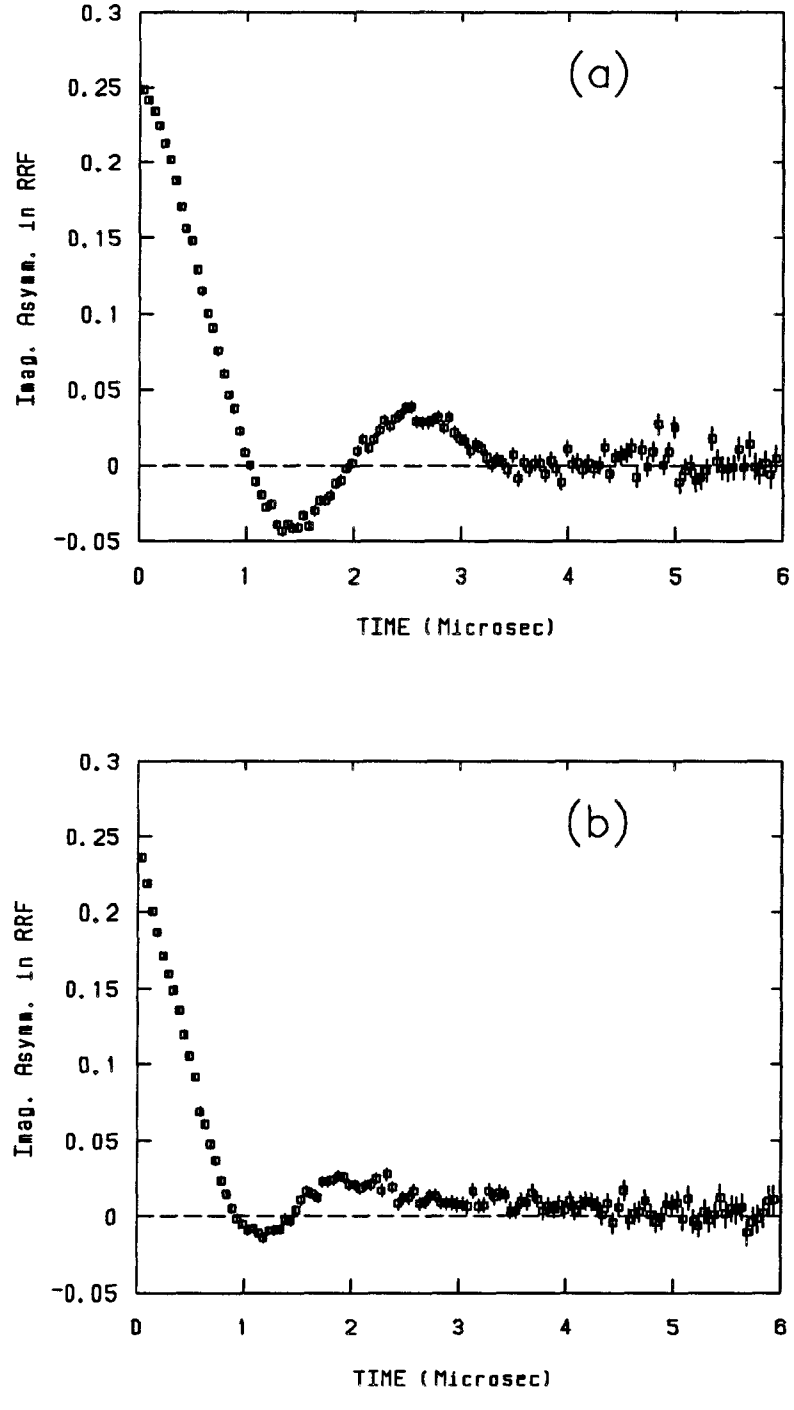

Figure 3.12: Asymmetry spectra plotted in a rotating reference frame due primarily to the vortex lattice in single-crystal $YBa_2Cu_3O_{6.95}$. The data is for an applied transverse field of 15kG at the temperatures (a) T=75K where $\lambda \approx 2040$Å and (b) T=2.9K where $\lambda \approx 1526$Å.

of the lattice to also be asymmetric in nature. In Eq. (3.34) we are assuming the distortions are gaussian distributed, but it can be shown analytically that convoluting with a gaussian does not change the average field of the distribution.

3.6 Modelling The Asymmetry Spectrum of the Vortex State

In terms of λ, the experimental raw asymmetry for TF-μ^+SR analysis of the vortex state in an isotropic type-II superconductor can be modelled assuming that the contribution to $A(t)$ from a particular point in the flux lattice is

$$A_{raw}^{th}(t) = \frac{A^\circ}{N}\sum_{i=1}^{N}\cos\left\{\left[\gamma_\mu \overline{B}t\sum_{\vec{K}}\frac{e^{-i\vec{K}\cdot\vec{r}_i}e^{-\lambda^2K^2/[2\kappa^2(1-b)]}}{1+\frac{K^2\lambda^2}{(1-b)}}\right]+\theta\right\} \tag{3.35}$$

where I have combined Eqs. (3.9), (3.27) and (3.31). Eq. (3.35) applies to an ideal flux lattice. To account for smearing of the field distribution due to flux-lattice disorder and nuclear dipolar fields, Eq. (3.35) must be convoluted with a gaussian distribution in the form of Eq. (3.34):

$$A_{raw}^{th}(t) = \frac{A^\circ}{N}e^{-\sigma_{eff}^2t^2/2}\sum_{i=1}^{N}\cos\left\{\left[\gamma_\mu \overline{B}t\sum_{\vec{K}}\frac{e^{-i\vec{K}\cdot\vec{r}_i}e^{-\lambda^2K^2/[2\kappa^2(1-b)]}}{1+\frac{K^2\lambda^2}{(1-b)}}\right]+\theta\right\} \tag{3.36}$$

Assuming that the flux-line lattice is composed of equilateral triangles as depicted in Fig. 3.1(a), an arbitrary reciprocal-lattice vector $\vec{K} = n\vec{k}_1 + m\vec{k}_2$ can be written in terms of the real lattice vectors $\vec{r}_1 = L\hat{x}$ and $\vec{r}_2 = L/2(\hat{x}+\sqrt{3}\hat{y})$ so that

$$\vec{K} = \frac{2\pi}{L}\left[n\hat{x}+\frac{1}{\sqrt{3}}(2m-n)\hat{y}\right] \tag{3.37}$$

where

$$L = \sqrt{\frac{2\,\Phi_\circ}{\sqrt{3}\,\overline{B}}} \tag{3.38}$$

is the distance between adjacent vortices. Combining Eqs. (3.36) and (3.37) gives

$$A^{th}_{raw}(t) = \frac{A^{\circ}}{N_1 N_2} e^{\frac{-\sigma^2_{eff} t^2}{2}} \sum_{i=0}^{N_1} \sum_{j=0}^{N_2}$$

$$\times \cos\left\{\left[\gamma_\mu \overline{B} t \sum_{n,m} \frac{\cos\left\{\frac{2\pi}{L}\left[a_i n + a_j\left(\frac{2m-n}{\sqrt{3}}\right)\right]\right\} e^{\frac{-\lambda^2}{\kappa^2}\left(\frac{4\pi}{\sqrt{3}L}\right)^2 \frac{(n^2+m^2-mn)}{2(1-b)}}}{1 + \frac{\left(\frac{4\pi}{\sqrt{3}L}\right)^2 (n^2+m^2-mn)\lambda^2}{(1-b)}}\right] + \theta\right\} \tag{3.39}$$

where $\vec{r}_{ij} = a_i\hat{x} + a_j\hat{y}$ is a vector in real space and the sum over a_i and a_j extends over a single unit cell. Eq. (3.39) can be substituted into Eq. (3.30) and the resulting theoretical corrected asymmetry used to fit the measured asymmetry.

3.7 4-Counter Geometry and the Complex Polarization

In the 2-counter setup of Fig. 3.11, information is lost by failing to detect decay positrons emitted in the *up* and *down* directions. A more efficient setup is the 4-counter arrangement depicted in Fig. 3.13, where additional counters are placed on the y and $-y$ axes. The **L** and **R** counters monitor the x-component of the polarization $P_x(t)$ as before, while the **U** and **D** counters measure the y-component of the polarization $P_y(t)$. Ignoring geometric misalignments and differences in counter efficiency, $P_y(t)$ differs from $P_x(t)$ only by a phase of 90°. In terms of the field distribution $n(B)$, $P_x(t)$ and $P_y(t)$ are defined as:

$$P_x(t) = e^{-\sigma^2_{eff} t^2/2} \int_{-\infty}^{+\infty} n(B) \cos\left[\gamma_\mu B t + \theta\right] dB \tag{3.40}$$

$$\begin{aligned} P_y(t) &= e^{-\sigma^2_{eff} t^2/2} \int_{-\infty}^{+\infty} n(B) \cos\left[\gamma_\mu B t + \theta - \pi/2\right] dB \\ &= e^{-\sigma^2_{eff} t^2/2} \int_{-\infty}^{+\infty} n(B) \sin\left[\gamma_\mu B t + \theta\right] dB \end{aligned} \tag{3.41}$$

where, $G_x(t) = G_y(t) = e^{-\sigma^2_{eff} t^2/2}$. For an applied field in the $\vec{z}$-direction, the muon spin polarization transverse to the magnetic field B_z may be described by the complex

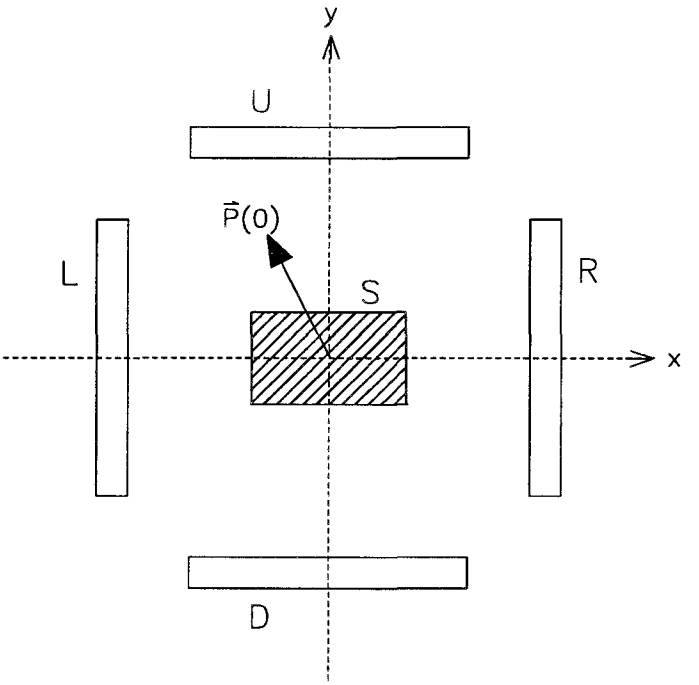

Figure 3.13: The orientation of the initial muon spin polarization $\vec{P}(0)$ with respect to a set of four counters **L**, **R**, **U** and **D**, in a TF-μ^+SR setup. The applied field is out of the page and **S** denotes the sample.

quantity [81]

$$\begin{aligned} P^+(t) &= P_x(t) + i\,P_y(t) \\ &\equiv e^{-\sigma_{eff}^2 t^2/2} \int_{-\infty}^{+\infty} n(B_z) e^{i(\gamma_\mu B_z t + \theta)} dB_z \end{aligned} \tag{3.42}$$

The real Fourier transform of the *complex muon polarization* $P^+(t)$ approximates the field distribution $n(B_z)$ with statistical noise due to finite counting rates [34]. At the later times in the asymmetry spectrum, most of the muons have already decayed. With few muons left, the statistics at these later times are low, resulting in increased noise at the end of the asymmetry spectrum. Using the fact that $P^+(t)$ is defined only

for positive times $t \geq 0$, the field distribution $n(B_z)$ may be written:

$$n(B_z) \simeq 2Re\left\{\frac{\gamma_\mu}{2\pi}\int_0^\infty P^+(t)e^{-\sigma_A^2 t^2/2}e^{\left(-i\gamma_\mu B_z t-\sigma_{eff}^2 t^2/2\right)}dt\right\} \tag{3.43}$$

where the gaussian *apodization parameter* σ_A is chosen to provide a compromise between statistical noise in the spectrum and additional broadening of the spectrum which such a procedure introduces.

The *complex asymmetry* for the 4-counter setup is defined as:

$$\begin{aligned} A^+(t) &= A^\circ P^+(t) \\ &= A^\circ P_x(t) + i\, A^\circ P_y(t) \\ &= A_x(t) + i\, A_y(t) \end{aligned} \tag{3.44}$$

where $A_x(t)$ and $A_y(t)$ are the *real* and *imaginary* parts of the complex asymmetry, respectively. The number of counts per second in the i^{th} counter [i = **R** (right), **L** (left), **U** (up) or **D** (down)], may be written:

$$N_i(t) = N_i^\circ e^{-t/\tau_\mu}\left[1 + A_i(t)\right] + B_i \tag{3.45}$$

where $A_i(t) = A_i^\circ P_i(t)$ is the asymmetry function for the i^{th} raw histogram. Rearranging Eq. (3.45):

$$A_i(t) = e^{t/\tau_\mu}\left[\frac{N_i(t) - B_i}{N_i^\circ}\right] - 1 \tag{3.46}$$

In terms of the individual counters depicted in Fig. 3.13, the real asymmetry $A_x(t)$ and the imaginary asymmetry $A_y(t)$ may be written:

$$A_x(t) = \frac{1}{2}\left[A_R(t) - A_L(t)\right] \tag{3.47}$$

$$A_y(t) = \frac{1}{2}\left[A_U(t) - A_D(t)\right] \tag{3.48}$$

In the present study, the real and imaginary parts of the asymmetry are fit simultaneously. For the vortex state of $YBa_2Cu_3O_{6.95}$, the real asymmetry can be fit with Eq.

(3.39). The imaginary part of the asymmetry can be fit with the same function, but with a phase difference of 90°.

3.8 The Rotating Reference Frame

It is often convenient to fit the measured asymmetry in a *rotating reference frame* (RRF). To do this, one subtracts a phase $\phi_{RRF} = \omega_{RRF}t$ from the phase of Eq. (3.39), where $\omega_{RRF} = 2\pi\nu_{RRF}$ is the chosen RRF frequency. The RRF frequency is taken to be slightly lower than the average Larmor-precession frequency $\overline{\omega}_\mu$ of the muon. The precession signal viewed in this rotating reference frame has only low frequency components on the order of $\overline{\omega}_\mu - \omega_{RRF}$, where $\overline{\omega}_\mu$ is the average precession frequency in the lab frame. This has two important consequences. The first is that the quality of the fit can be visually inspected. Second and most important, it allows the data to be packed into much fewer bins, greatly enhancing the speed of fitting.

Chapter 4

Experimental Determination of $\lambda_{ab}(T)$

4.1 Sample Characteristics

A mosaic of three twinned single crystals of $YBa_2Cu_3O_{6.95}$ were utilized in this experiment. The $YBa_2Cu_3O_{6.95}$ crystals were of extremely high quality, as characterized by low-field magnetization, *ab*-plane resistivity, microwave surface resistance and heat capacity measurements [85]. For example, the superconducting transition temperature T_c, determined by magnetization measurements was found to be 93.2K with a relatively narrow transition width $\Delta T_c < 0.25$K.

The $YBa_2Cu_3O_{6.95}$ single crystals were grown by a flux method in yttria-stabilized zirconia crucibles. CuO-BaO flux was poured over hot (950-970°C) crystals initially grown from high purity Y_2O_3 (99.999%), CuO (99.999%) and $BaCO_3$ (99.997%) compounds. To ensure each crystal had the identical oxygen concentration corresponding to the maximum T_c, all three crystals were carefully annealed prior to the experiment. For 3 days the crystals were held in 1 atmosphere of O_2 at 860°C, followed by 14 days at 450°C before rapidly cooling to room temperature. Together the three crystals had a total mass of 53mg.

4.2 The Apparatus

The measurements were performed on the M15 surface μ^+ beamline at TRIUMF. The beam consisted of low momentum (28.6MeV/c), 100% backward spin polarized positive

muons. The short range of these muons makes this beamline ideal for the study of thin samples. A crossed-field separator was used to rotate the muon spins perpendicular to their momentum direction. After passing through a 1cm diameter collimator and a thin muon defining counter, a small fraction of the incoming beam came to rest in the crystals ($30,000\mu^+s^{-1}$ stops out of $200,000\mu^+s^{-1}$ incoming).

Great effort was devoted to reducing the background signal in this experiment, which superimposes itself on the measured field distribution originating from the sample. The background signal originates from muons stopping in the sample holder or in the cryostat walls and windows, which then precess in the externally applied field. Previous μ^+SR experiments on single crystals have been seriously plagued by the inseparable nature of the often large background signal [77]. A novel experimental setup was used to eliminate most of the background signal produced by those muons which missed the sample [86]. The three crystals were mounted on a thin layer of aluminized mylar using a minute portion of *Apiezon N* grease, with their c-axes parallel to the applied field. Recall with this orientation of the field it is $\lambda_{ab}(T)$ which is measured. The thin aluminized mylar provides no appreciable signal. The three crystals together provided a total area of $36mm^2$ for the incoming muon beam. Data taken with only one of the three single crystals of $YBa_2Cu_3O_{6.95}$, showed no further appreciable reduction in the background signal and gave the same foreground signal as the 3-crystal sample. Consequently, a mosaic consisting of all three single crystals was used to maximize the counting rates for muons striking the sample.

The mylar with the mosaic of crystals was stretched over the end of a hollow 4.45cm-diameter, cylindrical, aluminum sample holder, as indicated in Fig. 4.1. A horizontal ^{4}He gas-flow cryostat with an internal diameter of 4.92cm, allowed cooling of the crystalline $YBa_2Cu_3O_{6.95}$ down to $\sim$ 2.6K. A 7T warm-bore superconducting magnet called

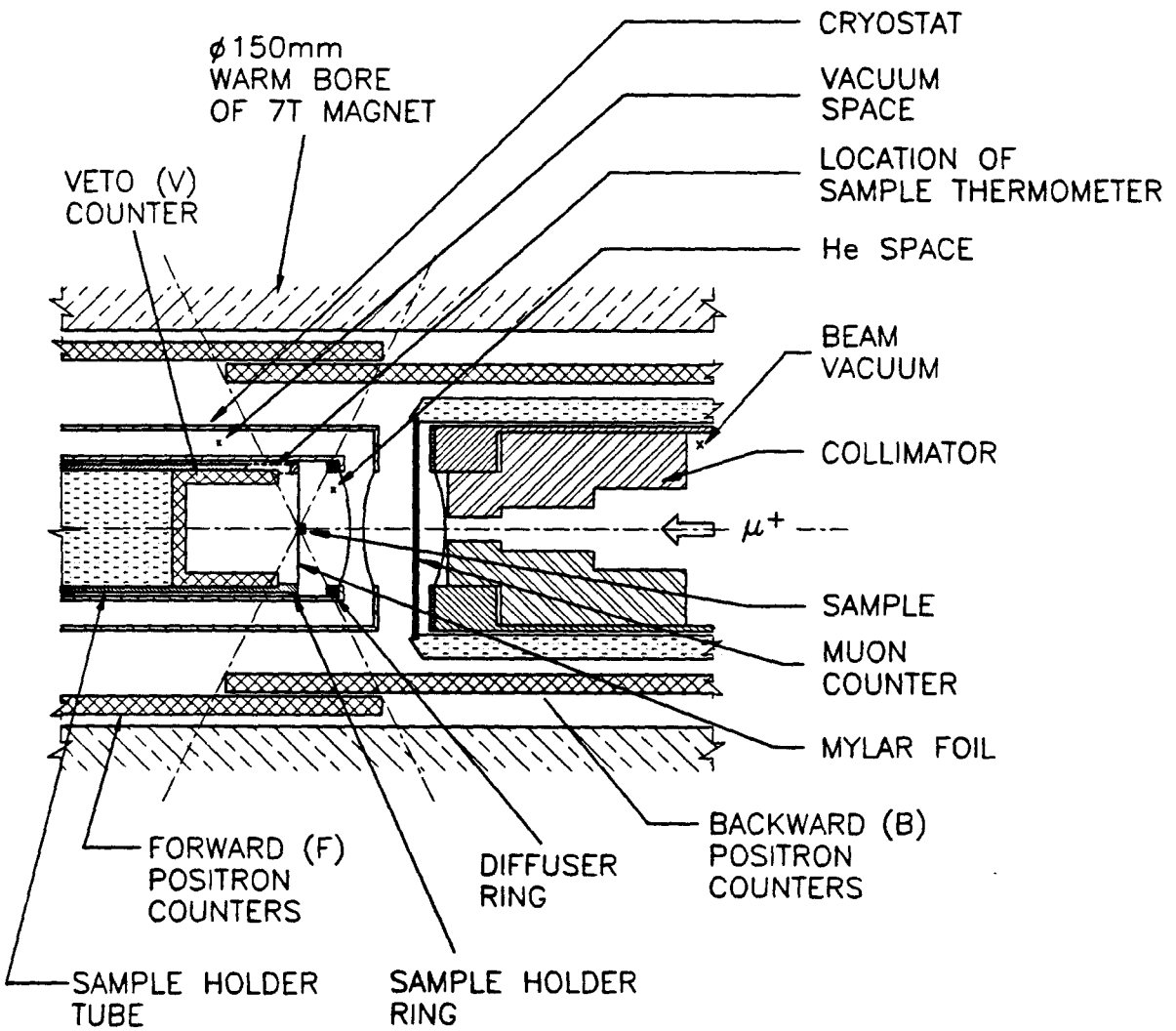

Figure 4.1: The low background μ^+SR apparatus.

Helios was used to produce magnetic fields transverse to the initial muon spin direction.

The positrons emitted from the muon decay were readily detected by a cylindrical arrangement of positron counters, coaxial with the magnet axis. Overlapping forward (F) and backward (B) counters were used to define a solid angle for muon decay events originating from the sample. A *veto* (V) counter in the form of a cylindrical scintillator cup, was employed to discriminate against those muons which missed the sample. A "good" muon stop was defined as $M \cdot \bar{V}$ ($M \equiv$ muon counter). A "good" positron stop (*i.e.* a positron originating from a muon that stopped in the sample) was defined as $F \cdot B \cdot \bar{V}$.

4.3 The Measured Asymmetry

Transverse-field μ^+SR spectra with approximately 2×10^7 muon decay events were taken under conditions of field cooling in applied magnetic fields of 0.5T and 1.5T. Figure 4.2(a) and Fig. 4.2(b) show the real and imaginary asymmetry spectra pertaining to the $YBa_2Cu_3O_{6.95}$ sample resting in an applied field of 0.5T and at a temperature well above T_c (*i.e.* $T \approx 110$K). For convenience the signals are displayed in a reference frame rotating at a frequency 2.3MHz below the Larmor precession frequency of a free muon. The average frequency of oscillation in Fig. 4.2(a) and Fig. 4.2(b) is determined by the applied magnetic field of 0.5T. Consequently, the corresponding frequency distribution [see Fig. 4.2(c)] exhibits a single peak at 67.3MHz related to the applied field through Eq. (3.14). Visual inspection of Fig. 4.2(a) and Fig. 4.2(b) suggests that the real and imaginary asymmetry spectra differ in phase by 90°, consistent with the discussion in the previous chapter. The solid curve passing through the data points is a fit to the data using a polarization function in the form of Eq. (3.21) with a relaxation function

resembling Eq. (3.33), so that

$$A(t) = A^{\circ}P(t) = A^{\circ}_{ns}e^{-\sigma^2_{ns}t^2/2}cos\left(2\pi\nu_{\mu}t + \theta\right) \tag{4.1}$$

where A°_{ns} (ns $\equiv$ normal state) is the precession amplitude, σ_{ns} is the depolarization rate due to nuclear dipolar broadening and ν_{μ} is the average precession frequency of a muon about the applied magnetic field. The real and imaginary parts of the measured asymmetry were fit simultaneously. The relaxation of the muon spin precession signal is small and is owing primarily to the distribution of the nuclear-dipolar fields in the sample. In particular, $\sigma_{ns} \approx 0.13\mu s^{-1}$ in Fig. 4.2.

As one cools the sample below T_c, the relaxation rate of the muon precession signal increases due to the presence of the vortex lattice. The asymmetry spectra pertaining to a pair of counters for the $YBa_2Cu_3O_{6.95}$ crystals in an applied field of 0.5T is shown for three different temperatures below T_c in Fig. 4.3. The signals are shown in a rotating reference frame 3.3MHz below the Larmor precession frequency of a free muon. As the muons stop randomly on the length scale of the flux lattice, the muon spin precession signal provides a random sampling of the internal field distribution in the vortex state. The ensuing asymmetry spectrum is a superposition of a signal resembling Fig. 3.12 originating from muons which stop in the sample and an inseparable background signal resembling Fig. 4.2(c), due to muons which miss the sample, do not trigger the veto counter and whose positron also does not trigger the veto counter. The origin of the residual background signal is still uncertain, but may be due to those muons which scatter at wide angles after passing through the muon counter and are thus not vetoed by the V counter. Fig. 3.12 was obtained by choosing a rotating reference frame frequency equal to the background frequency, determined by fitting the data. Unfortunately, the broadening of the background signal is not necessarily identical to the field distribution above T_c and thus cannot be fixed in the fits below T_c.

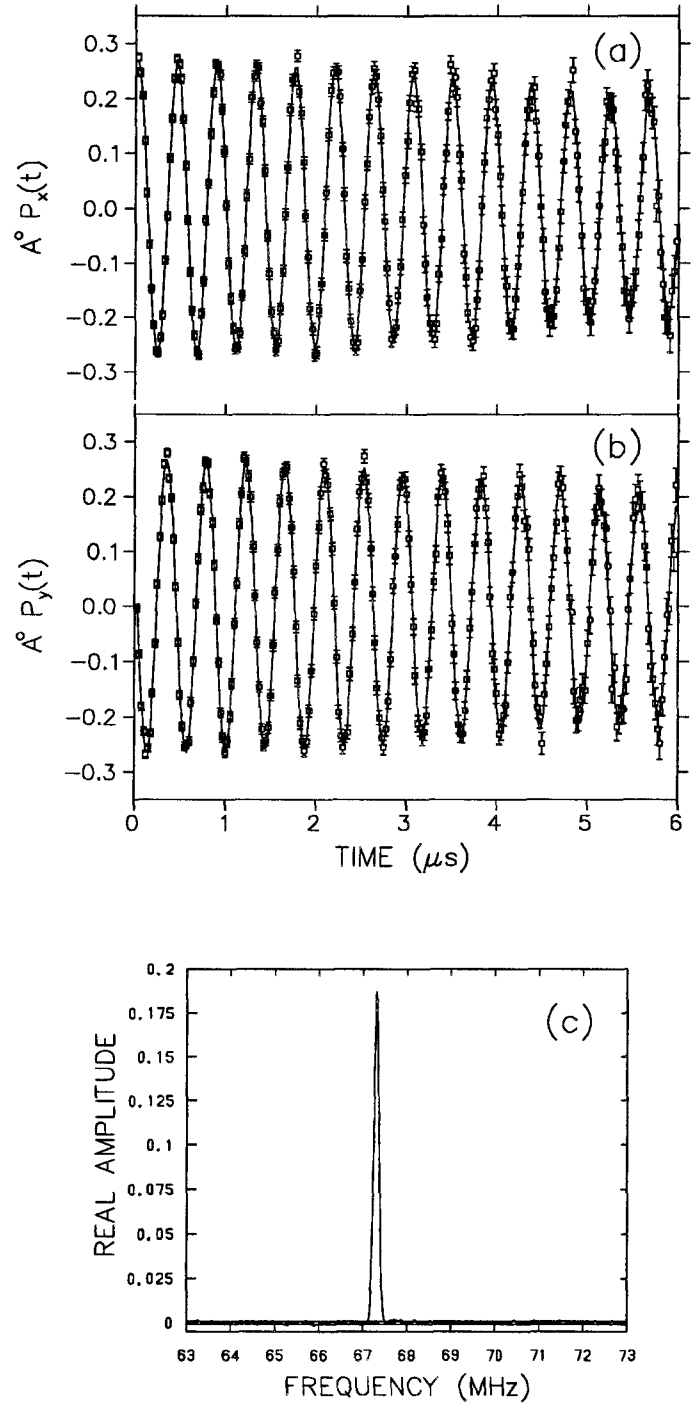

Figure 4.2: (a) The real part and, (b) the imaginary part of the muon precession signal in $YBa_2Cu_3O_{6.95}$ at 110K in a magnetic field of 0.5T. The solid curves are a fit to the data assuming a gaussian distribution of fields [see Eq. (4.1)]. (c) The corresponding frequency distribution. The peak is at 67.31MHz, corresponding to an average field of 0.497T.

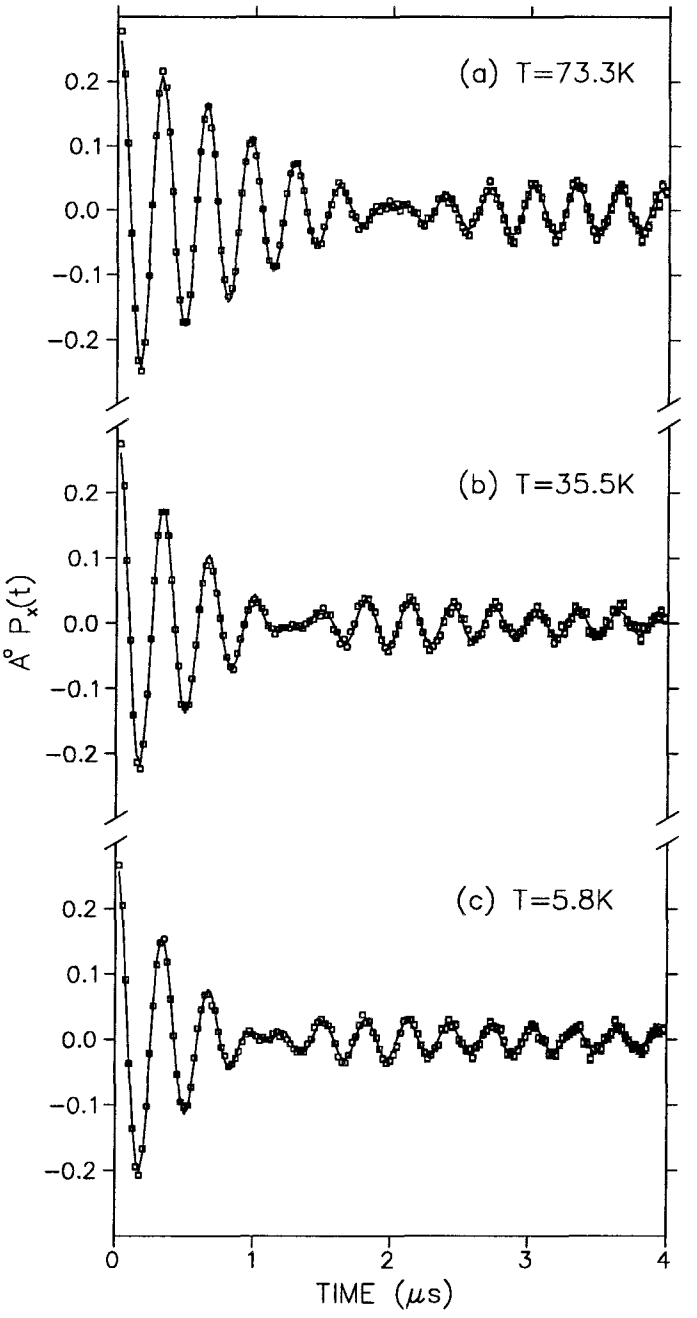

Figure 4.3: The muon precession signal for $YBa_2Cu_3O_{6.95}$ in a field of 0.5T and at, (a) 73.3K, (b) 35.5K and (c) 5.8K. The solid curves are a fit to the data assuming the field distribution of Eq. (2.10).

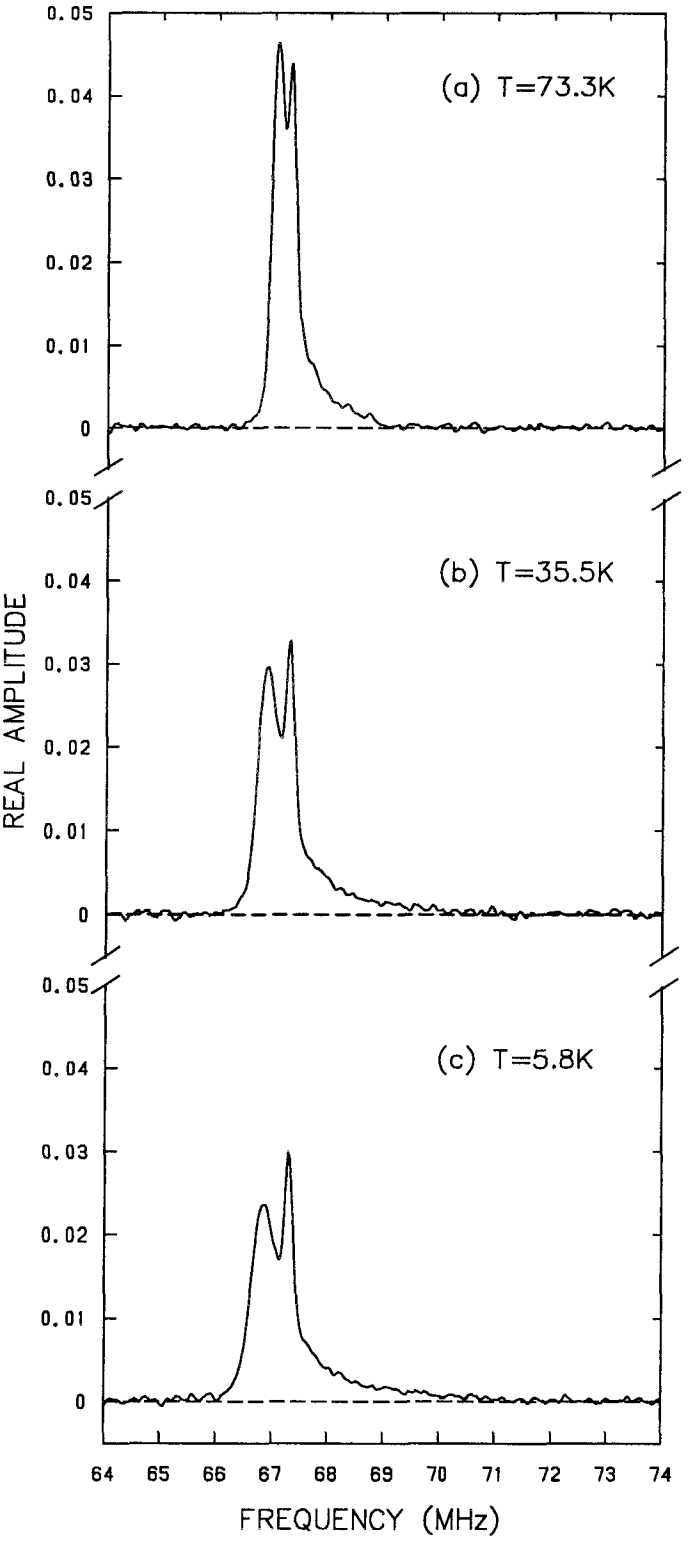

Figure 4.4: The corresponding Fourier transforms of Fig. 4.3 for $YBa_2Cu_3O_{6.95}$ in a field of 0.5T and at, (a) 73.3K, (b) 35.5K and (c) 5.8K.

The beat occurring in all three spectra of Fig. 4.3 is due to the difference in the average precession frequency of a muon in the internal field of the vortex lattice and the precession frequency of the muon in the background field. The solid curves in Fig. 4.3 are fits to the theoretical polarization function of Eq. (3.39). An additional polarization function in the form of Eq. (4.1) was added to model the background signal pertaining to the muons which missed the sample, so that the measured asymmetry is of the form:

$$A(t) = A_{sam}(t) + A_{bkg}(t) \tag{4.2}$$

where $A_{sam}(t)$ (sam $\equiv$ sample) is as given in Eq. (3.39) and the background asymmetry $A_{bkg}(t)$ (bkg $\equiv$ background) has the form:

$$A_{bkg}(t) = A^{\circ}_{bkg} e^{-\sigma^2_{bkg} t^2/2} \cos\left(\gamma_\mu \overline{B}_{bkg}\, t + \theta\right) \tag{4.3}$$

As the temperature is lowered, the vortices become better separated and the muon spin relaxes faster due to the presence of a broader distribution of internal magnetic fields. This is better displayed in Fig. 4.4 which shows the corresponding real Fourier transforms of Fig. 4.3. Recall from Eq. (3.6) that the width of the field distribution is proportional to $1/\lambda^2_{ab}(T)$. Thus it is clear from Fig. 4.4 that $\lambda_{ab}(T)$ decreases with decreasing temperature. The sharp spike on the right side of each frequency distribution in Fig. 4.4 is attributed to the residual background signal. It has been determined to account for approximately 13% of the total signal amplitude at 0.5T and $\sim$ 5% at 1.5T.

Figure 4.5 shows the frequency distribution resulting from field cooling the sample in the 0.5T field [Fig. 4.5(a)] and then lowering the applied field by 11.3mT [Fig. 4.5(b)]. As shown the background signal shifts down by 1.5MHz and positions itself at the Larmor frequency corresponding to the new applied field. The signal originating from muons which stop in the sample does not appear to change under this small shift in field. This clearly demonstrates that at low temperatures the vortex lattice is strongly

pinned. Furthermore, the absence of any background peak in the unshifted signal implies that the sample is free of any appreciable non-superconducting inclusions. The shifting of the background peak away from the sample signal has since been duplicated for higher temperatures and at other applied fields. Field shifts in excess of $\sim$ 200G were not attempted for fear that the crystals would shatter as a result of the strain exerted by the pinned vortex lattice.

The asymmetric frequency distribution shown isolated in Fig. 4.5(b) has the basic features one would anticipate for a triangular vortex lattice, but with the van Hove singularities shown in Fig. 3.1(b) smeared out. Structural defects in the vortex lattice, variations in the average field due to demagnetization effects and $\vec{a}$-$\vec{b}$ anisotropy are all possible reasons for a lack of sharper features.

4.4 Data Analysis

To determine the low temperature behaviour of $\lambda_{ab}(T)$ several assumptions were made in the fitting procedure to reduce the number of independent variables. To start with, the Ginzburg-Landau parameter $\kappa = \lambda_{ab}/\xi$ was assumed to be independent of temperature. Although this is strictly valid only for weak coupling s-wave superconductors away from T_c, the lineshapes are not very sensitive to κ in the low-field region being considered here. Determining a value for κ was accomplished by first fitting the recorded asymmetry spectra with κ as a fixed quantity. The value of κ which minimized the sum of the χ^2's for each temperature considered was then taken to be the best value for κ. The value $\kappa = 68$ gave the best overall fit to both the 0.5T and 1.5T data. Increasing κ to 73 was found to change $\lambda_{ab}(0)$ by less than 0.3nm. The value $\kappa = 68$ is close to the value $\kappa = 69(1.4)$ determined from previous lineshape measurements on similar crystals in higher magnetic fields [77].

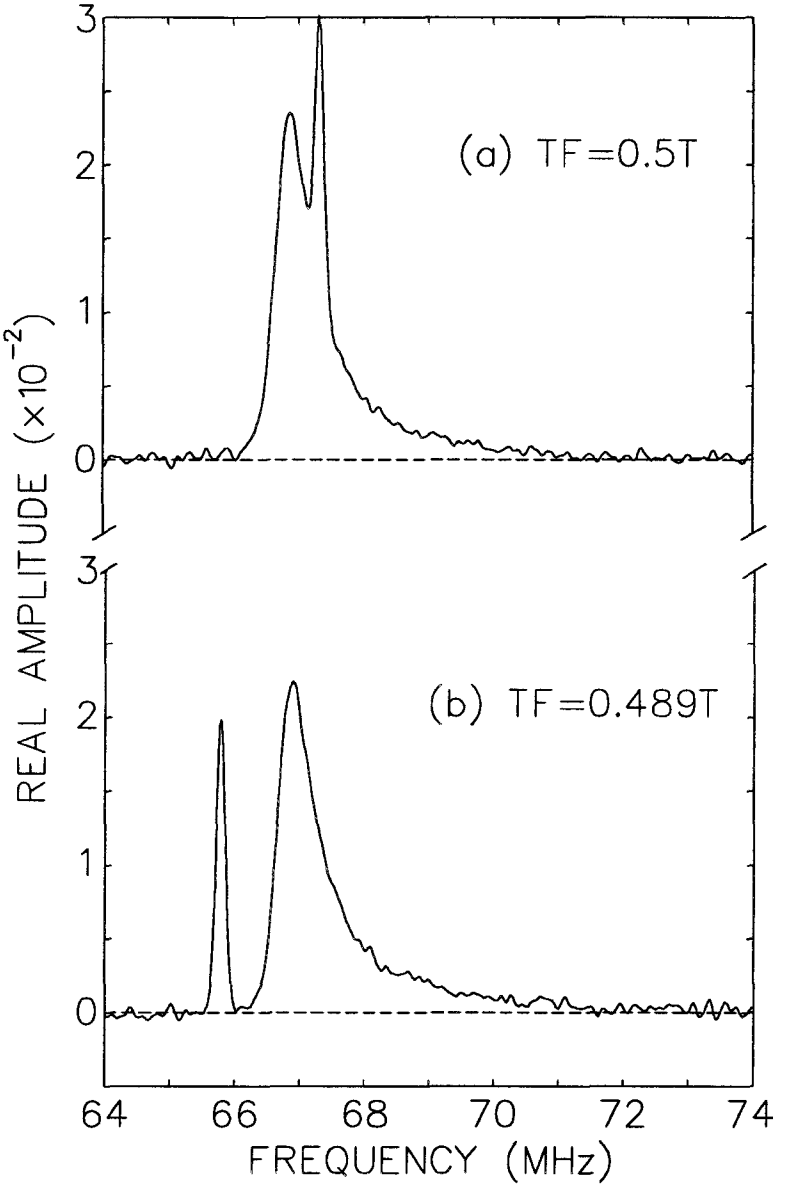

Figure 4.5: (a) The Fourier transform of Fig. 4.3(c) [*i.e.* the same as Fig. 4.4(c)] for $YBa_2Cu_3O_{6.95}$ in a field of 0.5T at 5.8K. (b) Same as in (a) except that the field was lowered by 11.3mT after field cooling to 6K.

Fits to the early part of the signal (*i.e.* the first 1μs) for data below T_c using an equation in the form of Eq. (4.1) with a single gaussian relaxation function of the form $\exp(-\sigma^2 t^2/2)$ and ν_μ pertaining to the average internal field, provides a simplified visual display of the dependence of the lineshape width on temperature. It is straightforward to use the polarization function in Eq. (4.1) to relate the relaxation parameter σ to the second moment $\langle \Delta B^2 \rangle$. The relationship is [68]

$$\langle \Delta B^2 \rangle = \frac{\sigma^2}{\gamma_\mu^2} \tag{4.4}$$

Comparing to Eqs. (3.6), (3.7) and (3.8), one has

$$\sigma \propto \frac{1}{\lambda_{ab}^2} \tag{4.5}$$

Because of the asymmetric shape of the true field distribution, using a gaussian distribution of internal fields gives poor fits to the data. However, the fits are sufficient to provide a crude estimate of the temperature dependence of the second moment. Fig. 4.6 shows the variation of the broadening parameter σ for single gaussian fits of the 0.5T and 1.5T data. Both sets of data suggest that the width of the field distribution varies linearly with temperature below 20K. Furthermore, the broadening of the lineshape appears larger at these low temperatures for the applied field of 0.5T. The linear term appears to weaken slightly at 1.5T. Above 20K the data for the two fields are nearly identical. The single gaussian fits of course cannot determine $\lambda_{ab}(T)$ explicitly, but are useful nonetheless in giving an approximate temperature dependence of $\lambda_{ab}(T)$. They also help facilitate a comparison with previous studies where only single gaussian fits were possible.

A more precise treatment of the data using the phenomenological model of Eq. (3.39), holds the two parameters σ_{eff} and $1/\lambda_{ab}^2$ accountable for the width of the measured field distribution in the sample. Clearly these two parameters must combine to

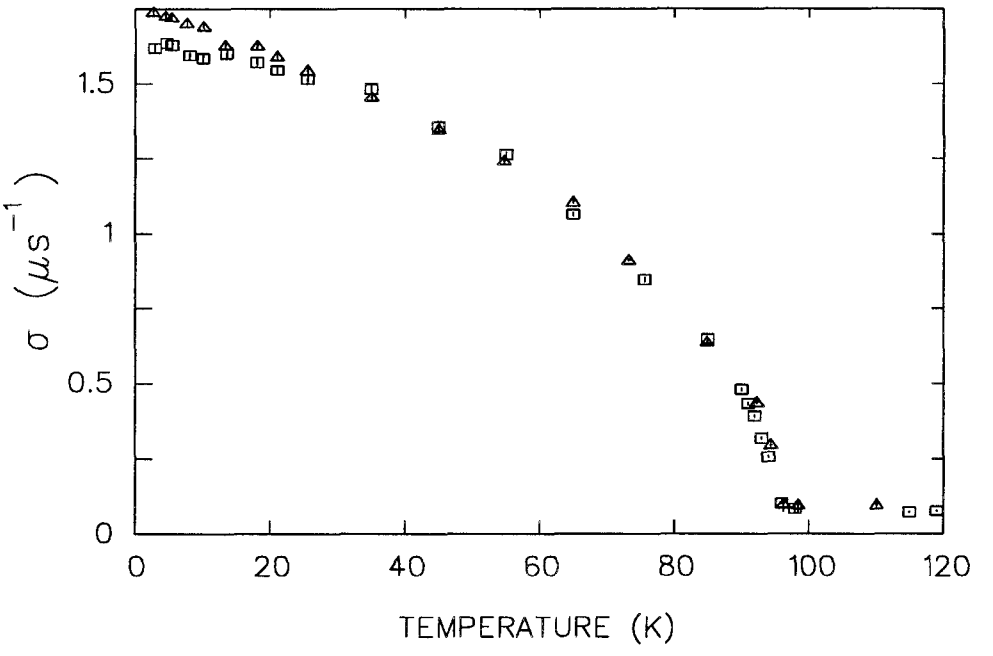

Figure 4.6: The gaussian linewidth parameter σ in $YBa_2Cu_3O_{6.95}$, in magnetic fields 0.5T of (triangles) and 1.5T (squares).

mimic the behaviour in Fig. 4.6. Since σ_{eff} and $1/\lambda_{ab}^2$ both contribute to the linewidth and both are expected to be temperature dependent quantities, the two parameters cannot be treated as independent of one another when analyzing the data. Indeed, fits to the data in which both parameters were free to vary have σ_{eff} and $1/\lambda_{ab}^2$ playing off one another as in Fig. 4.7. A temperature point which appears locally high in the σ_{eff} *vs.* T plot, appears locally low in the $1/\lambda_{ab}^2$ *vs.* T plot and *vice versa.* A plot of $1/\lambda_{ab}^2$ *vs.* σ_{eff} suggests a linear correlation between the two parameters as shown in Fig. 4.8. The solid curve through the points in Fig. 4.8 has the following form:

$$\frac{1}{\lambda_{ab}^2} = \frac{\sqrt{\sigma_{eff}^2 - \sigma_{ns}^2}}{C} \tag{4.6}$$

where the relaxation parameter σ_{ns} [see Eq. (4.1)] is determined by a run taken above T_c in the normal state and C is a constant (*i.e.* the slope) chosen so as to minimize the total χ^2 for all runs in which $T \leq 55$K. In other words, only runs where $T \leq 55$K were considered in determining C since it is the low temperature regime which is of primary importance.

Figure 4.9 shows the total χ^2 arising from global fits of the 0.5T and 1.5T data for various choices of the constant C. The proportionality constant C was found to be $0.0293(10)\mu\text{m}^2\mu\text{s}^{-1}$ and $0.0258(10)\mu\text{m}^2\mu\text{s}^{-1}$ for the 0.5T and 1.5T data, respectively. The depolarization rate σ_{ns} was approximately $0.13\mu\text{s}^{-1}$ and $0.11\mu\text{s}^{-1}$ for the 0.5T and 1.5T fields, respectively.

In the first type of analysis, the total asymmetry amplitude A° for signals recorded below T_c was fixed to the value of the precession amplitude A_{ns}° obtained from fitting data above the transition temperature, prior to determining C in Eq. (4.6). Below T_c the asymmetry amplitude of the measured signal A° is the sum of the precession amplitude of the background signal (A_{bkg}°) and the precession amplitude of the signal originating from within the sample (A_{sam}°). Thus, here we are assuming that the total

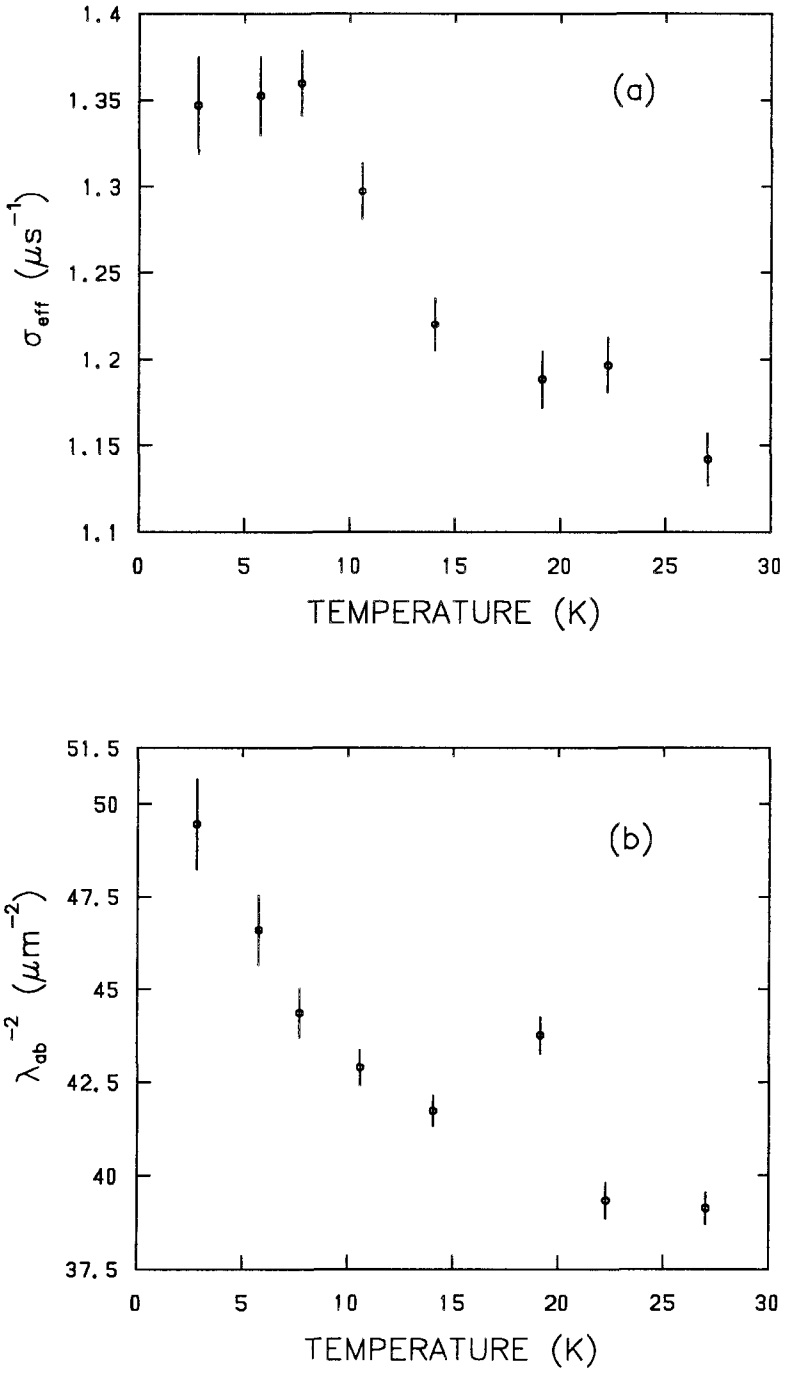

Figure 4.7: The temperature dependence of (a) the gaussian linewidth parameter σ_{eff} and (b) the magnetic penetration depth λ_{ab} in the low temperature regime at a field of 0.5T, as deduced from fitting data with independent σ_{eff} and λ_{ab}.

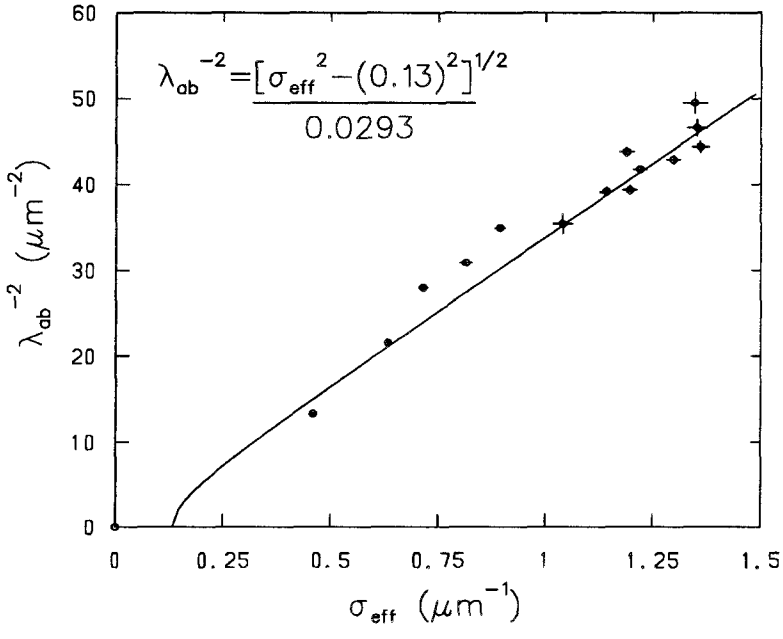

Figure 4.8: The relationship between λ_{ab} and the gaussian broadening parameter σ_{eff}. The solid curve is the equation which appears to the left of the data points.

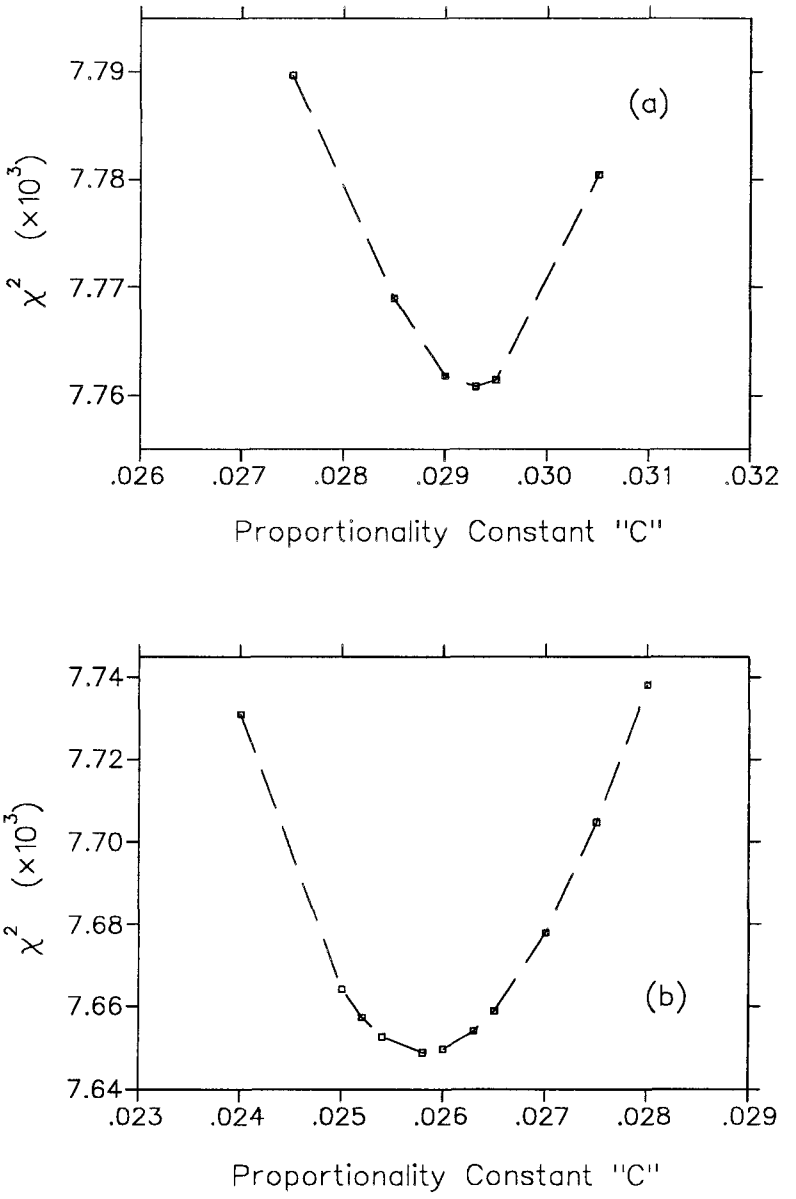

Figure 4.9: The total χ^2 for fits to the (a) 0.5T and (b) 1.5T data below 55K. The dashed lines are guides to the eye.

precession amplitude of the resultant signal is independent of temperature, but dependent upon the applied magnetic field. The asymmetry amplitude above T_c at fields of 0.5T and 1.5T were found to be $A^\circ \approx 0.266(1)$ and $A^\circ \approx 0.247(1)$, respectively. The field dependence is primarily attributed to the finite timing resolution of the counters, which causes the observed precession amplitude to decrease as the period of the muon precession becomes comparable to the timing resolution.

In the final step of this analysis, the status of the fitting parameters was then as follows:

1. **Sample Signal** [refer to Eq. (3.39)]:

Variable parameters:

i) The amplitude A°_{sam}

ii) $1/\lambda^2_{ab}$

iii) The average internal field $\overline{B}$

iv) The initial phase θ

Fixed parameters:

i) κ

ii) σ_{eff} fixed to λ_{ab} according to Eq. (4.6)

2. **Background Signal** [refer to Eq. (4.3)]:

Variable parameters:

i) The field $\overline{B}_{bkg} \approx B_{applied}$

ii) σ_{bkg}

iii) The initial phase θ (same as for sample signal)

Fixed parameters:

i) The amplitude, $A^{\circ}_{bkg} = A^{\circ}_{ns} - A^{\circ}_{sam}$

Thus in the final fit of the data there were six independent parameters. Figure 4.10 shows the variation with temperature of the initial phase θ, the average field $\overline{B}_{bkg}$,the amplitude A°_{bkg} and relaxation rate σ_{bkg} of the background precession signal, obtained from fits of the 0.5T data. As indicated in Fig. 4.10(a), the phase of the initial muon spin polarization remains nearly constant throughout the temperature scan (*i.e.* $\delta\theta \sim 0.05$rad). This implies that there were no appreciable fluctuations in the applied field or electronics. The nearly constant field $\overline{B}_{bkg}$ in Fig. 4.10(b) is a further indication of a highly stable applied magnetic field. The 1.5T data is not shown because there was a significant change in the applied field after 40K.

Figure 4.10(d) shows a significant drop in the relaxation rate of the background signal at higher temperatures, indicating some temperature dependence for σ_{bkg}. However, at lower temperatures ($T \leq 50$K) the background relaxation rate and hence the contribution of the background signal to the second moment exhibits no obvious correlation with temperature. This suggests that σ_{bkg} plays little role in the temperature dependence of σ in Fig. 4.6. The fact that $\sigma_{bkg} > \sigma_{ns}$ suggests that the background is caused by a material with a large nuclear dipolar interaction such as Cu, or is in a region of fairly large field inhomogeneity.

Figure 4.11 and Fig. 4.12 show the temperature dependence of A°_{sam}, $\overline{B}$ and $1/\lambda^2_{ab}$ arising from the same fits which produced the results in Fig. 4.10. Together these parameters constitute three of the four variable parameters (the other being θ) which pertain to the signal originating from the sample. The sample amplitude A°_{sam} depicted

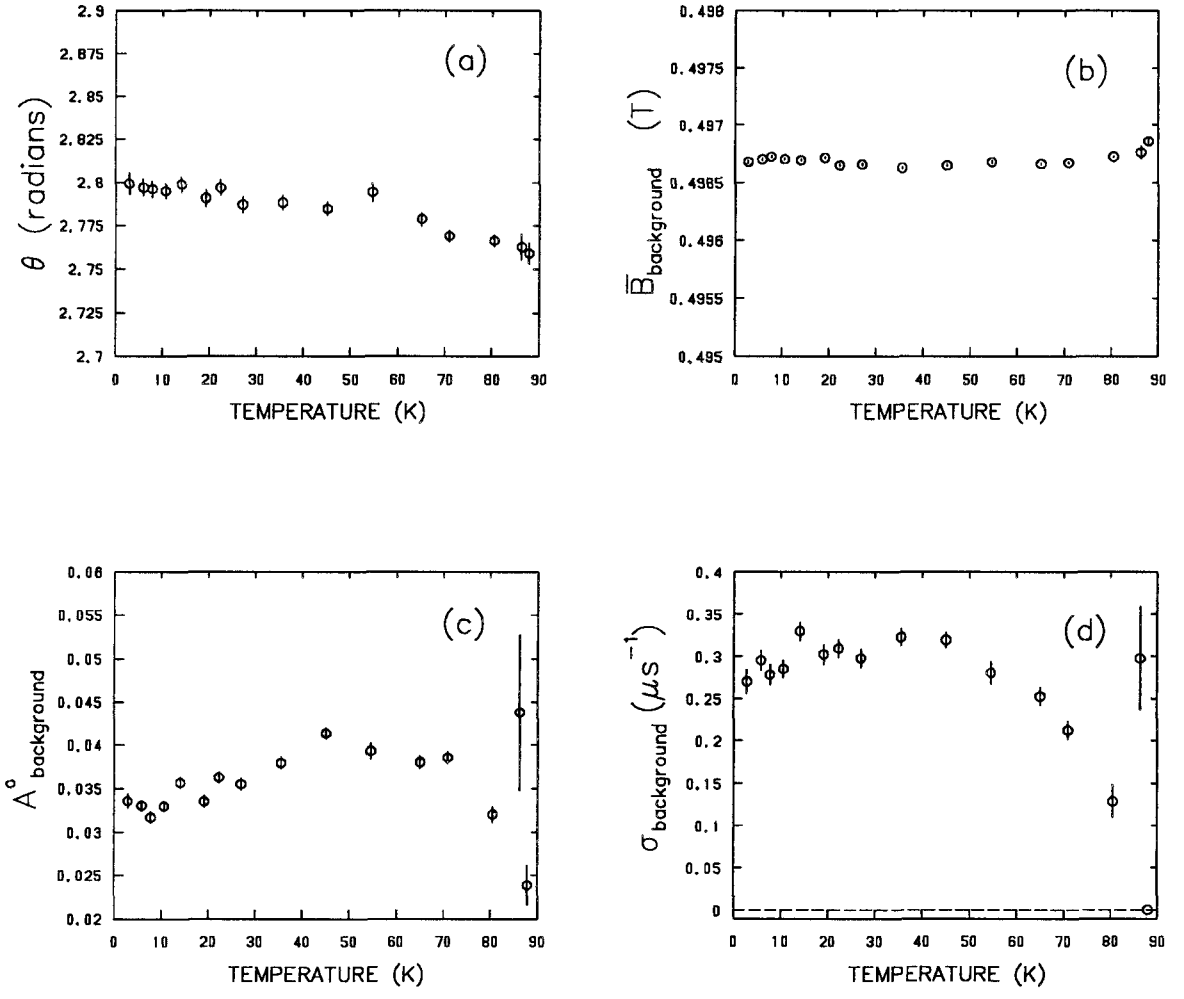

Figure 4.10: The temperature dependence of (a) the initial phase θ, (b) the average field $\overline{B}_{bkg}$, (c) the amplitude A°_{bkg} and (d) the depolarization rate σ_{bkg} corresponding to the background signal produced by muons missing the sample, in an applied field of 0.5T. These results are taken from fits in which the total muon spin precession signal amplitude was fixed to a constant.

in Fig. 4.11(a) shows some scatter and a slight decrease at higher temperatures. The scatter in the asymmetry amplitude is not all that surprising considering that the data was recorded over a period of 5 days, through which time, small fluctuations in experimental conditions were unavoidable. For instance, one such experimental variation was the rate at which ^{4}He was pumped through the cryostat. At higher temperatures (where the required cooling power is low) the amount of ^{4}He flowing into the cryostat and the corresponding pumping rate were minimized in an effort to keep the heater voltage small to preserve the supply of ^{4}He and to reduce thermal gradients between the thermometers and the sample. However, to maintain low temperatures a much larger flow of ^{4}He was required. The increased density of helium atoms in the cryostat increases the probability of scattering the incoming muons before they can reach the sample, thus increasing the background signal and decreasing the magnitude of A°_{sam}. To minimize this effect, the cryostat sample space was pumped on hard, but the choice of a specific combination of ^{4}He-flow rate and the pumping rate was purely judgemental. This is a possible explanation for the scatter observed in Fig. 4.11(a). However, the downward trend of A°_{sam} as one increases the temperature may be purely statistical, as a similar behaviour was not observed in more recently recorded data fitted with the same procedure. Recall that since the total asymmetry amplitude was fixed, the variation of A°_{bkg} with temperature in Fig. 4.10(c) appears as a mirror image of Fig. 4.11(a).

Figure 4.11(b) shows the temperature variation of the average internal field $\overline{B}$ experienced by muons implanted in the $YBa_2Cu_3O_{6.95}$ sample. For comparison, the background field $\overline{B}_{bkg}$ is also plotted in Fig. 4.11(b). In general, the field at any point in the sample is the sum of the local fields in Eq. (3.13). For all temperatures, $\overline{B}$ is less than $\overline{B}_{bkg}$, but $\overline{B}$ appears to approach $\overline{B}_{bkg}$ at both ends of the temperature scan. In

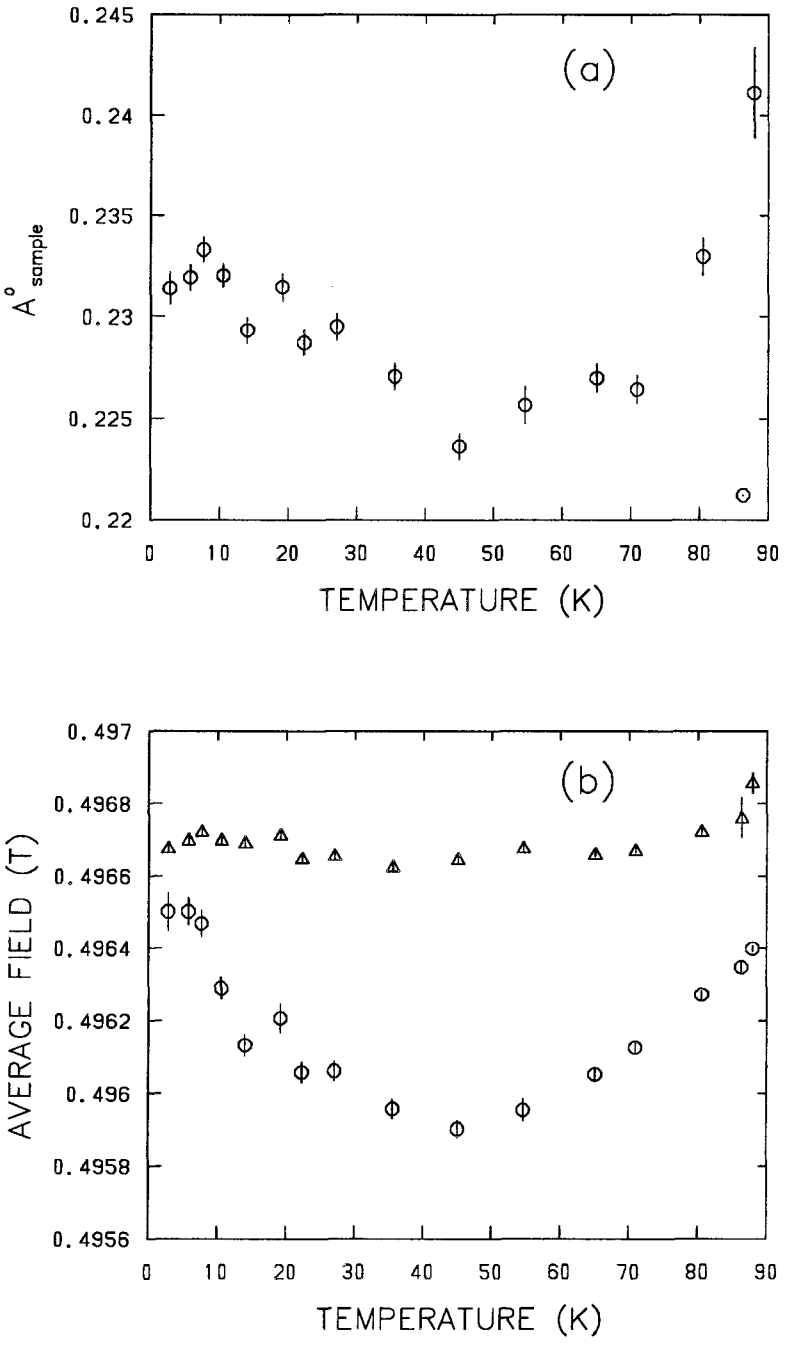

Figure 4.11: The temperature dependence of (a) the muon precession amplitude A°_{sam} and (b) the average internal field $\overline{B}$ (circles), corresponding to the precession signal produced by muons hitting the sample, and the background field $\overline{B}_{bkg}$ (triangles), for an applied field of 0.5T. The total precession signal amplitude was assumed constant in the fits.

the high-temperature regime the vortex cores begin to overlap with the internal field distribution approaching full penetration of the applied field. Thus it is not surprising to see the average internal field $\overline{B}$ approach $\overline{B}_{bkg}$ as one increases the temperature towards T_c. The rise in average field $\overline{B}$ at low temperatures, however, is more difficult to understand. Such an increase has also been reported in previous work by Riseman [77] and observed in more recent data taken at different fields. The cause for such behaviour is puzzling indeed. However, Fig. 4.11(b) is consistent with the time spectrum shown in Fig. 4.3 which shows a more distinct beat in the muon spin precession signal at the intermediate temperature $T = 35.5$K, corresponding to a greater separation between the average precession frequency of muons subjected to the internal field distribution and the average precession frequency of muons in the background field. This suggests that the increase in $\overline{B}$ at low temperatures may be due to some intrinsic phenomenon of the $YBa_2Cu_3O_{6.95}$ sample itself.

Figure 4.12 shows the temperature dependence of $1/\lambda_{ab}^2$ (which in the phenomenological London Model is directly proportional to the superfluid density n_s) for the applied field of 0.5T . Since the relaxation rate σ_{eff} is assumed proportional to $1/\lambda_{ab}^2$ [see Eq. (4.6)], the variation of σ_{eff} with temperature resembles the behaviour in Fig. 4.12. Figure 4.13 shows the low-temperature dependence of $1/\lambda_{ab}^2$ for both 0.5T and 1.5T applied fields. As shown, the presence of a linear term (*i.e.* $1/\lambda_{ab}^2 \propto T$) in the low-temperature region is unmistakeable for both 0.5T and 1.5T fields, with the latter showing a weaker linear dependence on T. A fit to the low-temperature data (*i.e.* below 55K), with an equation of the form:

$$\frac{1}{\lambda_{ab}^2(T)} = \frac{1}{\lambda_{ab}^2(0)}\left[1 - \alpha T - \beta T^2\right] \tag{4.7}$$

gives $\lambda_{ab}(0) = 1451(2)$Å and $\lambda_{ab}(0) = 1496(1)$Å for the 0.5T and 1.5T data respectively, where the quoted uncertainties are purely statistical [87]. It should be noted that this

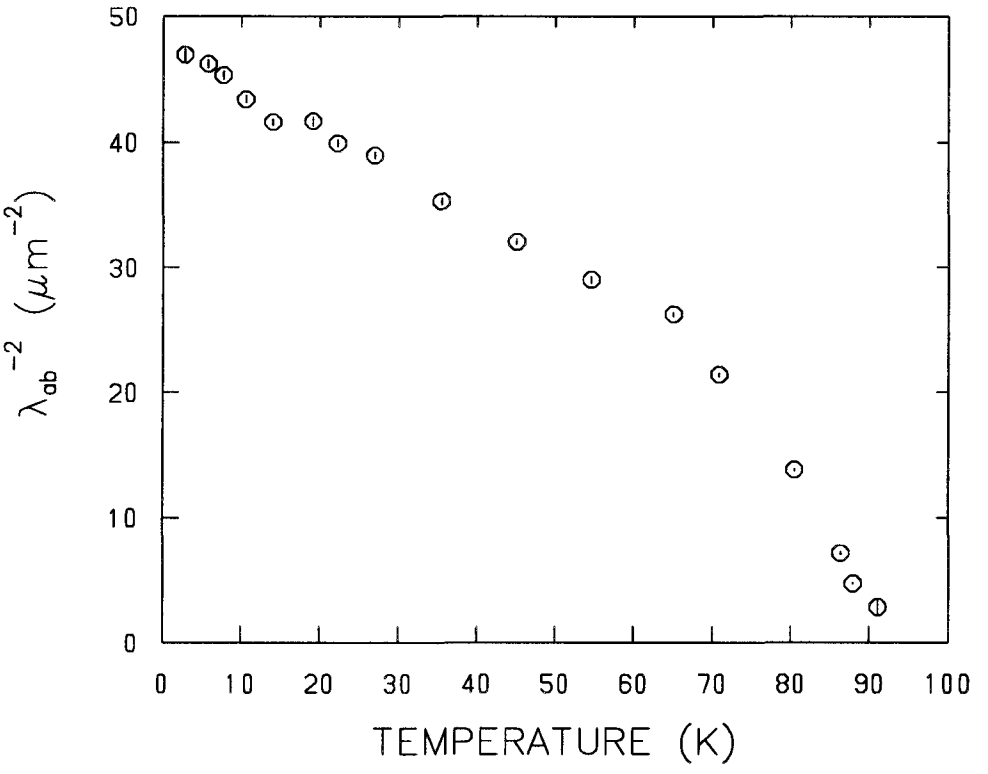

Figure 4.12: The temperature dependence of $1/\lambda_{ab}^2$ in a magnetic field of 0.5T, as determined from fits in which the total precession signal amplitude was assumed constant.

equation is purely phenomenological and cannot be extended to include the higher-temperature data. Both curves suggest that pair breaking persists at the lowest of temperatures in $YBa_2Cu_3O_{6.95}$, which is inconsistent with conventional s-wave pairing of carriers. This low-temperature behaviour indicates a more complicated gap function $\Delta(\vec{k}, T)$ characteristic of the presence of nodes in the energy gap.

In Fig. 4.14 the temperature dependence of λ_{ab} at 0.5T and 1.5T is shown. The solid curves represent microwave measurements of the change in penetration depth $\Delta\lambda_{ab}(T)$ taken in zero static magnetic field by Hardy *et al.* [6]. For the purpose of comparison, $\lambda_{ab}(0)$ for each field is chosen to be the value obtained from fitting the μ^+SR low-temperature data with Eq. (4.7). Surprisingly, the microwave data shows a much better agreement with the μ^+SR data at the higher magnetic field of 1.5T.

There was some concern after completion of the above analysis that fixing the total asymmetry amplitude to the value above T_c may introduce systematic errors by constraining the fits. The large fluctuation in the amplitude of the muon spin precession signal originating from the sample [see Fig. 4.11(a)] was the source of such concerns. Intuitively, we expect that A°_{sam} should scale with the percentage of muons striking the sample. The fluctuations in this percentage during the actual experiment were probably not large enough to account for the large scatter in Fig. 4.11(a). If one dismisses the previous explanation for the large fluctuations in A°_{sam}, it is worth investigating this matter further.

Since A°_{sam} is not expected to change significantly over the temperature scan, the data was refitted first by designating A°_{sam} and A°_{bkg} as variable parameters. As in the previous analysis, σ_{eff} was assumed to be proportional to $1/\lambda^2_{ab}$ through Eq. (4.6). The proportionality constant C was determined to be 0.0250(10) and 0.0243(10)μm$^2\mu$s^{-1} for the 0.5T and 1.5T data respectively. The variable parameters pertaining to the

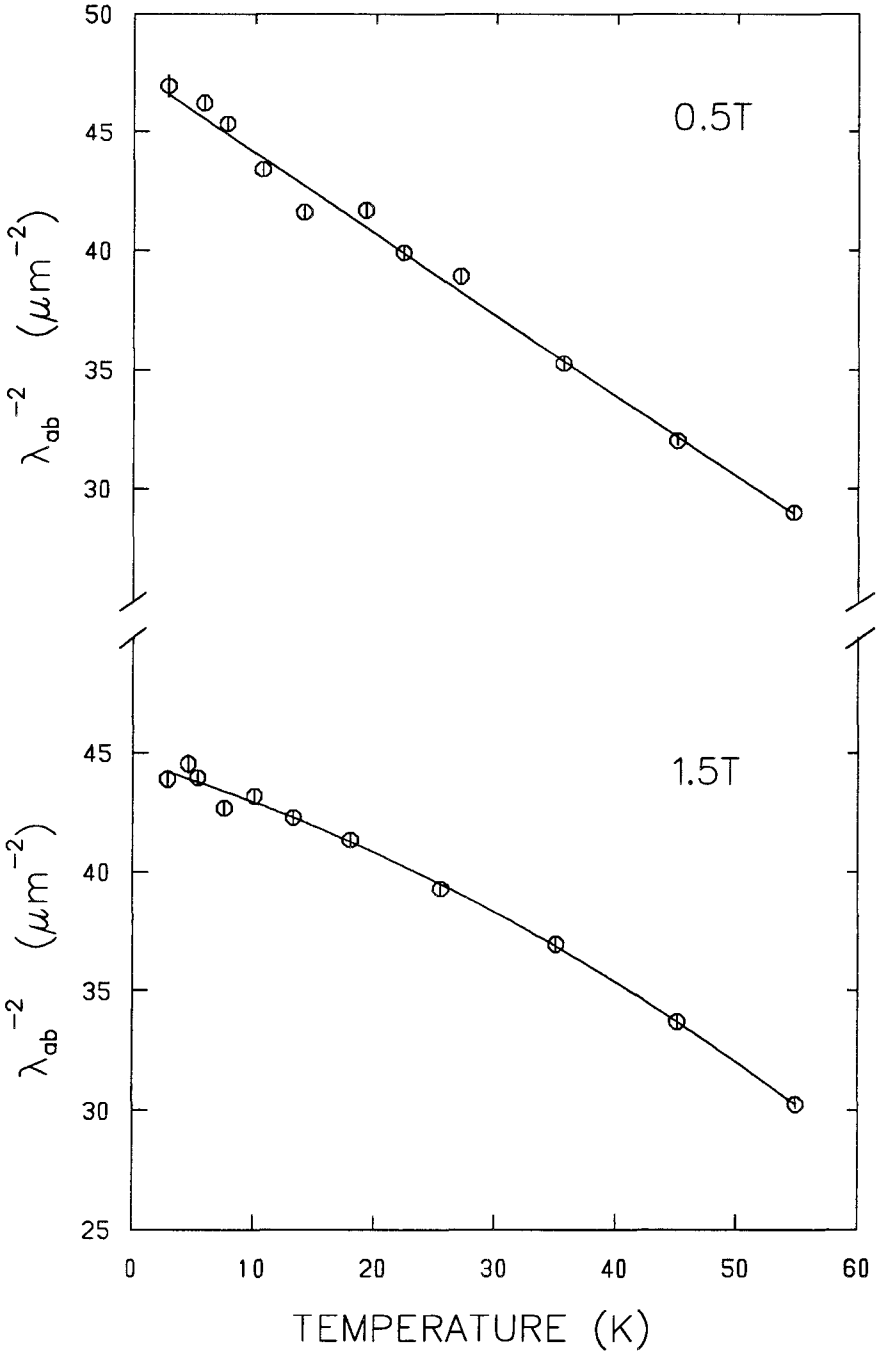

Figure 4.13: The temperature dependence of $1/\lambda_{ab}^2$ in magnetic fields of 0.5T and 1.5T, as determined from fits in which the total precession signal amplitude was assumed constant. The solid lines are fits to Eq. (4.7).

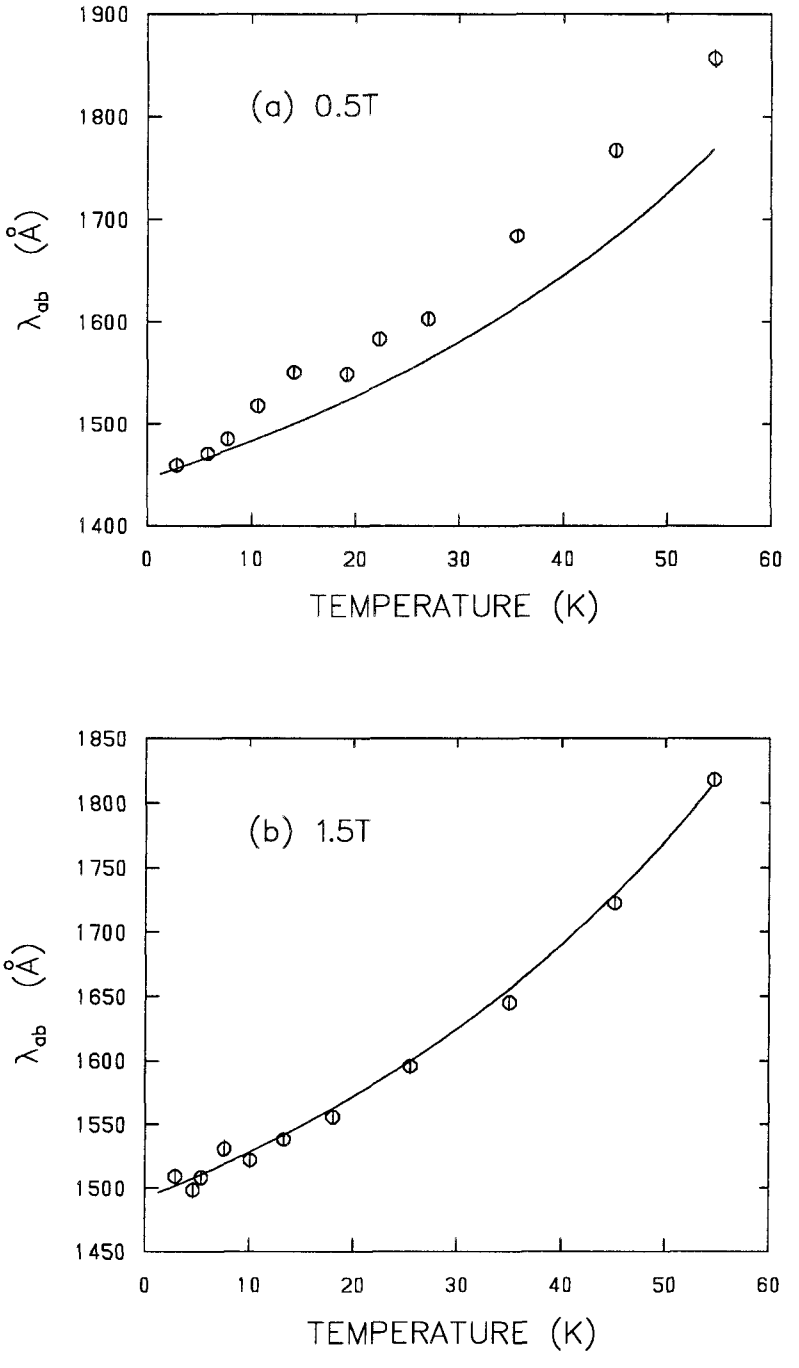

Figure 4.14: The temperature dependence of λ_{ab} at (a) 0.5T and (b) 1.5T. The solid lines show the microwave measurements of $\Delta\lambda_{ab}(T)$ in zero field from Ref. [6], assuming $\lambda_{ab}(0) = 1451$ and 1496Å in (a) and (b) respectively.

background precession signal varied with temperature according to Fig. 4.15. Comparing with Fig. 4.10, the phase θ shifts down $\sim$ 0.005rad, while $\overline{B}_{bkg}$ shifts upward $\sim$ 0.05mT. The degree of fluctuation in both these parameters appears similar to that of the previous analysis, so again it seems apparent that there were negligible fluctuations in the applied field.

The amplitude A°_{bkg} and the relaxation rate σ_{bkg} [see Fig. 4.15(c) and Fig. 4.15(d)] show almost no change from the results depicted in Fig. 4.10. Even the size of the statistical error bars are comparable. These results indicate that the fitting program is capable of clearly separating the unwanted background signal from the sample signal.

Figure 4.16(a) shows the temperature dependence of the amplitude A°_{sam} corresponding to the muon spin precession signal originating from the sample. The downward trend with increasing T appears slightly more prominent than in Fig. 4.11(a). The temperature dependence of $\overline{B}$ in Fig. 4.16(b) is significantly different from that in the previous analysis. The average field $\overline{B}$ is greater than $\overline{B}_{bkg}$ at the lowest of temperatures and does not dip as far below $\overline{B}_{bkg}$ as in Fig. 4.11(b) for temperatures beyond this. At the high-temperature end in Fig. 4.11(b), $\overline{B}$ recovers to approximately the same value as in Fig. 4.11(b). Again the rise in $\overline{B}$ at low temperatures is surprising. It is possible that this is an effect due to $\vec{a}$-$\vec{b}$ anisotropy. The presence of $\vec{a}$-$\vec{b}$ anisotropy would distort the vortex lattice into isoceles triangles as shown in Fig. 3.9. If this lattice were to be modelled by one consisting of equilateral triangles as assumed in our analysis, then there would be some error in the determination of the average field $\overline{B}$. This would be a greater problem at low temperatures where the cores are further apart and errors in spectral weighting are more pronounced.

The low-temperature dependence of $1/\lambda^2_{ab}$ is shown in Fig. 4.17. Surprisingly, the scatter in the data points is not significantly greater than in Fig. 4.13. Noticeably

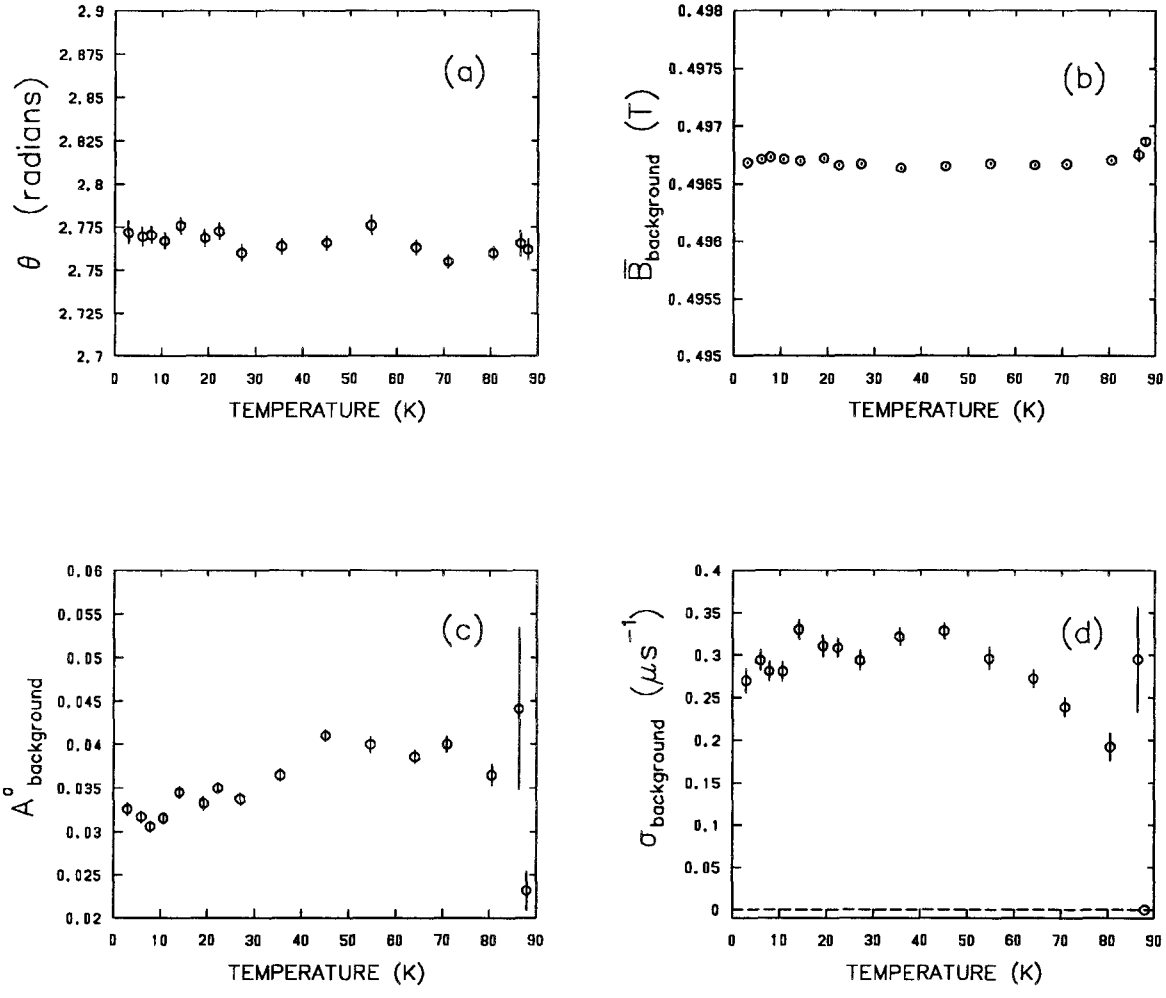

Figure 4.15: The temperature dependence of (a) the initial phase θ, (b) the average field $\overline{B}_{bkg}$, (c) the amplitude A°_{bkg} and (d) the depolarization rate σ_{bkg} corresponding to the background signal produced by muons missing the sample, in an applied field of 0.5T. These results are taken from fits in which A°_{sam} and A°_{bkg} were free to vary.

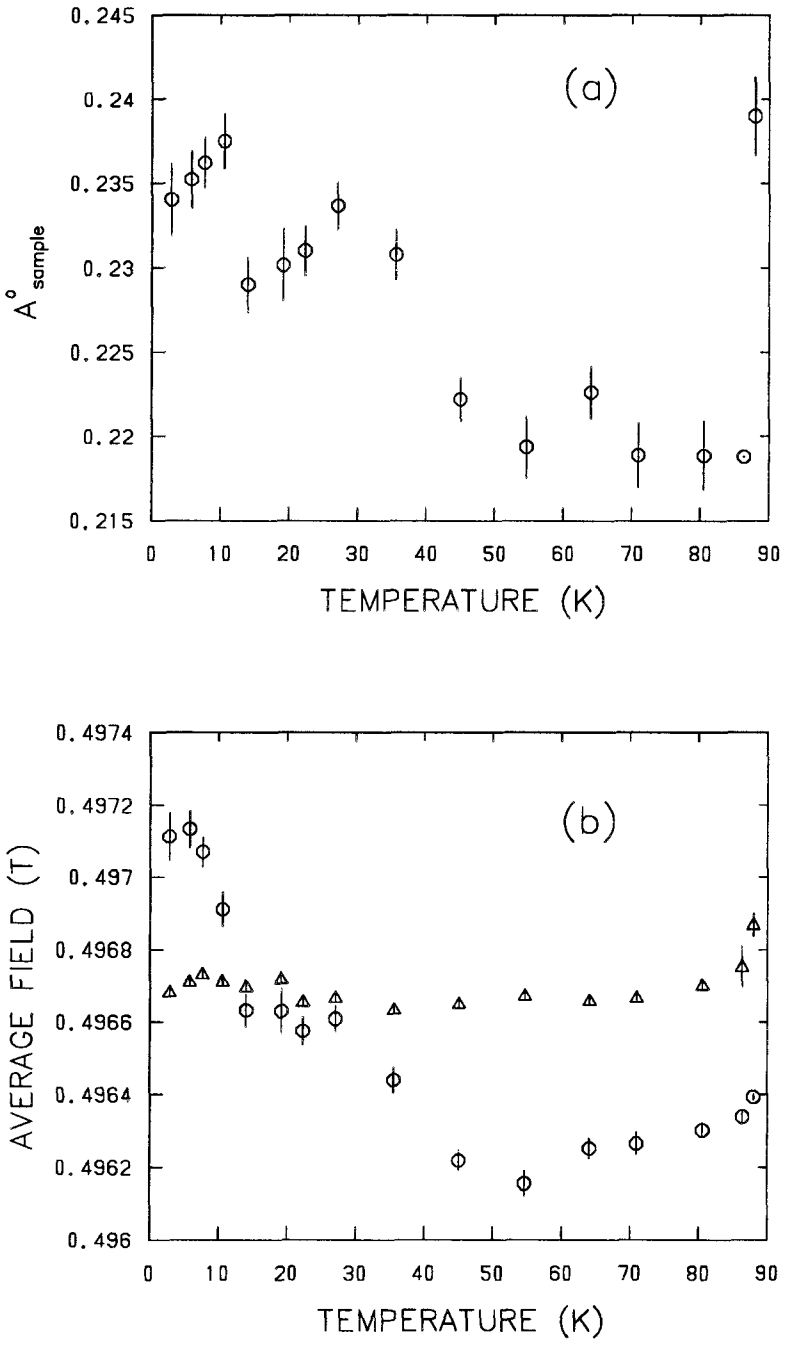

Figure 4.16: The temperature dependence of (a) the muon precession amplitude A°_{sam} and (b) the average internal field $\overline{B}$ (circles), corresponding to the precession signal produced by muons hitting the sample, and the background field $\overline{B}_{bkg}$ (triangles), for an applied field of 0.5T. A°_{sam} and A°_{bkg} were both independently variable parameters in the fits.

different however, is an increase in the linear term (see Table 4.1). Furthermore, fits to Eq. (4.6) yield $\lambda_{ab}(0) = 1350(2)$Å and $\lambda_{ab}(0) = 1437(1)$Å for the 0.5T and 1.5T data, respectively. A comparison to the microwave measurements of Hardy *et al.*, assuming these values for $\lambda_{ab}(0)$ is shown in Fig. 4.18. There appears to be even less agreement at 0.5T than previously noted in Fig. 4.14(a). However, the agreement at 1.5T in Fig. 4.18(b) is comparable to that in Fig. 4.14(b) despite the significant difference in $\lambda_{ab}(0)$.

As a final step in the analysis, the data was refitted with the amplitude A°_{sam} fixed to the average value of the data below 55K in Fig. 4.16(a). This results in a noticeable reduction in the scatter for the parameters A°_{bkg} and σ_{bkg} (see Fig. 4.19). Fixing A°_{sam} in this way significantly shifts the data points above 40K. This is not surprising since A°_{sam} was fixed to the low-temperature average. The phase θ shows a slight decrease at high temperatures [see Fig. 4.19(a)] and $\overline{B}$ levels off above 40K [see Fig. 4.20(b)]. These results suggest that fixing A°_{sam} to the low-temperature average reduces the scatter in the low-temperature data, but it is not yet clear whether or not we are introducing non-physical deviations in the high-temperature region.

The reduction in scatter is most noticeable in Fig. 4.21 which shows the temperature dependence of $1/\lambda^2_{ab}$. From Eq. (4.6) we find $\lambda_{ab}(0) = 1362(2)$Å and $\lambda_{ab}(0) = 1445(1)$Å for the 0.5T and 1.5T data, respectively. A plot of the temperature dependence of $1/\lambda^2_{ab}$ over the full temperature scan is shown in Fig. 4.22. The two fields appear to converge well before T_c, but the crossover is difficult to determine. As shown in Fig. 4.23, there is improved agreement between the microwave measurements and the 0.5T μ^+SR data, while the agreement with the 1.5T data is comparable to that of the previous two fitting methods. The total asymmetry amplitude of the muon spin precession signal as determined from all three fitting procedures is shown in Fig. 4.24. It appears as

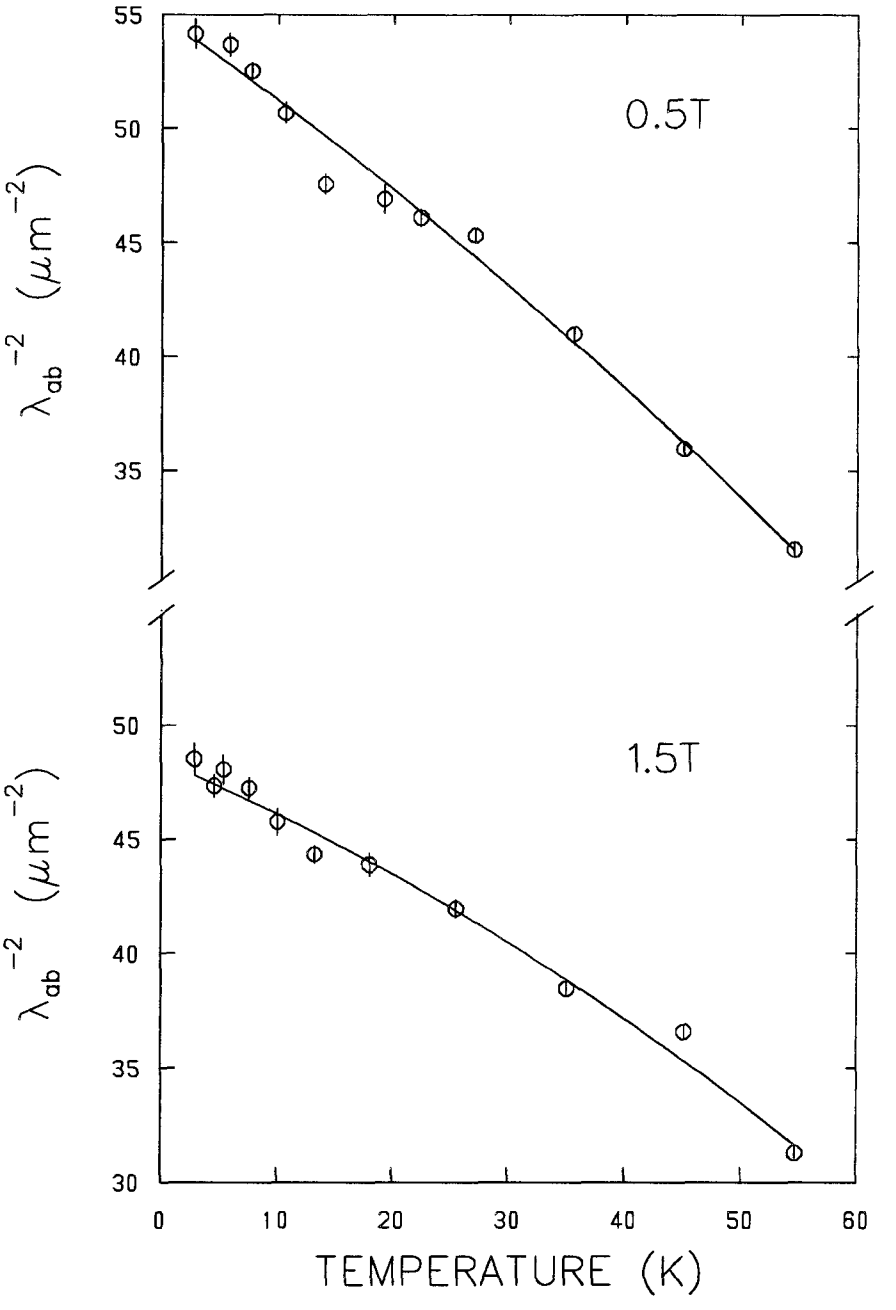

Figure 4.17: The temperature dependence of $1/\lambda_{ab}^2$ in magnetic fields of 0.5T and 1.5T, as determined from fits in which A_{sam}° and A_{bkg}° were variable parameters. The solid lines are fits to Eq. (4.7).

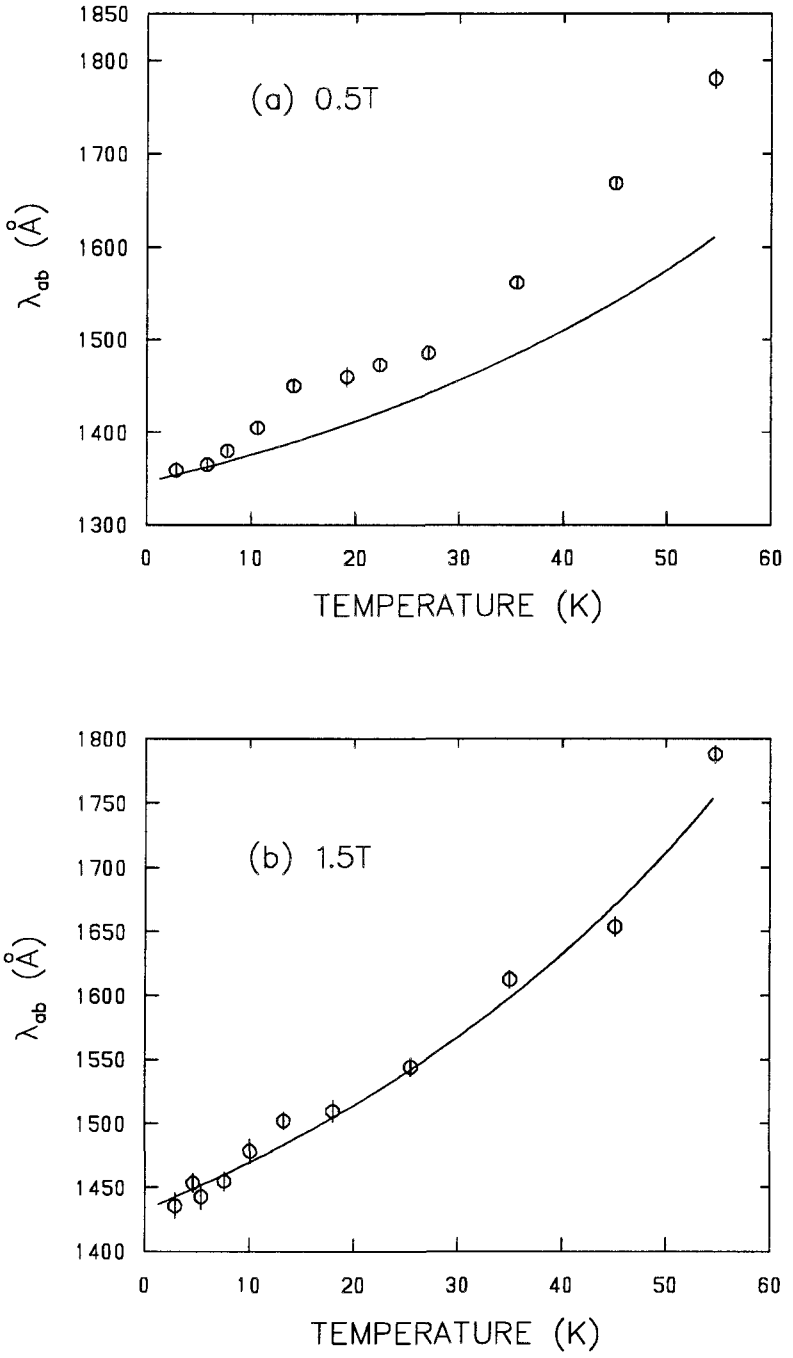

Figure 4.18: The temperature dependence of λ_{ab} at (a) 0.5T and (b) 1.5T. The solid lines show the microwave measurements of $\Delta\lambda_{ab}(T)$ in zero field from Ref.[6], assuming $\lambda_{ab}(0) = 1350$ and 1437Å in (a) and (b), respectively.

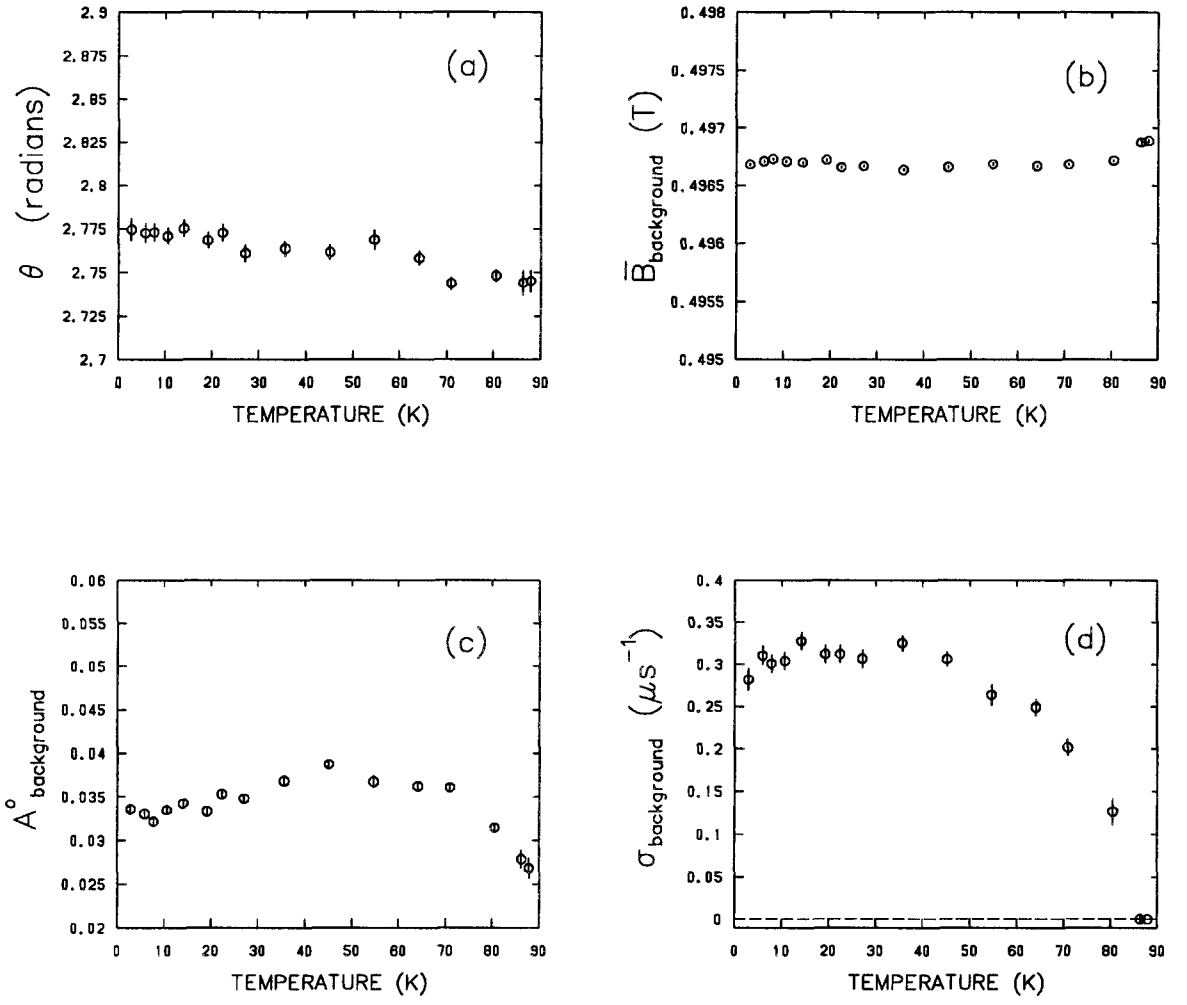

Figure 4.19: The temperature dependence of (a) the initial phase θ, (b) the average field $\overline{B}_{bkg}$, (c) the amplitude A°_{bkg} and (d) the depolarization rate σ_{bkg} corresponding to the background signal produced by muons missing the sample, in an applied field of 0.5T, from fits where A°_{sam} is assumed constant.

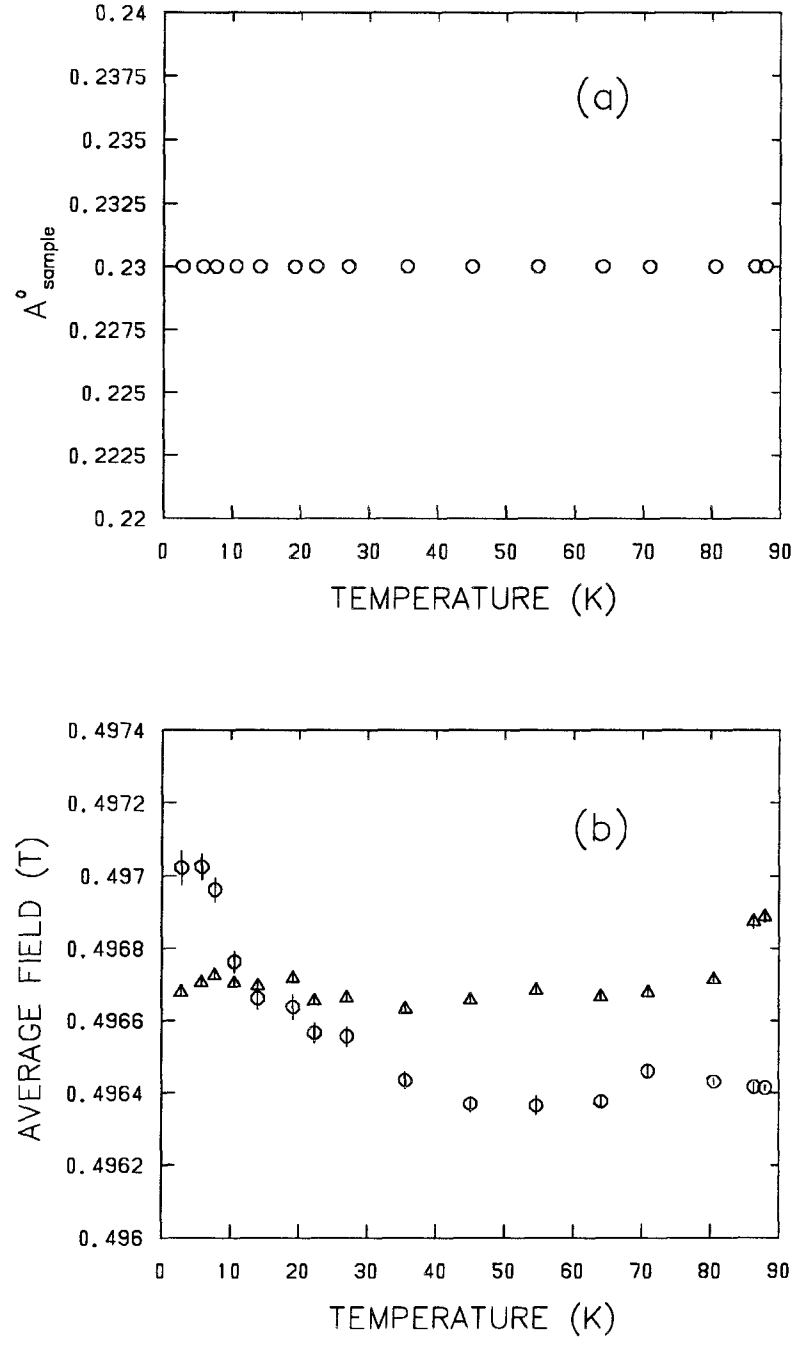

Figure 4.20: The temperature dependence of (a) the muon precession amplitude A°_{sam} and (b) the average internal field $\overline{B}$ (circles), corresponding to the precession signal produced by muons hitting the sample, and the background field $\overline{B}_{bkg}$ (triangles), for an applied field of 0.5T.

though one is justified in fixing the total asymmetry amplitude, as the average values are comparable.

The results from all three types of analysis are summarized in Table 4.1. Methods (ii) and (iii) give comparable results, but differ substantially from method (i). The difference appears to be related to the proportionality constant C of Eq. (4.6). As C increases, so does $\lambda_{ab}(0)$.

It should be noted that for method (i) in Table 4.1, the total asymmetry amplitude was fixed prior to the determination of C. This may in fact be the most significant difference between method (i) and the other fitting procedures, in which C was determined before fixing any additional parameters. To see if this is the case, the 0.5T data was refit, by first determining the proportionality constant C and then fixing the total asymmetry amplitude to the average value for the data below 55K (see method (iv) in Table 4.1). Remarkably, the total asymmetry amplitude was found to be the same as in method (i) (*i.e.* $A^{\circ} \approx 0.2650$). The linear coefficient α and the quadratic coefficient β [determined by fitting the low-temperature data to Eq. (4.7)] are virtually the same for methods (i) and (iv), but the values obtained for $\lambda_{ab}(0)$ are very different. Moreover, the value of $\lambda_{ab}(0)$ from method (iv) is comparable to (ii) and (iii). All of this implies that $\lambda_{ab}(0)$ is significantly influenced by changes in C, but is little affected by the manner in which the amplitude of the precession signal is treated in the fitting procedure. Also, the deviations in the linear term from one method to the next are likely not significant enough to suggest that there is any difference in the behaviour of $\lambda_{ab}(T)$ at low temperatures.

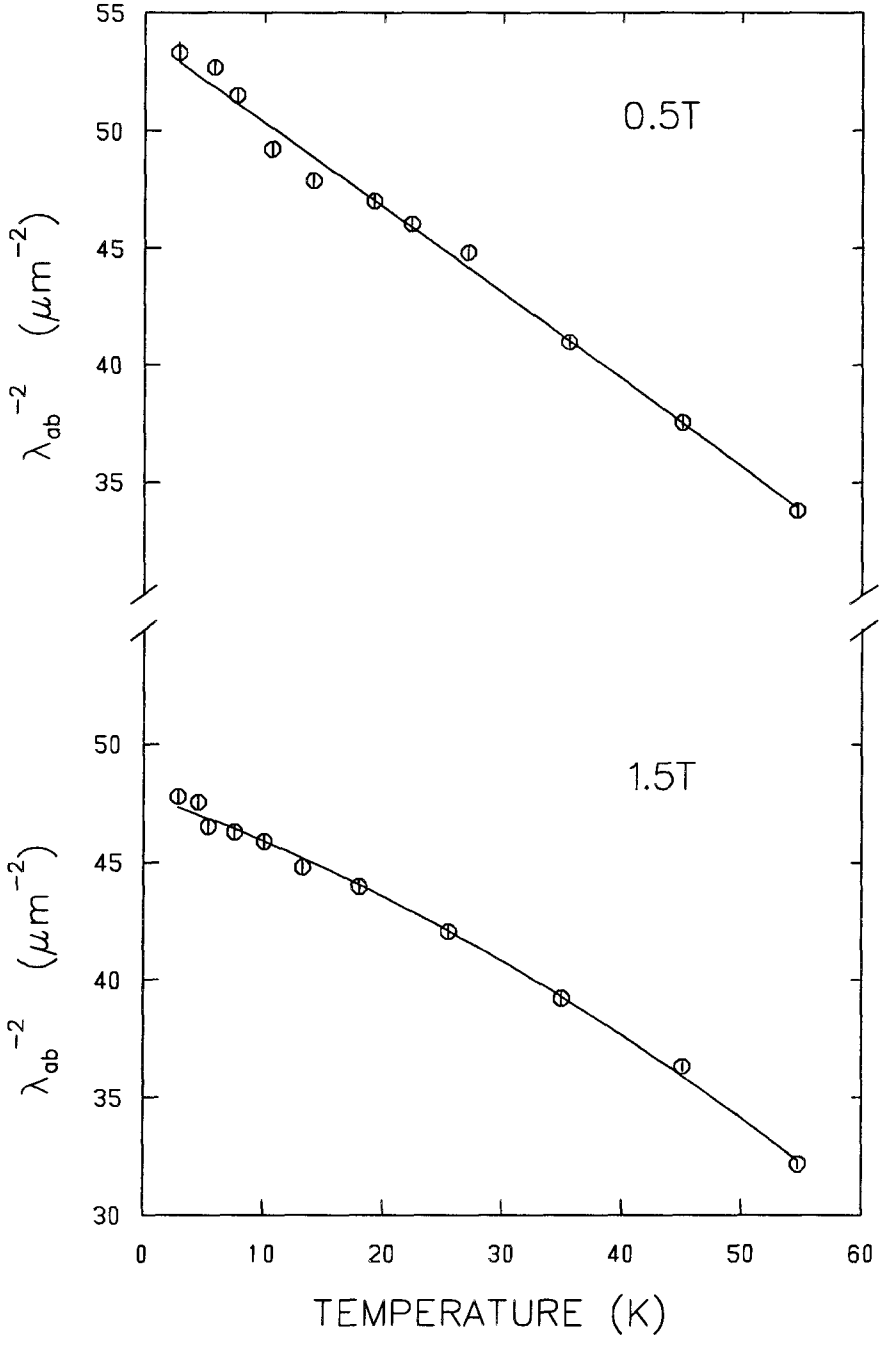

Figure 4.21: The temperature dependence of $1/\lambda_{ab}^2$ in magnetic fields of 0.5T and 1.5T, as determined from fits in which A_{sam}° was assumed to be constant. The solid lines are fits to Eq. (4.7).

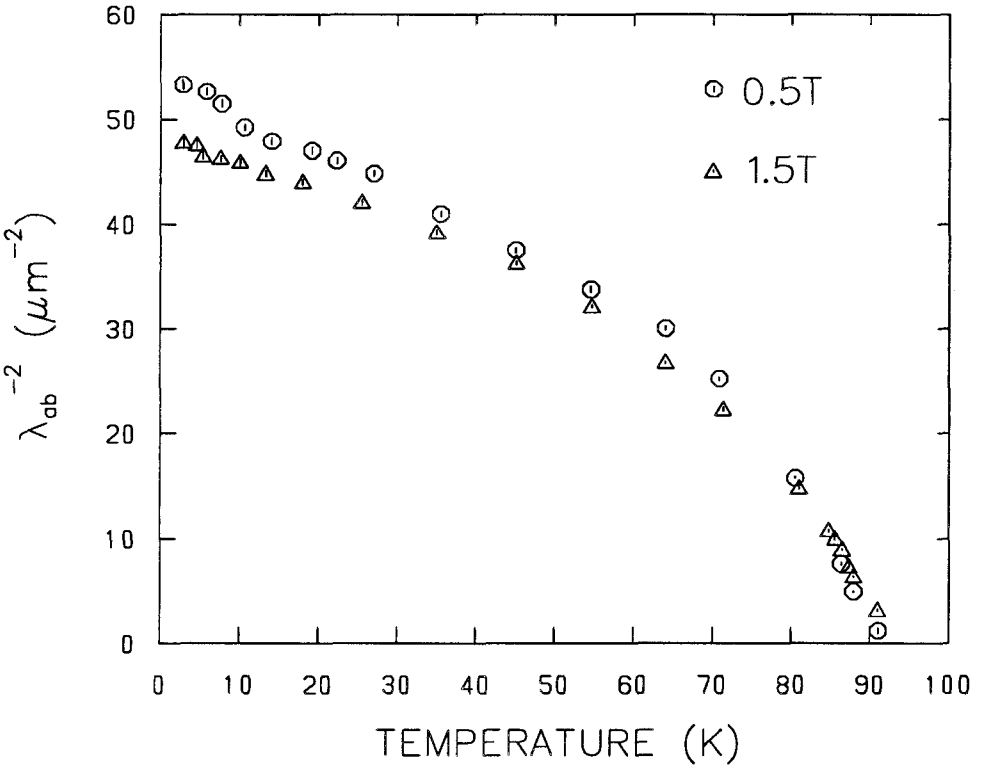

Figure 4.22: The temperature dependence of $1/\lambda_{ab}^2$ in magnetic fields of 0.5T and 1.5T, as determined from fits in which A_{sam}° was assumed to be constant.

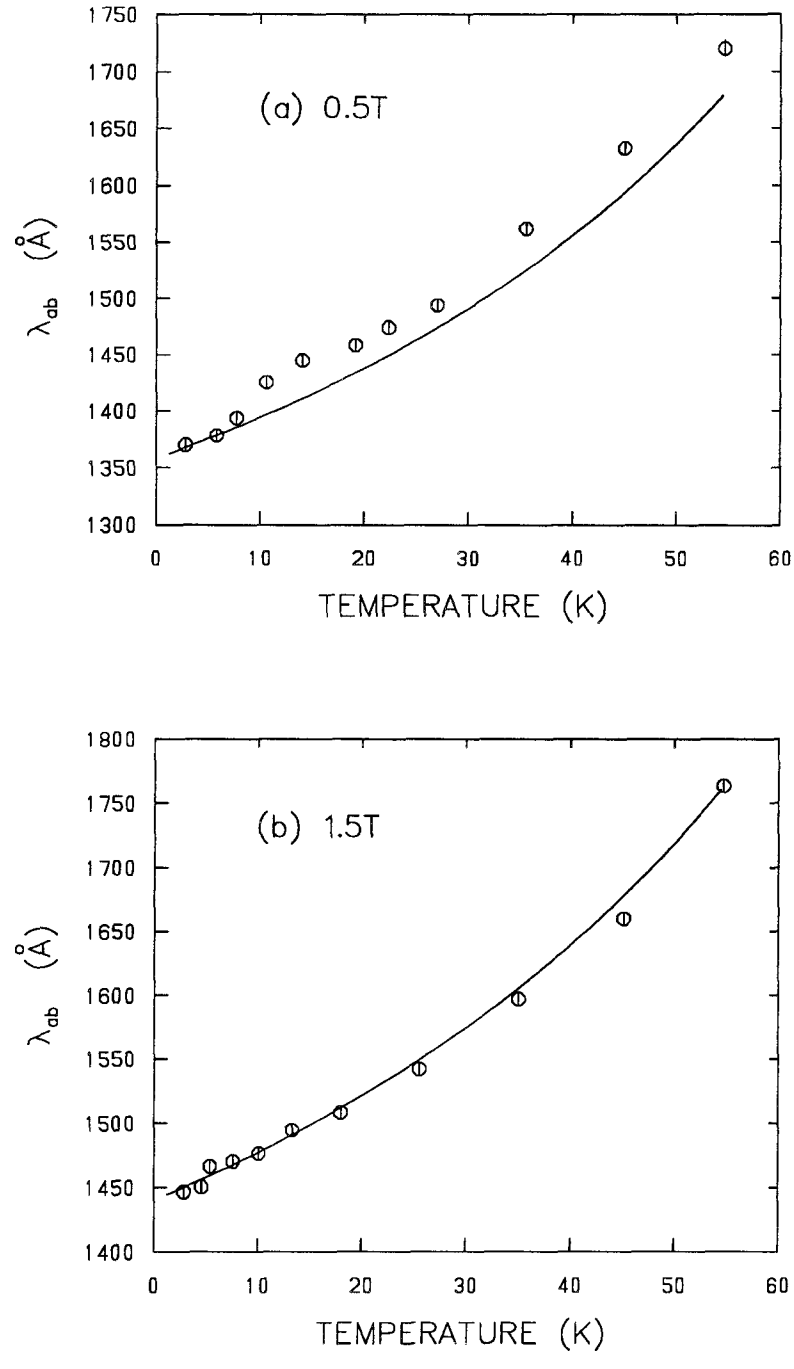

Figure 4.23: The temperature dependence of λ_{ab} at (a) 0.5T and (b) 1.5T. The solid lines show the microwave measurements of $\Delta\lambda_{ab}(T)$ in zero field from Ref.[6], assuming $\lambda_{ab}(0) = 1362$ and 1445Å in (a) and (b) respectively.

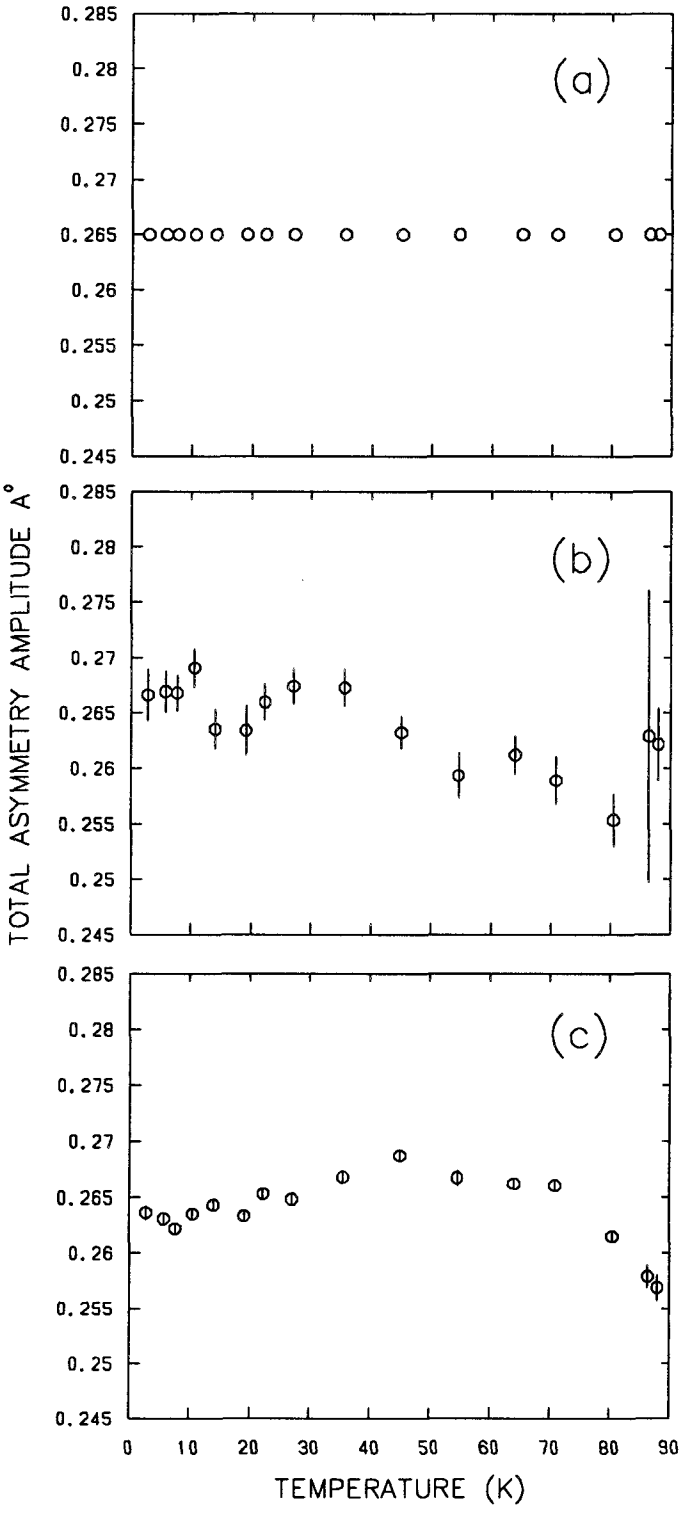

Figure 4.24: The temperature dependence of the total asymmetry amplitude at 0.5T for three different fitting procedures: (a) $(A^{\circ}_{sam} + A^{\circ}_{bkg})$ is fixed to a constant value; (b) A°_{sam} and A°_{bkg} are independent parameters; (c) A°_{sam} is a fixed parameter.

Fitting Procedure	*Applied Field (T)*	*"C" from* Eq. (3.6) ($\mu m^2 \mu s^{-1}$)	$\lambda_{ab}(0)$ (Å)	α (K^{-1})	β (K^{-2})
Method (i):					
$(A^{\circ}_{sam} + A^{\circ}_{bkg})$ is "fixed before" determining C	0.5	0.0293	1451(2)	$7.2(1) \times 10^{-3}$	0
	1.5	0.0258	1496(1)	$3.4(5) \times 10^{-3}$	$4.5(8) \times 10^{-5}$
Method (ii):					
A°_{sam} and A°_{bkg} are "free"	0.5	0.0250	1350(2)	$6.4(1) \times 10^{-3}$	$2.6(1) \times 10^{-5}$
	1.5	0.0243	1437(1)	$4.4(1) \times 10^{-3}$	$3.5(1) \times 10^{-5}$
Method (iii):					
A°_{sam} is "fixed"	0.5	0.0250	1362(2)	$6.5(1) \times 10^{-3}$	$4.8(2) \times 10^{-6}$
	1.5	0.0243	1445(1)	$3.7(1) \times 10^{-3}$	$4.2(1) \times 10^{-4}$
Method (iv):					
$(A^{\circ}_{sam} + A^{\circ}_{bkg})$ is "fixed after" determining C	0.5	0.0250	1347(2)	$7.7(3) \times 10^{-3}$	0

Table 4.1: Comparison of the fitting procedures.

Chapter 5

Conclusion

The observation of a linear temperature dependence below 50K for $1/\lambda_{ab}^2$ is in agreement with the microwave cavity measurements of Hardy *et al.* on similar $YBa_2Cu_3O_{6.95}$ crystals in zero applied field [6]. Both experiments provide further evidence for unconventional pairing of carriers in the superconducting state. These results of course contradict previous μ^+SR studies, which found a much weaker low-temperature behaviour for λ_{ab} [9]. The likelihood of impurity scattering playing a role in suppressing λ_{ab} in such a way as to simulate conventional s-wave behaviour has been made more plausible by recent measurements on Zn-doped crystals [84,88]. These measurements show a distinct weakening of the linear term at low temperatures due to the added Zn impurity. Thus it is possible that the presence of impurities, as well as a lack of good low-temperature data may have lead to a misinterpretation in some of the previous μ^+SR experiments.

The difficulties in analyzing μ^+SR data of this nature have been addressed as much as possible in this study. The large number of variable parameters requires one to make some plausible assumptions in the fitting procedure. Fortunately, all variations of the analysis considered in this report arrive at the same conclusion regarding the behaviour of $\lambda_{ab}(T)$ at low temperatures; namely, a strong linear term exists. Furthermore, the strength of the linear term is comparable for all forms of analysis considered. This implies that the observed low-temperature linear dependence of $1/\lambda_{ab}^2$ is not an artificial manifestation of the fitting procedure itself. This notion is further supported by the

obseravtion of a linear term in the single gaussian fits, which provide a crude estimate of the second moment.

The weakening of the linear term at 1.5T (or conversely, the strengthening of the linear term at 0.5T) was surprising indeed. The magnetic penetration depth is not expected to be field dependent in this low-field regime. Theoretically there is no low-field limit associated with the field distribution used to model the vortex lattice. Eq. (3.9) is simply an extension of the London model which has no low-field limit.

One possible explanation for the observed field dependence is quasiparticle scattering off of the vortex cores, which we know to be static, as evidenced by the field-shifted results of Fig. 4.5. One can imagine this effect to be enhanced at higher magnetic fields, where the flux-line density is greater in the sample. A scattering process of this nature may be similar to the impurity scattering which appears to weaken the linear term in the Zn-doped samples.

It is possible that the observed low-temperature field dependence for λ_{ab} is somehow linked to the $\vec{a}$-$\vec{b}$ anisotropy in the penetration depth, not considered here. It is important to stress that none of the previous μ^+SR studies included $\vec{a}$-$\vec{b}$ anisotropy in determining the temperature dependence of λ_{ab}, either. Consequently, it cannot be held accountable for the observation of a linear term in the present study.

Another puzzling observation comes from the comparison of the temperature dependence of λ_{ab} with that obtained from the microwave cavity measurements. The 1.5T data agrees well with the microwave results for all forms of the analysis. On the other hand, the 0.5T data shows poor agreement with the microwave measurements. The better agreement with the higher-field μ^+SR data is surprising since the microwave measurements were performed in zero static magnetic field. However, there are some questions as to whether the two types of measurements can be compared at this level

due to the very different nature of the two methods. In the microwave studies the measured penetration depth pertains to the length scale over which very weak shielding currents flow around the perimeter of the sample. In the μ^+SR studies one is measuring the penetration depth associated with supercurrents circulating around the vortex cores in the bulk of the sample.

Finally, something must be said about the uncertainty in the μ^+SR measurements. This study gives $\lambda_{ab}(0)$ in the range $1347 - 1451$Å and $1437 - 1496$Å depending on the analysis, for the 0.5T and 1.5T fields, respectively. However, the errors in these results are difficult to determine. The systematic errors are much larger than the statistical errors quoted in Table 4.1 and those which appear on the graphs throughout this report. Thermal and magnetic field fluctuations during the experiment are difficult to assess, but these uncertainties are likely negligible compared to those introduced in the fitting procedure. Although there is some question regarding the accuracy of the $\lambda_{ab}(0)$ values obtained, there is exciting new qualitative information to be obtained from this μ^+SR study. Namely, evidence for unconventional pairing of carriers in the superconducting state of $YBa_2Cu_3O_{6.95}$ and the possible existence of a low-temperature field dependence for λ_{ab}.

Bibliography

[1] P. Monthoux, A. Balatsky and D. Pines, Phys. Rev. Lett. **67**, 3448 (1991).

[2] N. Bulut and D.J. Scalapino, Phys. Rev. Lett. **67**, 2898 (1991).

[3] F. Gross *et al.*, Z. Phys. B **64**, 175 (1986).

[4] J. Annett, N. Goldenfeld and S.R. Renn, Phys. Rev. B **43**, 2778 (1991).

[5] M. Prohammer and J.P. Carbotte, Phys. Rev. B **43**, 5370 (1991).

[6] W. Hardy, D.A. Bonn, D.C. Morgan, R.X. Liang and Kuan Zhang, Phys. Rev. Lett. **70**, 3999 (1993).

[7] P.J. Hirshfeld and N. Goldenfeld, Phys. Rev. B **48**, 4219 (1993).

[8] Z. Ma, R.C. Taber, L.W. Lombardo, A. Kapitulnak, M.R. Beasley, P. Merchant, C.B. Eom, S.Y. Hou and J.M. Phillips, Phys. Rev. Lett. **71**, 781 (1993).

[9] D.R. Harshmann *et al.*, Phys. Rev. B **36**, 2386 (1987); R.F. Kiefl *et al.*, Physica C **153-155**, 757 (1988); Y.J. Uemura *et al.*, Phys. Rev. B **38**, 909 (1988); D.R. Harshmann *et al.*, Phys. Rev. B **39**, 851 (1989); B. Pümpin *et al.*, Phys. Rev. B **42**, 8019 (1990).

[10] Kuan Zhang, D.A. Bonn, S. Kamal, Ruixing Liang, D.J. Barr, W.N. Hardy, D. Basov and T. Timusk, *Measurement of the ab Plane Anisotropy of Microwave Surface Impedance of Untwinned* $YBa_2Cu_3O_{6.95}$ *Single Crystals*, preprint.

[11] M.J.P. Gingras, *Finite-Scale Remnants of a Kosterlitz-Thouless Transition and Temperature Dependence of the London Penetration Length of High-*T_c *Superconductors*, submitted to Phys. Rev. Lett. (1994).

[12] C.J. Gorter and H. Casimir, Physica **1**, 306 (1934).

[13] R.P. Huebener, *Magnetic Flux Structures in Superconductors*, edited by P. Fulde (Springer, Berlin, 1992).

[14] P.G. deGennes, *Superconductivty of Metals and Alloys*, (Addison-Wesley Publishing Company Inc., California, 1989).

[15] Saint-James, Thomas and Sarma, *Type-II Superconductivity*, (Pergamon Press Ltd., 1969).

[16] C. Kittel, *Introduction to Solid State Physics*, (John Wiley and Sons, 1976).

[17] D.R. Tilley and J. Tilley, *Superfluidity and Superconductivity*, (Adam Hilger Ltd, Bristol, 1990).

[18] J.W. Lynn, *High Temperature Superconductivity*, 268 (Springer-Verlag, New York, Inc., 1990).

[19] V.L. Ginzburg and L.D. Landau, Zh. Eksp. Teor. Fiz **20**, 1064 (1950).

[20] R.D. Parks, *Superconductivity Vol.2*, (Marcel Dekker, Inc., New York 1969).

[21] A.N. Lykov, Advances in Physics **42**, 263 (1993).

[22] A.D.C. Grassie, The Superconducting State (Sussex University Press, 1975).

[23] E. Dagotto, *Correlated Electrons in High Temperature Superconductors*, submitted to Review of Modern Physics.

[24] J. Bardeen, L.N. Cooper and J.R. Schrieffer, Phys. Rev. **108**, 1175 (1957).

[25] Frölich, Phys. Rev. **79**, 845 (1950).

[26] N.W. Ashcroft and N.D. Mermin, *Solid State Physics*, (Holt, Rinehart and Winston, 1976).

[27] J.R. Schrieffer, *Nobel Lecture, Physics Today*, 23 (1973).

[28] B.G. Levi, Physics Today, 17 (May 1993).

[29] B. Muhlschlegel, Z. Phys. **155**, 313 (1959).

[30] T. Hirata and Y. Asada, J. Supercond. **4**, 171 (1991).

[31] F. Reif and M.A. Woolf, Phys. Rev. Letters **9**, 315 (1962).

[32] J. Rammer, Physica C **177**, 421 (1991).

[33] S.A. Gordyunin *et al.*, JETP Lett. **47**, 40 (1988).

[34] E.H. Brandt, Phys. Rev. B **37**, 2349 (1988).

[35] A.A. Abrikosov, Soviet Phys. JETP **5**, 1174 (1957).

[36] H. Svensmark and L.M. Falicov, Phys. Rev. B **42**, 9957 (1990).

[37] W.R. Hudson, *The Mixed State of Superconductors*, (National Aeronautics and Space Administration, 1970).

[38] C.G. Kuper, *An Introduction to the Theory of Superconductivity* (Clarendon Press, Oxford, 1968).

[39] A.C. Rose-Innes and E.H. Rhoderick, *Introduction to Superconductivity* (Pergamon Press, Great Britain, 1988).

[40] W.H. Kleiner, L.M. Roth and S.H. Autler, Phys. Rev. **133**, A1226 (1964).

[41] D.J. Bishop, P.L. Gammel and D.A. Huse, *Resistance in High-Temperature Superconductors*, Scientific American, 48 (Feb 1993).

[42] P.L. Gammel, D.J. Bishop, G.J. Dolan, J.R. Kwo, C.A. Murray, L.F. Schneemeyer and J.V. Waszczak, Phys. Rev. Lett. **59**, 2592 (1987).

[43] D. Pines, *Nearly Antiferromagnetic Fermi Liquids are High Temperature Superconductors: Are the Superconducting Cuprates Nearly Antiferromagnetic Liquids?*, submitted to J. Chem. Phys. Solids (1993).

[44] J.R. Christman, *Fundamentals of Solid State Physics*, (John Wiley and Sons, Inc., New York, 1988).

[45] J.E.C. Williams, *Superconductivity and its Applications* (Pion Limited, London, 1970).

[46] V.Z. Kresin and S.A. Wolf, *Fundamentals of Superconductivity* (Plenum Press, New York, 1990).

[47] A. Virosztek and J. Ruvalds, Phys. Rev. B **42**, 4064 (1990).

[48] C.M. Varma, P.B. Littlewood and S. Schmitt-Rink, Phys. Rev. Lett. **63**, 1996 (1989).

[49] J.R. Schrieffer, X.G. Wen and S.C. Zhang, Phys. Rev. B **39**, 11663 (1989).

[50] V.L. Ginzburg, Physica C **209**, 1 (1993).

[51] N.E. Bickers, D.J. Scalapino and S.R. White, Phys. Rev. Lett. **62**, 961 (1989).

[52] T. Moriya, Y. Takahashi and K. Ueda, Physica C **185-189**, 114 (1991).

[53] P. Monthoux and D. Pines, Phys. Rev. Lett. **69**, 961 (1992).

[54] P. Monthoux and D. Pines, Phys. Rev. B **49**, 4261 (1994).

[55] N. Bulut, D.W. Hone, D.J. Scalapino and N.E. Bickers, Phys. Rev. B **41**, 1797 (1990).

[56] A.J. Millis, H. Monien and D. Pines, Phys. Rev. B **42**, 167 (1990).

[57] T. Moriya, Y. Takahashi and K. Ueda, J. Phys. Soc. Jpn. **59**, 2905 (1992).

[58] P. Mendels, J.H. Brewer, H. Alloul, E.J. Ansaldo, D.R. Noakes, Ch. Niedermeyer, G. Collin, J.F. Marucco, C.E. Stronach, G.D. Morris, T.L. Duty and S. Johnston, *μ^+SR Study of the Effect of Zn Substitution of Magnetism in $YBa_2Cu_3O_x$*, submitted to Phys. Rev. Lett. (1993).

[59] K.V.R. Rao and K.B. Garg, Physica C **178**, 352 (1991).

[60] R.N. Shelton, *High Temperature Superconductivity*, edited by J.W. Lynn, 168 (Springer-Verlag, New York, Inc., 1990).

[61] S.K. Yip and J.A. Sauls, Phys. Rev. Lett. **69**, 2264 (1992).

[62] Q. Si, Y. Zha, K. Levin and J.P. Lu, Phys. Rev. B **47**, 9055 (1993).

[63] K. Ueda, T. Moriya and Y. Takahashi, J. Phys. Chem. Solids **53**, 1515 (1992).

[64] R. Gagnon, C. Lupien and L. Taillefer, *T^2 Dependence of the Resistivity in the Cu-O Chains of $YBa_2Cu_3O_{6.9}$*, preprint.

[65] D.M. Ginsberg, W.C. Lee and S.E. Stupp, Phys. Rev. B **47**, 12167 (1993).

[66] W. Barford and J.M.F. Gunn, Physica C **156**, 515 (1988)

[67] V.G. Kogan, Phys. Rev. B **24**, 1572 (1981).

[68] B. Pümpin, H. Keller, W. Kündig, W. Odermatt, I.M. Savić, J.W. Schneider, H. Simmler, P. Zimmerman, E. Kaldis, S. Rusiecki, Y. Maeno and C. Rossel, Phys. Rev. B **42**, 8019 (1990).

[69] M. Yethiraj, H.A. Mook, G.D. Wignall, R. Cubitt, E.M. Forgan, S.L. Lee, D.M. Paul and T. Armstrong, Phys. Rev. Lett. **71**, 3019 (1993).

[70] W.A. Little, *Physics of High-Temperature Superconductors*, 113 (Springer-Verlag, Berlin Heidelberg, 1992).

[71] S.S. Jha, *Studies of High Temperature Superconductors*, vol. 1, (Nova Science Publishers Inc., New York, 1989).

[72] E.H. Brandt, J. Low Temp. Phys. **73**, 355 (1988)

[73] H. Keller, *Earlier and Recent Aspects of Superconductivity*, edited by J.G. Bednorz and K.A. Müller, 222 (Springer-Verlag, Berlin, 1990).

[74] A.D. Sidorenko, V.P. Smilga and V.I. Fesenko, Hyperfine Interactions **63**, 49 (1990).

[75] V. Fesenko, V. Gorbunov, A. Sidorenko and V. Smilga, Physica C **211**, 343 (1993).

[76] E.H. Brandt, Journal of Low Temp. Phys. **26**, 709 (1977)

[77] T.M. Risemann, Ph.D. thesis, University of British Columbia (1993)

[78] S.L. Thiemann, Z. Radović and V.G. Kogan, Phys. Rev. B **39**, 11406 (1989).

[79] A. Schenck, *Muon Spin Rotation Spectroscopy: Principles and Applications in Solid State Physics* (Adam Hilger Ltd., 1985).

[80] S.F.J. Cox, J. Phys. C **20**, (1987).

[81] E.H. Brandt and A. Seeger, Adv. in Phys. **35**, 189 (1986).

[82] P. Monthoux, A.V. Balatsky and D. Pines, Phys. Rev. B **46**, 14803 (1992).

[83] K. Ishida, Y. Kitaoka, N. Ogata, T. Kamino, K. Asayama, J.R. Cooper and N. Athanassopoulu, J. Phys. Soc. Jpn. **62**, 2803 (1993).

[84] D.A. Bonn *et al.*, *Oxygen Vacancies, Zinc Impurities and the Intrinsic Microwave Loss of* $YBa_2Cu_3O_{6.95}$, submitted to Phys. Rev. B (1993).

[85] R.X. Liang, P. Dosanjh, D.A. Bonn, D.J. Barr, J.F. Carolan and W.N. Hardy, Physica C **195**, 51 (1992).

[86] J.W. Schneider, R.F. Kiefl, K.H. Chow, S. Johnston, J.E. Sonier, T.L. Estle, B. Hitti, R.L. Lichti, S.H. Connell, J.P.F. Sellschop, C.G. Smallman, T.R. Anthony and W.F. Banholzer, Phys. Rev. Lett. **71**, 557 (1993).

[87] J.E. Sonier, R.F. Kiefl, J.H. Brewer, D.A. Bonn, J.F. Carolan, K.H. Chow, P. Dosanjh, W.N. Hardy, Ruixing Liang, W.A. MacFarlane, P. Mendels, G.D. Morris, T.M. Riseman and J.W. Schneider, Phys. Rev. Lett. **72**, 744 (1994).

[88] Recent μ^+SR measurements of the temperature dependence of λ_{ab} in $YBa_2(Cu_{0.997}Zn_{0.003})_3O_{6.95}$, in an applied field of 0.2T, show a distinct weakening of the linear term in agreement with microwave cavity measurements performed on the same sample., unpublished (1994).

Appendix A

Some Remarks About The Fitting Program

The computer time allocated to calculating $B(\vec{r})$ of Eq. (3.9), is significant enough that it is practical to avoid the large sum over reciprocal lattice vectors $\vec{K}$ for each iteration in the χ^2-minimization procedure. Consequently, a Taylor series expansion around an initial value of the magnetic penetration depth λ_o was employed in the actual fitting program:

$$\begin{aligned} B(\vec{r}) \equiv B(\vec{r}, \frac{1}{\lambda^2}) &\approx B(\vec{r}, \frac{1}{\lambda_o^2}) + \left(\frac{1}{\lambda^2} - \frac{1}{\lambda_o^2}\right) \frac{\partial B\left(\vec{r}, \frac{1}{\lambda_o^2}\right)}{\partial\left(\frac{1}{\lambda^2}\right)} \\ &+ \frac{1}{2}\left(\frac{1}{\lambda^2} - \frac{1}{\lambda_o^2}\right)^2 \frac{\partial^2 B\left(\vec{r}, \frac{1}{\lambda_o^2}\right)}{\partial\left(\frac{1}{\lambda^2}\right)^2} \end{aligned} \tag{A.1}$$

so that, $B(\vec{r}, \frac{1}{\lambda^2})$ is determined by expanding about the initial point $\left(\vec{r}, \frac{1}{\lambda_o^2}\right)$. In this way, $B(\vec{r})$ is calculated by summing over the reciprocal lattice vectors $\vec{K}$ [in Eq. (3.9)], only once for an initial set of parameters $\frac{1}{\lambda_o^2}$ and B_o, where B_o is the initial value of the average field. It is not necessary to expand about B_o. This is because changes in the average field merely shift the field distribution along the field (or frequency) axis. In the fitting process, field shifts in excess of a conservative value of ~ 0.00073T were not permitted before the program was stopped, the initial parameters changed, and the data refitted.

Table A.1 shows the accuracy of the Taylor series assuming an average magnetic field 0.5T and $\kappa = 68$. The error in using Eq. (A.1), expressed as a percentage of the exact calculation of $B(\vec{r})$ using Eq. (3.9), is shown for $B(\vec{r})$ calculated at the vortex

$1/\lambda_o^2$ (μm^{-2})	$1/\lambda^2$ (μm^{-2})	*% Error in $B(\vec{r})$ at the vortex core.*	*% Error in $B(\vec{r})$ at the saddle point.*
50	50	0.00	0.00
50	49	0.16	0.14
50	48	0.31	0.27
50	47	0.47	0.40
50	46	0.62	0.53
50	45	0.78	0.67
50	44	0.93	0.80
50	43	1.08	0.93
50	30	3.01	2.65
50	20	4.43	3.96
50	10	5.78	5.25
50	0	7.07	6.54

Table A.1: Accuracy of the Taylor series expansion used in the fitting program.

core and at a saddle point. The results show that even large changes in $\frac{1}{\lambda^2}$ give a good approximation for $B(\vec{r})$. In a typical fit, $B(\vec{r})$ is calculated in excess of $150,000$ times, so that using a Taylor series greatly diminishes the time required to fit.